A Thesis for the Degree of Ph.D. in Science

Thermodynamic Properties of a Strongly Interacting Ultracold Fermi Gas and Application to Neutron Star Equation of State

February 2018

Graduate School of Science and Technology
Keio University

Pieter van Wyk

Abstract

In this thesis, I theoretically investigate thermodynamic properties of an ultracold Fermi gas. Including pairing fluctuations within the framework of the theory developed by Nozières and Schmitt-Rink (NSR), I examine strong-coupling corrections to the internal energy, as well as the specific heat at constant volume C_V, over the entire BCS (Bardeen-Cooper-Schrieffer)-BEC (Bose-Einstein condensation) crossover region. Using the similarity between a superfluid Fermi gas in the unitary regime and the crust regime of a neutron star interior, I also show an application of the former atomic system as a quantum simulator for the study of the latter.

In the normal state of an ultracold Fermi gas, C_V is found to be sensitive to pairing fluctuations. From the detailed temperature dependence of C_V, I identify the region where pairing fluctuations dominate over the system, as well as the region where most atoms form bound molecules, in the phase diagram with respect to the strength of a pairing interaction and the temperature.

Although properties of the crust regime of a neutron star is expected to be similar to a superfluid Fermi gas in the unitary regime far below T_c, one cannot immediately use results obtained in the latter for the study of the former. This is because the magnitude of the effective range $r_{\rm eff}$ is very different between the two. That is, while $r_{\rm eff}$ is negligibly small in ultracold Fermi gases, one cannot ignore $r_{\rm eff} = 2.7$ fm in the neutron star case. In this thesis, I theoretically make up for this difference, to examine the neutron star equation of state (EOS). For this purpose, I first show that the NSR internal energy agrees well with the recent experiment on a superfluid ^{6}Li Fermi gas, far below T_c. I then extend this theory, to include the non-vanishing effective range $r_{\rm eff} = 2.7$ fm. The calculated EOS by this extended NSR scheme is found to well reproduce previous results in the low-density regime, obtained in nuclear physics. This agreement indicates the validity of a superfluid Fermi gas as a quantum simulator for the study of the low-density crust regime of a neutron star interior.

Contents

1 Introduction **1**

1.1 BCS-BEC Crossover In An Ultracold Fermi Gas With A Feshbach Resonance 1

1.2 Observed Quantities In The BCS-BEC Crossover Region 4

1.3 Specific Heat As A Probe For Pairing Fluctuations 8

1.4 Internal Energy Of A Superfluid Fermi Atom Gas And Application To Neutron Star Equation Of State 11

1.4.1 Introduction To Neutron Stars 12

1.4.2 Cold Atoms And Neutron Star Equation Of State 13

1.5 Purpose And Organisation Of This Thesis 17

2 Strong Coupling Formalism For Attractively Interacting Fermi Systems **19**

2.1 Strong Coupling Theory In The Normal State 19

2.1.1 Model Hamiltonian 19

2.1.2 NSR Theory In The Normal State 20

2.1.3 Internal Energy And Specific Heat Above T_c 26

2.2 NSR Theory In The Superfluid State 27

2.2.1 Nambu Representation 27

2.2.2 Strong Coupling Corrections To The Thermodynamic Potential In The Superfluid Phase 28

2.2.3 Internal Energy And Specific Heat Below T_c 31

2.3 Superfluid NSR Theory With A Non-Vanishing Effective Range r_{eff} (Neutron Star Case) 31

2.3.1 Effective Range Theory 32

2.3.2 Superfluid NSR Theory In The Presence Of Non-Vanishing Effective Range 35

2.3.3 Internal Energy Far Below T_c 37

3 Specific Heat In The BCS-BEC Crossover Region Of An Ultracold Fermi Gas **39**

3.1 Specific Heat At T_c 39

3.2 Specific Heat Above T_c 43

3.2.1 The Strong Coupling Side $(k_F a_s)^{-1} \gtrsim 0$ 44

3.2.2 The Weak Coupling Side $(k_F a_s)^{-1} \lesssim 0$ 48

3.3 Specific Heat Below T_c 48

3.4 Phase Diagram Of An Ultracold Fermi Gas 49

3.5 Comparison With Experiment 52

4 Application To Neutron Star Equation Of State **53**
4.1 EOS Of A Superfluid Fermi Gas In The BCS-Unitary Regime . . 53
4.2 Neutron Star Equation Of State In The Low Density Regime . . . 54
4.3 Effects Of A Finite Effective Range On Thermodynamic Properties 58
4.4 Correction From Density Fluctuations To The Equation Of State . 59

5 Summary **63**

A Proton Fraction In Non-Interacting Nuclear Matter **67**

B Derivation Of Eq.(2.57) And Eq.(2.60) **69**

C Derivation Of Eq.(2.71) **71**

Chapter 1

Introduction

In this chapter we introduce the ultracold Fermi gas in the BCS-BEC crossover region, as a useful system for studying strong correlation effects. After giving an outline of ultra cold Fermi gas physics and the BCS-BEC crossover in Sec.1.1, we discuss recent measurements on thermodynamic quantities in this system in Sec.1.2. In Sec.1.3 the specific heat at constant volume C_V is introduced as a useful quantity for studying strong-coupling effects in the BCS-BEC crossover region of an ultracold Fermi gas. In Sec.1.4. we give a brief introduction to neutron star physics, and discuss how the ultracold Fermi gas could be used as a *quantum simulator* to study this mysterious astronomical object. Finally, in Sec.1.5. we give the purpose and organisation of this thesis.

1.1 BCS-BEC Crossover In An Ultracold Fermi Gas With A Feshbach Resonance

The study of strongly correlated many-body quantum systems is one of the most exciting challenges in modern condensed matter physics. Together with quantum statistics (Fermi or Bose), as well as the system dimension, various novel phenomena have been discussed in these systems, such as superconductivity, Bose-Einstein condensation (BEC) [1], fractional quantum Hall state, and quantum spin liquid [2]. Cold atom physics is turning out to be a crucial key element in unlocking mysteries originating from strong correlations [3].

Due to their underlying simplicity, as well as high controllability, gasses of trapped Fermi and Bose atoms have attracted much experimental and theoretical attention [1, 3–42]. One of the most striking features of these systems is that one can experimentally tune the interaction between atoms by using a Feshbach resonance [6]. Using this technique, the so-called BCS (Bardeen-Cooper-Schrieffer)-BEC crossover phenomenon has been realised in ^{40}K [9] and ^{6}Li [10–12] Fermi gas. Here the character of a Fermi superfluid continuously changes from the weak-coupling BCS-type to BEC of tightly bound molecules that have already been formed above the superfluid phase transition temperature T_c with increasing the strength of a pairing interaction (see Fig.1.1). Before this achievement in cold atom physics, this many-body phenomenon had been merely an academic problem, although it has also been discussed as a possible mechanism of the pseudogap observed in the underdoped region of high-T_c cuprates [43–45].

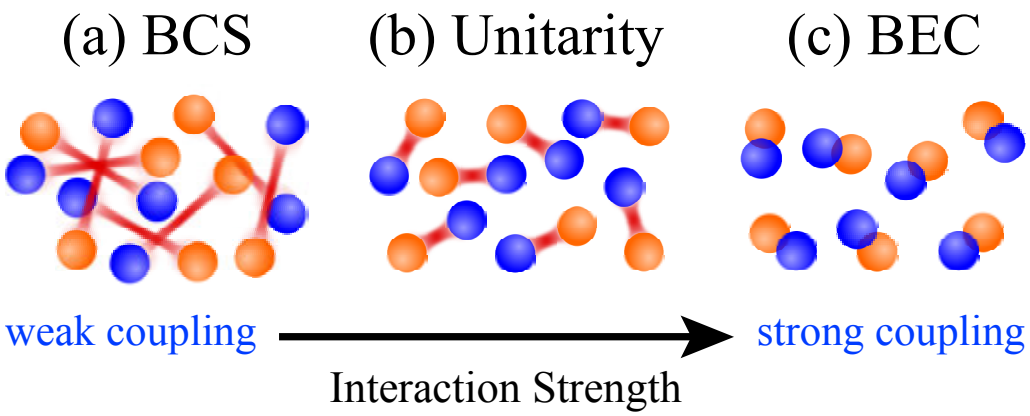

Figure 1.1: Schematic illustration of the BCS-BEC crossover in an ultracold Fermi gas. (a) weak-coupling BCS regime, where Cooper pairs are largely overlapping. (b) Unitarity limit, where the pairing size is comparable to the interatomic distance. (c) Strong-coupling BEC regime, where the molecular size is much smaller than the interatomic distance. The blue and orange spheres describes Fermi atoms in different hyperfine states.

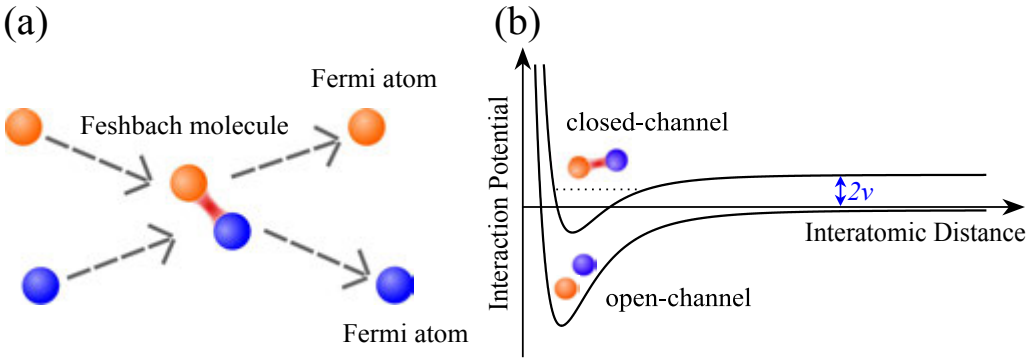

Figure 1.2: (a) Schematic illustration of a Feshbach resonance. The orange and blue spheres represent Fermi atoms in different hyperfine states. (b) Interaction potential as a function of the relative distance between two atoms in the closed and open-channel, respectively. 2ν is the threshold energy of a Feshbach resonance.

Since the realisation of superfluid ^{40}K and ^{6}Li Fermi gases, the BCS-BEC crossover has become one of the central topics, as a realistic problem, not only in cold atom physics, but also in the field of strong-coupling Fermi superfluids [46–54]. Very recently, the BCS-BEC crossover has been discussed in the unconventional superconductor FeSe [55, 56].

To simply explain how to tune an atomic interaction by using a Feshbach resonance, we schematically draw this phenomenon in Fig.1.2 (a). In this resonance phenomenon, atoms (open channel) form a quasi molecular boson (closed channel) which is formed in the dip of a Lenard-Jones type interatomic potential shown in Fig.1.2 (b), and it again dissociates into two atoms (open channel). In this case, since the atomic hyperfine states in the open channel are different from those in the closed channel (which is caused by the hyperfine interaction), their Zeeman energies are different from each other under the external magnetic field. As a re-

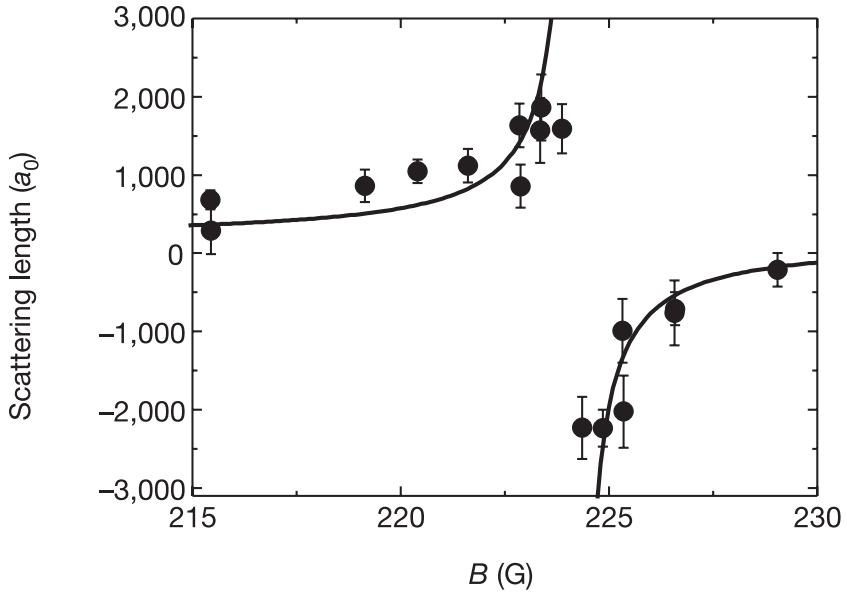

Figure 1.3: Magnetic field dependence of the s-wave scattering length $a_s(B)$ near a Feshbach resonance at B_0=224.21 ± 0.05 G in a ^{40}K Fermi atom gas. This interaction works between the hyperfine states $|9/2, -9/2\rangle$ and $|9/2, -7/2\rangle$. [Reprinted figure with the permission from Macmillan Publishers Ltd: Nature, C. A. Regal, C. Ticknor, J. L. Bohn and D. S. Jin, "Creation of ultracold molecules from a Fermi gas of atoms," **424**, 47-50 (2003), copyright (2003).]

sult, the energy of the Feshbach molecular state (closed channel) 2ν in Fig.1.2 (b) depends on the difference of the Zeeman energies between the two channels. This means that the energy 2ν can be tuned by adjusting an external magnetic field. This magnetically tunable resonance energy 2ν is also referred to as the threshold energy of a Feshbach resonance in the interaction.

When we evaluate this Feshbach resonance process within the second order perturbation theory, the effective interaction $U_{\rm eff}$ between two Fermi atoms in the open channel is obtained as

$$U_{\rm eff} = g\frac{1}{0-2\nu}g = -\frac{g^2}{2\nu}, \tag{1.1}$$

where g is a Feshbach coupling, and we have assumed that the total energy of the initial atomic states equals zero. When an external magnetic field B is close to a Feshbach resonance field B_0, the threshold energy 2ν may be written as

$$2\nu = \alpha(B - B_0), \tag{1.2}$$

where α is a constant.

Atoms also feel a non-resonant weak interaction potential U_0. Measuring the interaction strength in terms of the scattering length $a_s(B)$ we obtain

$$a_s(B) = a_s^{bg}\left[1 - \frac{\lambda}{B - B_0}\right], \tag{1.3}$$

where a_s^{bg} is a background s-wave scattering length associated with U_0, and λ is the width of a Feshbach resonance.

Figure 1.3 shows an example of a Feshbach resonance-induced tunable interaction in a ^{40}K Fermi gas. As expected from Eq.(1.3), the tunable s-wave scattering length changes its sign at the resonance field $B_0 \simeq 224$ G.

So far, the superfluid phase transition, as well as the BCS-BEC crossover, have been realised in ^{40}K and ^{6}Li Fermi gases [3, 9, 11, 12]. In the former case, the strength of a pairing interaction working between $|F = 9/2, F_z = -9/2\rangle$ and $|F = 9/2, F_z = -7/2\rangle$ is tuned by the Feshbach technique (see Fig.1.3). Here, $\boldsymbol{F} = \boldsymbol{S} + \boldsymbol{I}$, when $\boldsymbol{S}$ is the electron spin and $\boldsymbol{I}$ is the nuclear spin. In the case of a ^{6}Li Fermi gas this technique is used to tune the interaction strength between $|F = 1/2, F_z = 1/2\rangle$ and $|F = 1/2, F_z = -1/2\rangle$. Since the detailed atomic states are actually irrelevant in considering the BCS-BEC crossover, they are usually described by a pseudo-spin $\sigma = \uparrow, \downarrow$.

1.2 Observed Quantities In The BCS-BEC Crossover Region

While the tunable pairing interaction associated with a Feshbach resonance is an advantage of cold Fermi gas physics, it was difficult to observe various physical quantities in the BCS-BEC crossover region in the early stage of research for superfluid ^{40}K and ^{6}Li Fermi gases [1, 3]. However, extensive experimental efforts have enabled us to measure several quantities that are useful in examining strong-coupling properties of this system in the crossover region [32, 33].

Figure 1.4 shows the results of the photoemission-type experiment on a ^{40}K Fermi gas developed by JILA group [25, 26]. This experiment is similar to the photoemission spectroscopy in condensed matter physics, and spectral intensity involves information about Fermi single-particle excitations. Indeed, in the weak-coupling BCS regime shown in Fig.1.4 (a), the spectral peak line is just along the free particle dispersion $\omega = k^2/2m$. Thus, using this experimental technique, we can observe how single-particle properties of an ultracold Fermi gas varies as one increases the strength of a pairing interaction in the BCS-BEC crossover region.

At the unitarity (which may be regarded as the centre of the BCS-BEC crossover region), we see in Fig.1.4 (b) that the spectral intensity becomes broad, and the peak positions (white dots) deviate from the free particle dispersion (black solid line), to exhibit the so-called back-bending behaviour (the hump structure seen around $k = 10\,\mu\mathrm{m}^{-1}$ in Fig.1.4 (b)).

Regarding this, the broadening of the spectral peak indicates the short lifetime of a quasiparticle excitation due to strong pairing interaction in the unitarity limit. For the back bending behaviour, the peak curve is similar to the lower branch of the Bogoliubov single-particle excitations in the BCS-theory

$$E_b = -\sqrt{\left(\frac{\boldsymbol{k}^2}{2m} - \mu\right)^2 + \Delta^2}, \tag{1.4}$$

(μ is the Fermi chemical potential, and Δ is the superfluid order parameter), although the system is in the normal state in the case of Fig.1.4 (b). When we recall

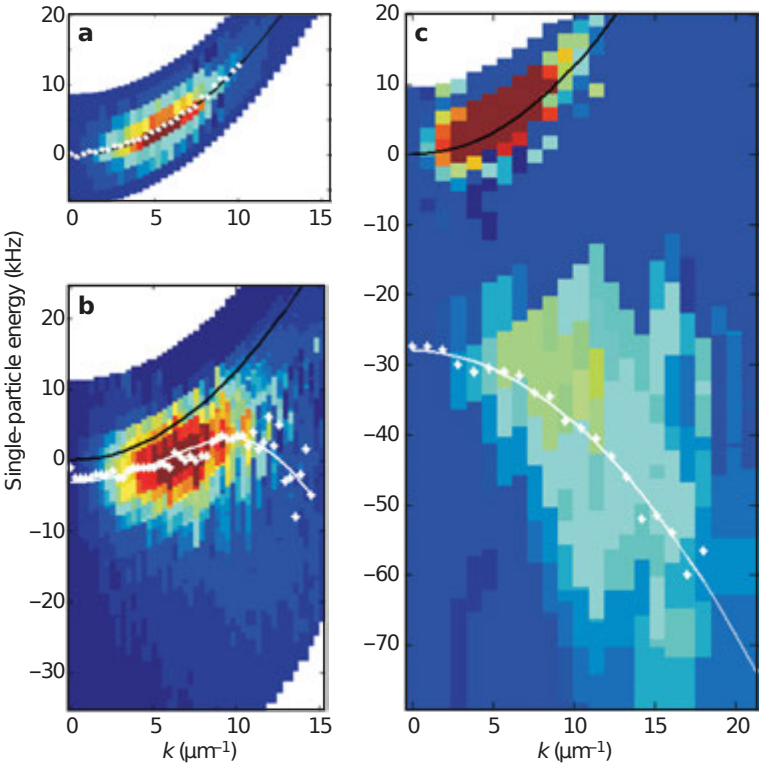

Figure 1.4: Observed photoemission spectra in the BCS-BEC crossover regime of a ^{40}K Fermi gas [25]. (a) Weak-coupling BCS regime. (b) Unitarity limit. (c) Strong-coupling BEC regime. The solid curve represents the free particle dispersion $\omega = k^2/2m$. The white dots are peak positions of the spectral intensity. The white curves in (b) and (c) represent fittings with respect to the Bogoliubov-type dispersion in the BCS theory. In panel (b), the so-called back bending structure of the spectral weight peak is interpreted as indirect evidence for a pseudogap phenomenon, associated with strong pairing fluctuations at unitarity [22]. [Reprinted figure with the permission from Macmillan Publishers Ltd: Nature, J. T. Stewart, J. P. Gaebler, D. S. Jin, "Using photoemission spectroscopy to probe a strongly interacting Fermi gas," **454**, 744 (2008), copyright (2008).]

that Δ in the BCS state is directly related to single-particle excitation gap $E_{\rm gap}$, as

$$E_{\rm gap} = 2\Delta, \tag{1.5}$$

the back bending behaviour seen in Fig.1.4 (b) implies the existence of a quantity which plays a similar role to Δ for single-particle excitations. According to the preformed pair scenario [3, 4, 22, 24, 44, 45], this quantity is sometimes referred to as the pseudogap parameter ($\Delta_{\rm pg}$), which physically describes the binding energy of a preformed Cooper pair which is formed in the normal state, above $T_{\rm c}$, due to strong pairing interactions. Actually, preformed Cooper pairs are considered to not be stable, but fluctuation in the unitarity regime, so that the BCS-state-like clear excitation gap is not expected. Instead, a partially filled gap structure (which is also referred to as the pseudogap) is expected in the single-particle density of states. Although the direct observation of the density of states is still difficult in the current stage of cold Fermi gas physics, strong-coupling theories that can well explain the observed photoemission spectrum in Fig.1.4 (b) predict the pseudogapped density of states in the BCS-BEC crossover region near $T_{\rm c}$ [22].

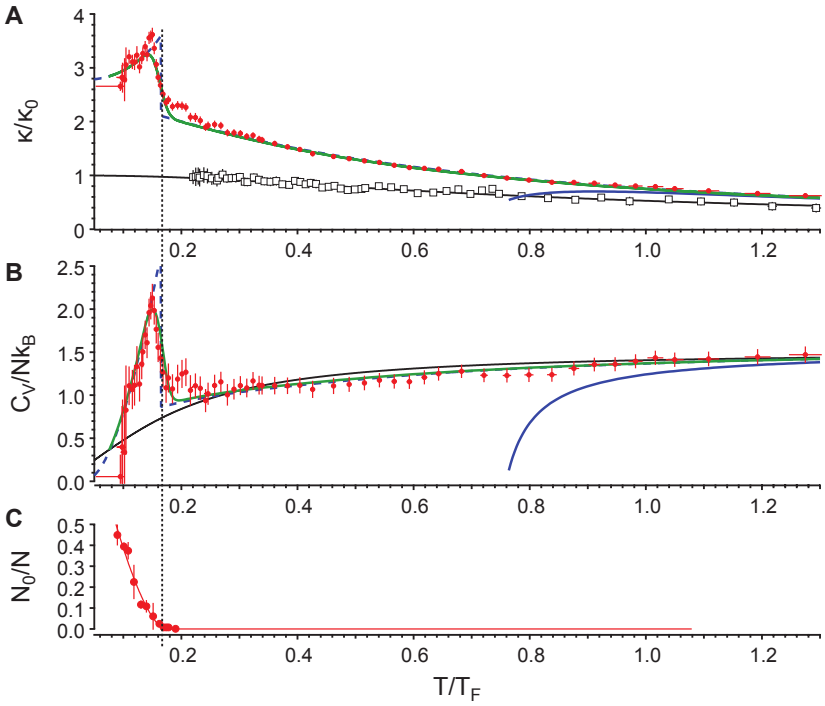

Figure 1.5: Measured temperature dependence of thermodynamic quantities in a unitary ^{6}Li Fermi atom gas (red circles). A Compressibility κ normalised by the compressibility $\kappa_0 = 3V/2\varepsilon_F N$ of a free Fermi gas at $T = 0$ (where ε_F is the Fermi energy and N the total number of atoms). B Specific heat at constant volume C_V. C Condensate Fraction N_0. The black and blue solid curves shows theoretical results for a free Fermi gas, and third-order virial expansion for a unitary Fermi gas, respectively. The black open squares show experimental measurements for a noninteracting Fermi gas. The green solid (blue curved) line shows model calculations including (excluding) finite imaging resolution effects. The vertical dashed line shows the position of the measured superfluid phase transition temperature $T_c = 0.167T_F$, where T_F is the Fermi temperature. [From M. J. H. Ku, A. T. Sommer, L. W. Cheuk, and M. W. Zwierlein, "Revealing the Superfluid Lambda Transition in the Universal Thermodynamics of a Unitary Fermi Gas," Science. **335**. 563-567 (2012). Reprinted with permission from AAAS.http://dx.doi.org/10.1126/science.1214987.]

In the strong coupling BEC regime, the photoemission spectre exhibits a double peak structure, as shown in Fig.1.4 (c). In this region, most Fermi atoms form tightly bound stable molecules, so that the energy difference between the two branches is considered as the dissociation energy of the molecules.

Although the preformed pair scenario, and associated pseudogap scenario, is consistent with the photoemission-type experiment shown in Fig.1.4, experiments on the local pressure in a ^{6}Li unitary Fermi gas is well explained by the ordinary Fermi liquid theory [27]. Since the pseudogap does not appear in a ordinary Fermi liquid, the existence of this many-body phenomenon is still in debate in cold Fermi gas physics.

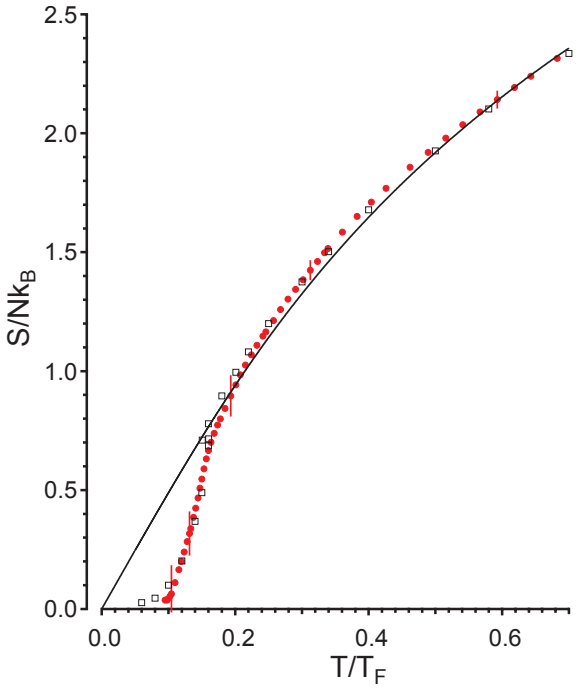

Figure 1.6: Measured entropy S per particle (red circles). The black solid curves and open squares show the results for a free Fermi gas, and the self-consistent T-matrix approximation (SCTMA) [29], respectively. [From M. J. H. Ku, A. T. Sommer, L. W. Cheuk, and M. W. Zwierlein, "Revealing the Superfluid Lambda Transition in the Universal Thermodynamics of a Unitary Fermi Gas," Science. **335**. 563-567 (2012). Reprinted with permission from AAAS.http://dx.doi.org/10.1126/science.1214987.]

Besides the photoemission spectre, various thermodynamic quantities have become experimentally accessible in the BCS-BEC crossover regime of an ultracold Fermi gas. Figures 1.5, 1.6 and 1.7 show the temperature dependence of thermodynamic quantities in a unitary ^{6}Li Fermi gas [32], and the ground-state quantities in a ^{6}Li superfluid Fermi gas in the BCS-unitary regime [33].

If the normal phase of an ultracold Fermi gas was really well described by the Landau theory for a normal Fermi liquid [57], the compressibility κ and specific heat C_V shown in Fig.1.5 (a) and (b) should not significantly deviate from the case of a normal Fermi gas, except for mass renormalisation (effective mass) and quasi-particle life time away from the Fermi level. However, it is clear that this is not the case, especially as one approaches the phase transition temperature T_c, from above. Indeed, C_V in the case of a normal Fermi liquid is linear in temperature in the low-temperature region where $T/T_F \ll 1$ (where T_F is the Fermi temperature). The measured C_V is, however, sharply decreasing with increasing the temperature near T_c, akin to the so-called lambda transition known in liquid ^{4}He. This similarity has lead the authors of [32] to refer to the superfluid transition here as a "lambda transition", although the system is a ^{6}Li Fermi gas. Since discussions concerning the pseudogap phenomenon, as well as preformed Cooper pairs in an ultracold Fermi gas has mostly been confined to the single-particle spectral weight, an alternate approach from thermodynamics to this phenomena is expected to be useful. In this thesis, we pick up the specific heat at constant vol-

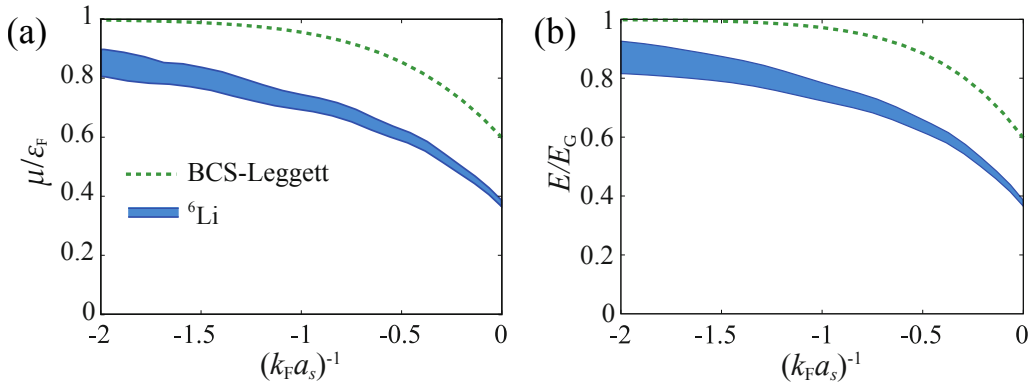

Figure 1.7: Measured ground state (a) chemical potential and (b) internal energy of a superfluid ^{6}Li Fermi gas in the BCS-unitarity regime [33]. $(k_Fa_s)^{-1}$ is the interaction strength, where $(k_Fa_s)^{-1} \lesssim -1$ is the weak-coupling BCS regime, and $(k_Fa_s)^{-1} = 0$ is the unitarity limit. The blue shaded area is the experimental measurements. The dotted line shows results in the BCS-Leggett mean-field theory.

ume C_V for the study of strong-coupling phenomena in the BCS-BEC crossover region.

In Fig.1.7, we find that although thermal fluctuations no longer exist at $T = 0$, the mean-field based BCS-Leggett theory cannot explain the observed internal energy E, nor the Fermi chemical potential μ of a superfluid ^{6}Li Fermi gas near $T = 0$, at a quantitative level. This indicates that, even far below T_c, we need to take into account strong-coupling effects beyond the mean-field theory in the region shown in Fig.1.7. In this thesis, we also demonstrate that the discrepancy between the mean-field result and experimental data in Fig.1.7 can be solved when we include effects of superfluid fluctuations in a consistent manner. As will be explained later, the region shown in Fig.1.7 is expected to be similar to the $^1S_0$ neutron superfluid, expected to exist in the crust regime of a neutron star. Thus, understanding this region would be important when one attempts to use a superfluid Fermi gas as a quantum simulator for the study of this compact star.

1.3 Specific Heat As A Probe For Pairing Fluctuations

In this thesis, we pick up the specific heat at constant volume C_V (which has recently become experimentally accessible, as shown in Fig.1.5) to clarify strong coupling properties of an ultracold Fermi gas in the BCS-BEC crossover region. In this section I explain the reason why this thermodynamic quantity is useful for our purpose.

According to the weak-coupling BCS theory, the specific heat exhibits a discontinuity at T_c, below which it decreases exponentially, as shown in figure 1.8 (a). This behaviour reflects the opening of the BCS excitation gap. Above T_c, C_V shows a linear-temperature dependence, when $T_c \leq T \ll T_F$, due to a nearly constant density of states near the Fermi level. Indeed, these characteristic be-

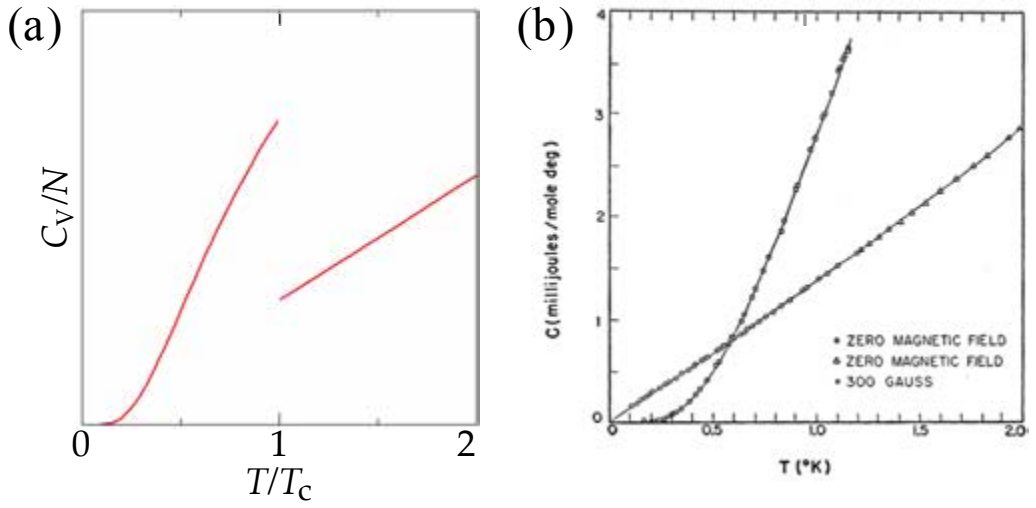

Figure 1.8: (a) Calculated Specific heat C_V in the mean-field BCS theory. C_V above T_c is proportional to T. (b) Observed C_V in Al ($T_c = 1.163°K$). The open squares and triangles are the measurements with no external magnetic field. The open circles are measurements under a magnetic field of 300 G, which is strong enough to destroy superconductivity in Al, so that the system is in the normal state. [Reprint figure with permission from N. E. Phillips, "Heat Capacity of Aluminum between 0.1°K and 4.0°K," Phys. Rev. **114**, 676 (1959). Copyright (1959) by the American Physical Society. https://doi.org/10.1103/PhysRev.114.676.]

haviours have been observed in the conventional superconductor Al, as shown in Fig.1.8 (b).

On the other hand, as shown in Fig.1.9, the specific heat of an ideal Bose gas exhibits a very different temperature dependence. That is, it monotonically decreases with increasing the temperature above the BEC phase transition temperature $T_{\rm BEC}$. There is also no jump in the specific heat at $T_{\rm BEC}$, being in contrast to the fermion case shown in Fig.1.8 (a). Since the formation of preformed pairs in the BCS-BEC crossover regime may be viewed as an enhancement of the bosonic character of a Fermi gas, C_V is expected to provide useful information about paring fluctuations above T_c.

This prospect can be further motivated by the thermodynamic relation [60]

$$C_V = T\left(\frac{\partial S}{\partial T}\right)_{N,V}, \tag{1.6}$$

connecting C_V with the entropy S. Noting that the entropy $S = k_B \ln \mathcal{W}$ (where k_B is Boltzmann's constant) is directly related to the total number $\mathcal{W}$ of microstates of the system, one may expect that, metastable bound states (fluctuating preformed Cooper pairs) associated with pairing fluctuations which are enhanced in the normal state near T_c, would decrease $\mathcal{W}$, as well as S. This would lead to enhancement of C_V with decreasing the temperature towards T_c. Indeed, as seen in Fig.1.6 the entropy of a unitary ^{6}Li Fermi gas becomes slightly suppressed in the normal state near $T_c = 0.167T_F$, compared to the non-interacting case.

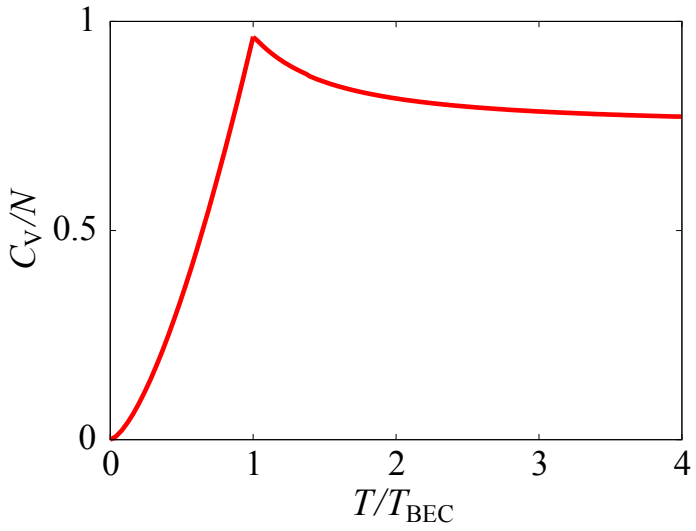

Figure 1.9: Specific heat C_V in an ideal Bose gas. T_{BEC} is the BEC transition temperature. Note that the temperature dependence of C_V above T_{BEC} is qualitatively different from a free Fermi gas (where $C_V \propto T$).

We note that the specific heat has already been used for the study of strong correlations in high-T_c cuprates [59]. In the underdoped regime shown in Fig.1.10 (a) and (b) the specific heat coefficient γ_{SC} smoothly varies near T_c, indicating the absence of the specific heat jump at T_c. In this regime, the pseudogap has been observed, although the origin of this is still unclear because of the complexity of this strongly correlated electron system [43–45, 59]. In the overdoped regime (Fig.1.10 (d)) γ_{SC} has a sharp peak at T_c, indicating the discontinuity of C_V at this temperature, as in the weak-coupling BCS theory. In this regime, the pseudogap is absent. These results also make us expect that the specific heat is effective for the study of the strong-coupling effects in the BCS-BEC crossover region of an ultracold Fermi gas.

We also note that, as another thermodynamic quantity, usefulness of the spin susceptibility χ_s for the study of BCS-BEC physics in an ultracold Fermi gas has been theoretically explored [24]. This approach is based on the idea that the preformed Cooper pair is a (pseudo)spin singlet state, so that χ_s is expected to be suppressed in the region where pairing fluctuations are enhanced. Using this so-called spingap phenomenon, ref [24] determines the region where pairing fluctuations dominate over system properties, which is close to the pseudogap regime (where a pseudogap appears in the density of states [22]), as expected.

However, although spin susceptibility is useful for the study of strong-coupling effects from the viewpoint of spin degrees of freedom, it is difficult to obtain useful information from this quantity in the strong-coupling BEC regime. This is simply because most Fermi atoms form spin-singlet pairs, so that in this region χ_s is highly suppressed. In this regard, the specific heat is not suppressed, even in the BEC regime (except near $T = 0$). Thus, using this, we can safely examine strong-coupling effects over the entire BCS-BEC crossover region. This is a reason why we pick up this thermodynamic quantity for our purpose.

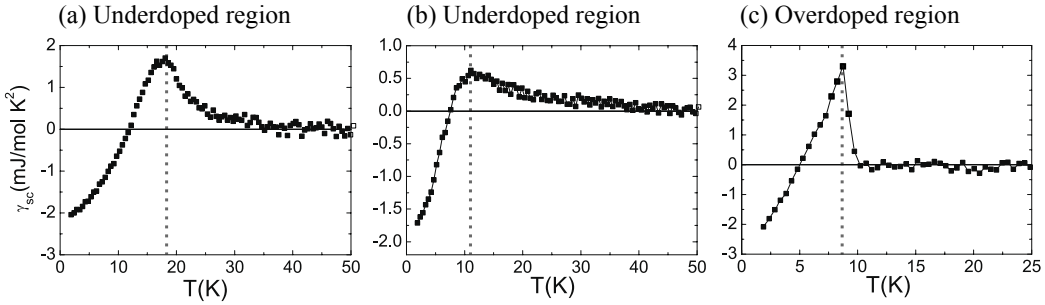

Figure 1.10: Observed specific heat coefficient $\gamma_{\rm SC} = [C_V - C_V\,({\rm N})]\,/T$, where $C_V\,({\rm N})$ is the specific heat measured under an external magnetic field which is strong enough to destroy superconductivity. (a) and (b) underdoped $Bi_2Sr_{2-x}La_xCuO_{6+\delta}$ ((a) $x = 0.7$, and (b) $x = 0.8$). (c) Overdoped $Bi_{1.74}Sr_{1.88}Pb_{0.38}CuO_{6+\delta}$. The vertical dashed line is at $T_{\rm c}$. [Reprint figure with permission from H. H. Wen, G. Mu, H. Luo, H. Yang, L. Shan, C. Ren, P. Cheng, J. Yan, L. Fang, "Specific-Heat Measurement of a Residual Superconducting State in the Normal State of Underdoped $Bi_2Sr_{2-x}La_xCuO_{6+\delta}$ Cuprate Superconductors," Phys. Rev. Lett. **103**, 067002 (2009). Copyright (2009) by the American Physical Society. https://doi.org/10.1103/PhysRevLett.103.067002.]

1.4 Internal Energy Of A Superfluid Fermi Atom Gas And Application To Neutron Star Equation Of State

Because of the high tunability of various physical parameters, a cold atomic gas is expected to be a useful quantum simulator for the study of unsolved many-body quantum systems, such as high-$T_{\rm c}$ cuprates. At present, however, this expectation has not been realised yet. This is because it is still difficult to completely replicate any target system by an ultracold atomic gas, even when one maximally makes use of the high controllability of the gas system [31, 44, 45].

To realise a quantum simulator made of a cold atomic gas, besides the above mentioned tunability, the recent theoretical development, especially in cold Fermi gas physics, may be helpful. Although quantitative theoretical analysis on strongly interacting fermions is usually difficult, the recent development of strong-coupling theory has enabled us to (semi) quantitatively compare theoretical predictions with experimental data in the BCS-BEC crossover regime of an ultracold Fermi gas, to some extent [22–24]. Then, even if the replication of the target system by an ultracold Fermi gas is incomplete, one may still quantum-simulate it by making up for the difference between the two by this strong-coupling theory. Such a hybrid approach would make the realisation of a cold-Fermi-gas quantum simulator more promising than the current approach aiming to the perfect replication of an unsolved quantum system.

In this thesis, to explore the possibility of this new approach, we pick up the neutron star. In this section, we give a brief overview of this highly dense astronomical object, to explain how to "quantum-simulate" it using an ultracold Fermi gas.

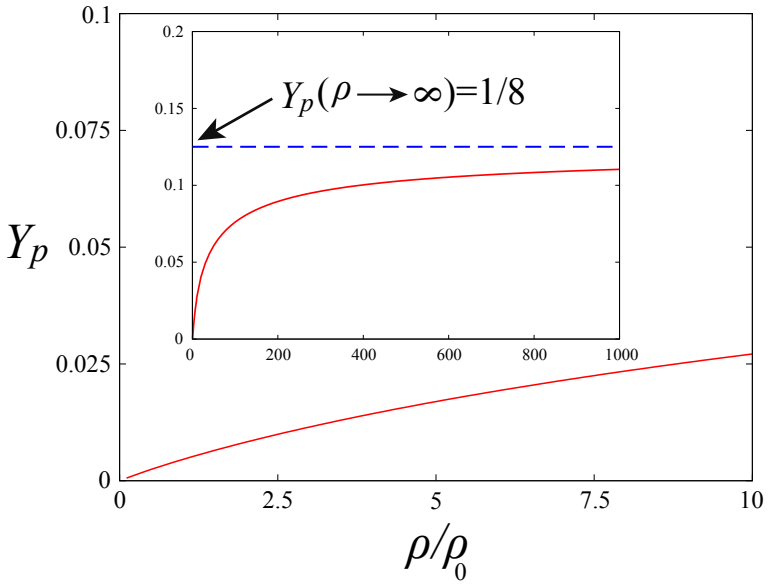

Figure 1.11: Density ρ dependence of the proton fraction $Y_p = n_p/n_n$ in non-interacting nuclear matter. $\rho_0 = m_n n_0$ is the neutron mass density at the nuclear saturation density $n_0 = 0.16$ fm^{-3}. The inset shows Y_p in the high density regime, where the dashed line shows the limiting value $Y_p(\rho \to \infty) = 1/8$ (see appendix A).

1.4.1 Introduction To Neutron Stars

At the end of the lifecycle of a massive star (with mass $M \gtrsim 8M_\odot$, where $M_\odot$ is the solar mass), when the mass of its iron core can no longer be sustained by the pressure of its electrons, gravitational collapse causes the star to explode in supernova. In the collapsing core of this explosion, a neutron star is considered to be born, as one of the most extreme objects in our universe. While a neutron star mass is comparable to $M_\odot$, the star radius is at most 10~15 km. Thus, neutron stars provide us with a unique opportunity for the study of extreme forms of matter, such as exotic nuclear superfluids and superconductors, beyond the reach of current terrestrial experiments.

Although neutron stars actually do not consist of pure neutron matter, it is at least true that they are very rich in neutrons. To realise this situation the beta decay plays a crucial role : Neutrons in the vacuum are unstable, and undergo beta-decay,

$$n \to p + e + \bar{\nu}_e, \tag{1.7}$$

where n, p, e and $\bar{\nu}_e$ denote a neutron, proton, electron and electron-antineutrino respectively. In addition to this process atomic nuclei are pressed together in the neutron star interior, so that, after the so-called neutron drip occurs, the large Coulomb repulsion between protons leads to the reverse beta decay,

$$p + e \to n + \nu_e. \tag{1.8}$$

When Eq.(1.1) and Eq.(1.2) balance out, an equilibrium state is reached with

$$\mu_n = \mu_p + \mu_e, \tag{1.9}$$

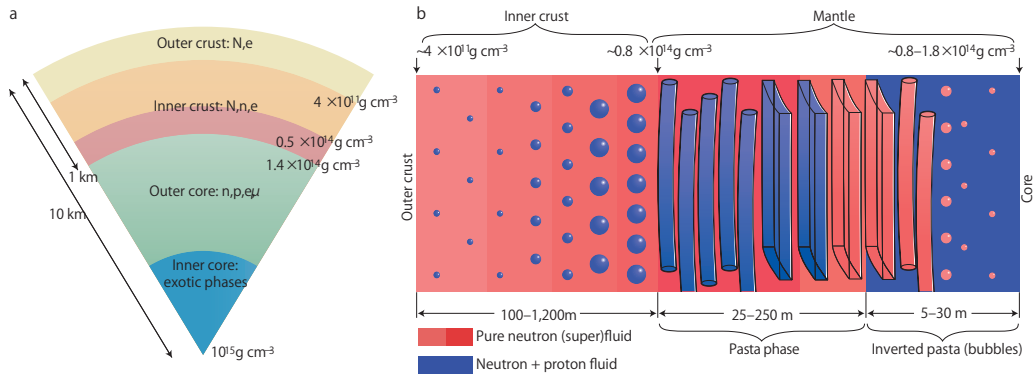

Figure 1.12: Schematic illustration of neutron star interior. (a) Overall structure. N, n, p, e, and μ are nuclei, fluid neutrons and protons, electrons and muons, respectively. (b) Detailed structure around the boundary between the crust and core regime. In the low density regime, a lattice of neutron-rich nuclei is immersed in a fluid of neutrons and relativistic electrons. At higher densities, nuclei are predicted to deform and connect along certain directions to form extended tubes, sheets and bubbles of nuclear matter, which is also referred to as nuclear pasta. [Reprinted figure with the permission from Macmillan Publishers Ltd: Nature, W. D. Newton, "Neutron stars: A taste of pasta?," Nature Physics, **9**, 396-397, (2013), copyright (2013).]

where μ_n, μ_p and μ_e are the Fermi chemical potential of a neutron, proton, and electron, respectively. Along with this beta-equilibrium condition, charge neutrality (requiring the equal number of protons and electrons) leads to a large increase in neutron density [62–64]. We can simply see this more clearly, by considering the non-interacting case, where

$$\mu_i = \sqrt{m_i^2 c^4 + p_{\mathrm{F}i}^2 c^2}. \tag{1.10}$$

Here, c is the speed of light in vacuum, m_i and $p_{\mathrm{F}i}$ denotes the mass and Fermi momentum for $i = n, p, e$. In this case, defining the proton fraction $Y_p = n_p/n_n$ (where n_p and n_n is the number density of protons and neutrons, respectively) and solving Eq.(1.9), we obtain Fig.1.11 (For the derivation, see appendix A). This figure shows that, beta-equilibrium leads to, $Y_p \ll 1$, that is, the system is dominated by neutrons. (Note that $\rho/\rho_0 \lesssim 10$ in the neutron star case.)

1.4.2 Cold Atoms And Neutron Star Equation Of State

The previous section gave a very simple reason why the interior of a "neutron" star is expected to be dominated by neutrons. Of course, protons and electrons still exist in the crust regime. As shown in Fig.1.12, when one passes through the neutron drip density, the crust regime is expected to be made up out of a lattice of nuclei surrounded by fluid neutrons, as well as relativistic electrons [65]. This is somehow similar to a metal, being composed of an ionic lattice and conduction electrons [57]. As in the metallic case, when we theoretically deal with the crust regime of a neutron star, in the first step, it would be allowed to approximately

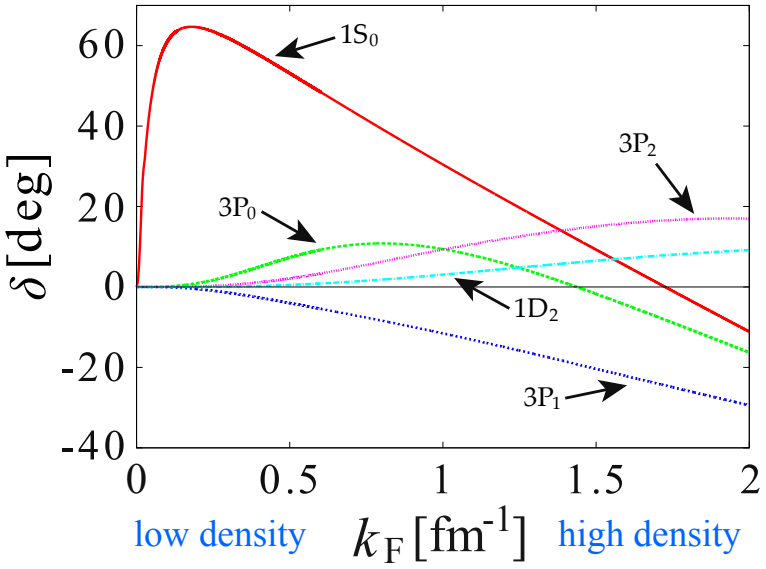

Figure 1.13: Phase shift $\delta(k_F)$ reconstructed from partial wave analysis on neutron-proton scattering data. If we assume isospin symmetry, this figure also approximately describes the neutron-neutron interaction [66]. Note that the s-wave interaction ($^1S_0$) is dominant in the low-density region ($k_F \lesssim 1.7$ fm^{-1}).

ignore the nuclear lattice, and to focus on the neutron liquid [47–49].

To connect neutron star physics and cold Fermi gas physics, we conveniently show in Fig.1.13 the phase shift data of neutron-proton interaction. Since the so-called isospin-symmetry approximately holds between proton and neutron [66], Fig.1.13 may also be viewed as the phase shift data of interacting neutrons. This figure clearly shows the low density region ($k_F \lesssim 1$ fm^{-1}) is dominated by the s-wave interaction ($^1S_0$ in Fig.1.13), which is characterised by the s-wave scattering length [67]

$$a_s = -18.5 \text{ fm}, \tag{1.11}$$

as well as the associated effective range

$$r_{\text{eff}} = 2.7 \text{ fm}. \tag{1.12}$$

In the effective range theory, these are related to the phase shift $\delta\left(^1S_0\right)$ as [68, 69]

$$k \cot \delta\left(^1S_0\right) \simeq -\frac{1}{a_s} + \frac{1}{2} r_{\text{eff}} k^2. \tag{1.13}$$

In the low density region $0 \leq k_F \lesssim 1$ fm^{-1} in the crust regime of a neutron star, using the typical value $k_F = 1$ fm^{-1}, one finds the value of the scaled interaction $(k_F a_s)^{-1}$ as

$$(k_F a_s)^{-1} = \frac{1}{-18.5} \simeq -0.054, \tag{1.14}$$

that is, the system is close to the unitarity limit ($(k_F a_s)^{-1} = 0$). Because of this strong pairing interaction in the $^1S_0$ Cooper channel, neutrons are considered to be nearly in the s-wave superfluid groundstate. Note that, although the temperature from the surface to the core of a neutron star is expected to vary from $T \sim 10^6$ K to $T \sim 10^9$ K, due to the large density, the scaled temperature $T/T_F \ll 1$, because

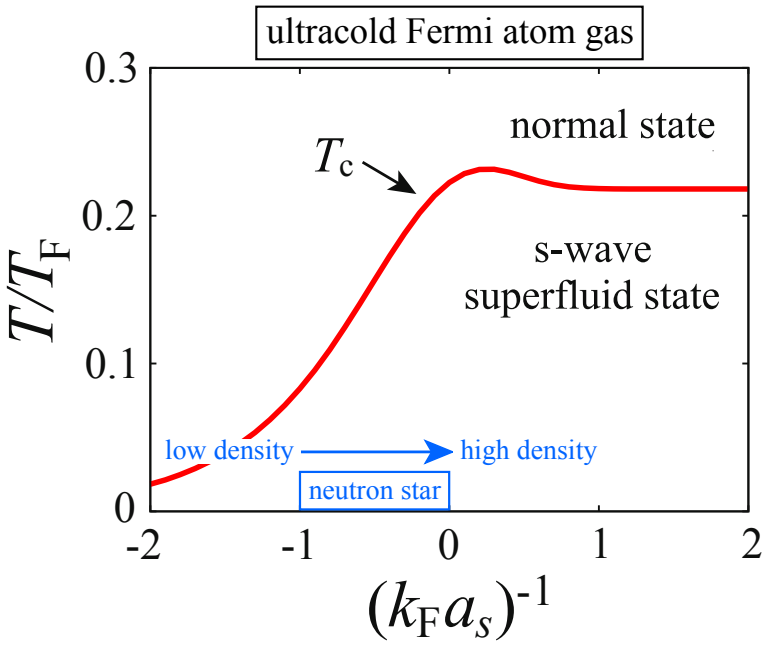

Figure 1.14: Phase diagram of an ultracold Fermi gas in the BCS-BEC crossover region. "neutron star" is the region where the system situation is very similar to the low density crust regime of a neutron star interior. The interaction strength is measured in terms of the inverse s-wave scattering length a_s^{-1}, normalized by the Fermi momentum k_F. In this scale, the strength of an s-wave pairing interaction increases with increasing the value of $(k_F a_s)^{-1}$. The unitarity limit is as $(k_F a_s)^{-1} = 0$.

of the high density. Thus, neutron fluid in the crust regime is similar to the unitary regime of a superfluid Fermi gas far below T_c.

In addition to this similarity, we also point out that, although the s-wave scattering length $a_s = -18.5$ fm is fixed in the neutron star case, the "scaled interaction $(k_F a_s)^{-1}$" varies as one goes inside the neutron star from the surface, because k_F increases with increasing the neutron density. This situation can also be realised in a superfluid Fermi gas, where $(k_F a_s)^{-1}$ can be tuned by adjusting the value of the scattering length a_s by using the Feshbach resonance technique.

Because physical properties of an ultracold Fermi gas do not depend on the detailed constituent Fermi atoms (^{6}Li or ^{40}K), we expect any experimental results done in the blue region shown in Fig.1.14 should be readily applicable to the neutron matter case. This analogy indicates that the recent measurement of the internal energy (equation of state (EOS)) of a ^{6}Li superfluid Fermi gas in the "neutron star" region in Fig.1.14 (see Fig.1.7 (b)) may be useful for investigating the neutron star EOS. Since the recent discovery of the massive neutron stars PSR J1614-2230 (with a mass $M = 1.97 \pm 0.04 M_\odot$) using the Shapiro delay [70], and PSR J0348+0342 ($M = 2.01 \pm 0.04 M_\odot$) [71], the EOS of a neutron star has attracted much attention, because many proposed EOS cannot explain such a heavy star [70–74]. This problem is sometimes referred to as the two-solar mass problem, and is one of the hottest topics in neutron star physics.

The reason why EOS is considered as a critical key to solve the two-solar mass problem is that, together with the Tolman-Oppenheimer-Volkov (TOV) equation [75, 76] (giving the balance between star gravity and internal pressure), EOS enables us to give relation between the stars mass M and the radius R [77]. This so-called M-R relation conveniently gives the upper limit of the neutron star mass, so that the precise EOS is necessary for knowing this limit, as well as solving the two-solar mass problem.

The nearest neutron star RX J1856.5-3754 is 400 light-years away from the earth [78]. Thus, although many neutron stars have already been discovered [70], this long distance prevents us from directly determining EOS by astronomical observations. Although, neutron hallows [79, 80] and skins [81, 82] in neutron-rich nuclei give some information about neutron matter, since these are few-body systems, it is still not enough to construct the neutron star EOS, including many-body effects associated with strong neutron-neutron interactions [64].

Because of these experimental difficulties, the current approaches to the neutron star EOS heavily relies on theoretical calculations based on Monte Carlo methods [49, 83–85]. Since these methods employ a realistic pseudopotential which is calibrated to few-body nucleon scattering experiments [49, 66, 83–85], these approaches are supported by experiments to some extent. However, many-body effects are a fully theoretical challenge with no experimental support.

It is exactly this point where ultracold Fermi gases can make a significant contribution to the investigation of the neutron star EOS, because many-body effects associated with a strong pairing interaction are inherent in there. Indeed, as shown in Fig.1.7 (b), the observed EOS in the BCS-unitary regime deviates from mean-field BCS-Leggett theory, indicating the importance of many-body correlations beyond the mean-field level.

However, in order to use the recent experiment on a ^{6}Li superfluid Fermi gas shown in Fig.1.7 (b) as data from a "cold Fermi gas quantum simulator" for the study of the neutron star EOS, we need to correct the data so as to be able to replicate the crust regime of a neutron star interior. That is, while the effective range $r_{\rm eff}$ is negligibly small in an ultracold Fermi gas, one can't ignore $r_{\rm eff} = 2.7$ fm [67] in the neutron star case. At present, it is difficult to experimentally tune the value of $r_{\rm eff}$ in cold atom physics. We thus need to make up for this difference in a theoretical manner.

Although this is still a theoretical challenge, we could resolve ambiguity coming from such theoretical manipulation, when we employ a reliable strong-coupling theory which can, at least, well explain the experimental results shown in Fig.1.7. In this thesis, we take this strategy, to evaluate the neutron star EOS in the low-density crust regime.

We briefly note that, as seen in Fig.1.13, non-s-wave interaction channels, as well as three-body forces [61, 86, 87], become important in the deeper region of a neutron star interior, which cannot be "quantum-simulated" by an s-wave superfluid Fermi gas. In this regard, however, a tunable p-wave interaction associated with a p-wave Feshbach resonance has been realised [36]. In addition, in the context of

the so-called Bose nova phenomenon [42], a three-body interaction effect has also been discussed. Thus, utilising these could make the experiments on cold atoms more effective in studying the deeper regions of the neutron star EOS in the future.

1.5 Purpose And Organisation Of This Thesis

In this thesis, we theoretically investigate strong-coupling properties of an ultracold Fermi gas. Including pairing fluctuations within the framework of the strong-coupling theory developed by Nozières and Schmitt-Rink (NSR), we evaluate the specific heat at constant volume C_V, over the entire BCS-BEC crossover region. This thermodynamic quantity, which has recently been measured in a ^{6}Li unitary Fermi gas, is ideal for studying how strong pairing fluctuations affect properties of the system. Analysing detailed temperature dependence of C_V, we determine the region where pairing fluctuations dominate over system properties, as well as the region where the system may be viewed as a gas of stable molecular bosons, in the phase diagram of an ultracold Fermi gas with respect to the temperature and the interaction strength.

We also explore the possibility of using an ultracold Fermi gas as a quantum simulator for the study of other systems. In contrast to the ordinary approach that aims to replicate a target system by this atomic gas, our idea is to simply use the situation which has already been experimentally realised, and to make up for the difference of a target system in a theoretical manner. To demonstrate this, we pick up the neutron star EOS in the low-density crust regime. After confirming that the NSR theory extended to the superfluid phase below T_c can well explain the observed EOS in the BCS-unitary region of a ^{6}Li superfluid Fermi gas, we further extend this scheme to include the non-vanishing effective range ($r_{\rm eff} = 2.7$ fm) which is crucial for the neutron star case. The calculated neutron star EOS is found to agree well with the previous work in nuclear physics, where realistic neutron-neutron interactions are taken into account.

The outline of this thesis is as follows. In Chap.2, we present our theoretical formulation. The NSR theory, as well as its extension to the superfluid phase are explained. We also explain how to incorporate effects of a non-vanishing effective range into the NSR theory, for the study of the neutron star in the low density region. In Chap.3 we show our results of the specific heat C_V in the BCS-BEC crossover regime of an ultracold Fermi gas. In the normal state, we introduce two characteristic temperatures $\tilde{T}$ and $\bar{T}$ from the detailed temperature dependence of this thermodynamic quantity. Using these we identify the region where pairing fluctuations are crucial for system properties, as well as the region where the system may be viewed as a molecular Bose gas, rather than a Fermi gas, in the phase diagram with respect to temperature and interaction strength. We also show the behaviour of C_V below T_c is rather simple, in the sense that it simply decreases with temperature in the whole BCS-BEC crossover region. At the unitarity we compare our results with the recent experiment on a ^{6}Li Fermi gas. In Chap.4, we deal with the neutron star EOS. We first show that the NSR theory extended to the superfluid state below T_c well explains the observed EOS in the BCS-unitary region of a ^{6}Li superfluid Fermi gas far below T_c. Keeping in mind that this region is similar to the crust regime of a neutron star interior, we further extended the

superfluid NSR theory, to include the non-vanishing effective range $r_{\rm eff} = 2.7$ fm of an s-wave neutron-neutron interaction. We then compare the calculated EOS with the previous work obtained by nuclear physics. In Chap.5, we summarise this thesis.

Throughout this thesis, we set $\hbar = k_{\rm B} = 1$, and take the system volume $V = 1$, for simplicity.

Chapter 2

Strong Coupling Formalism For Attractively Interacting Fermi Systems

In this chapter we, explain the strong-coupling theory we employ in this thesis to study thermodynamic properties of an ultracold Fermi gas in the BCS-BEC crossover region. We also extend this theoretical framework to include a non-vanishing effective range $r_{\rm eff}$, being necessary for the neutron star case. In Sec. 2.1, we explain a strong-coupling theory developed by Nozières and Schmitt-Rink (NSR) [15]. In Sec. 2.2 we extend this to the superfluid phase below the superfluid phase transition temperature $T_{\rm c}$. These are used to evaluate thermodynamic quantities, such as the specific heat and internal energy, in Chaps 3 and 4. In Sec. 2.3, we further extend the NSR formalism below $T_{\rm c}$, to include effects of non-vanishing effective range $r_{\rm eff}$, which is applied to the study of the equation of state of a neutron star in the low density crust regime in Chap. 4.

2.1 Strong Coupling Theory In The Normal State

2.1.1 Model Hamiltonian

We consider a two-component Fermi system described by the Hamiltonian $H = H_0 + H_{\rm I}$, where

$$H_0 = \sum_{\boldsymbol{p},\sigma} \xi_{\boldsymbol{p}} c^\dagger_{\boldsymbol{p},\sigma} c_{\boldsymbol{p},\sigma} \tag{2.1}$$

is the kinetic term, and

$$H_{\rm I} = -\sum_{\boldsymbol{p},\boldsymbol{p}',\boldsymbol{q}} U(\boldsymbol{p}-\boldsymbol{p}') c^\dagger_{\boldsymbol{p}+\boldsymbol{q}/2,\uparrow} c^\dagger_{-\boldsymbol{p}+\boldsymbol{q}/2,\downarrow} c_{-\boldsymbol{p}'+\boldsymbol{q}/2,\downarrow} c_{\boldsymbol{p}'+\boldsymbol{q}/2,\uparrow}. \tag{2.2}$$

is the interaction term.

For Eq.(2.1), $\xi_{\boldsymbol{p}} = \varepsilon_{\boldsymbol{p}} - \mu = \boldsymbol{p}^2/(2m) - \mu$ is the kinetic energy of a Fermi particle with mass m, measured from the Fermi chemical potential μ. In the case of an ultracold Fermi gas this particle is a ^{40}K or ^{6}Li Fermi atom. For the neutron star case, this is a neutron. $c_{\boldsymbol{p},\sigma}$ is the annihilation operator of a Fermi particle with spin $\sigma =\uparrow,\downarrow$ (in an ultracolf Fermi gas $\sigma =\uparrow,\downarrow$ are actually pseudospins,

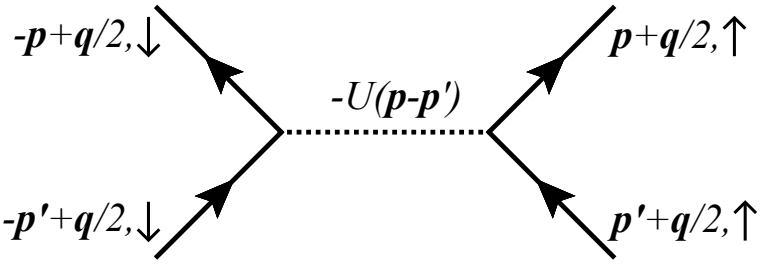

Figure 2.1: Feynman diagram describing the pairing interaction term in $H_{\rm I}$ in Eq.(2.2). The solid and dotted lines describe the bare single-particle Green's function in Eq.(2.15) and the coupling $-U(\boldsymbol{p}-\boldsymbol{p}') < 0$, respectively.

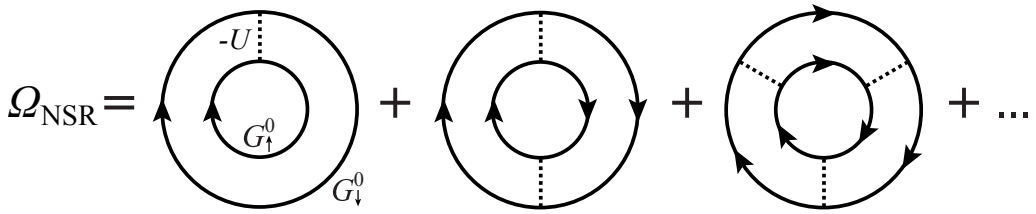

Figure 2.2: Diagrammatic representation of fluctuation correction $\Omega_{\rm NSR}$ to the thermodynamic potential Ω in the NSR theory[15]. The solid line is the bare single-particle Green's function $G^0_{\sigma=\uparrow,\downarrow}$ in Eq.(2.18).The dashed line represents the attractive interaction $-U < 0$.

describing two different atomic hyperfine states contributing to the pair formation). The interaction term in Eq.(2.2) describes an attractive two body interaction ($-U(\boldsymbol{p}-\boldsymbol{p}') < 0$), which is diagrammatically described as Fig.2.1.

In the BCS-BEC crossover regime of an ultracold Fermi gas, the attractive pairing interaction in Eq.(2.2) is known to be well described by a contact-type s-wave one. That is, one may simply take the coupling $-U(\boldsymbol{p}-\boldsymbol{p}')$ as a constant $-U < 0$. For this "cold Fermi gas case", Eq.(2.2) is simplified as

$$H_{\rm I} = -U \sum_{\boldsymbol{p},\boldsymbol{p}',\boldsymbol{q}} c^{\dagger}_{\boldsymbol{p}+\boldsymbol{q}/2,\uparrow} c^{\dagger}_{-\boldsymbol{p}+\boldsymbol{q}/2,\downarrow} c_{-\boldsymbol{p}'+\boldsymbol{q}/2,\downarrow} c_{\boldsymbol{p}'+\boldsymbol{q}/2,\uparrow}. \tag{2.3}$$

In the following, using Eq.(2.3) we first explain the strong-coupling BCS-BEC crossover theory above $T_{\rm c}$ developed by Nozières and Schmitt-Rink (NSR) [15], and its extension to the superfluid phase below $T_{\rm c}$. We will explain a more general case (Eq.(2.2)) in Sec.2.3.

2.1.2 NSR Theory In The Normal State

In the NSR theory [15], strong-coupling effects associated with the pairing interaction in Eq.(2.3) can conveniently be incorporated into the theory by taking into account fluctuation corrections to the thermodynamic potential Ω shown in Fig.(2.2). To evaluate the NSR correction $\Omega_{\rm NSR}$ in Fig.(2.2) we rewrite the partition function Z as

$$Z = {\rm tr} e^{-H/T} = {\rm tr}\left[e^{-H_0/T} R_{\rm I}(T)\right], \tag{2.4}$$

where

$$R_{\rm I}(T) = e^{H_0/T} e^{-H/T}. \tag{2.5}$$

The thermodynamic potential Ω is then given by

$$\begin{aligned}\Omega &= -T \log\left[\mathrm{tr}\left[e^{-H_0/T} R_{\rm I}(T)\right]\right] \\ &= -T\left[\log\left[\mathrm{tr} e^{-H_0/T}\right] + \log\left[\frac{\mathrm{tr}\left[e^{-H_0/T} R_{\rm I}(T)\right]}{\mathrm{tr} e^{-H_0/T}}\right]\right] \\ &= \Omega_0 + \Omega_{\rm I},\end{aligned} \tag{2.6}$$

where

$$\Omega_0 = -T \log\left[\mathrm{tr} e^{-H_0/T}\right] = -2T \sum_{\boldsymbol{p}} \log\left[1 + e^{-\xi_{\boldsymbol{p}}/T}\right] \tag{2.7}$$

is the thermodynamic potential of a free Fermi gas, and

$$\Omega_{\rm I} = -T \log \langle R_{\rm I}(T) \rangle_0 \tag{2.8}$$

describe interaction corrections to the thermodynamic potential.

Using the so-called linked cluster theorem [88], one can rewrite the correction term in Eq.(2.8) as

$$\Omega_{\rm I} = -T \log \langle R_{\rm I}(T) \rangle_0 = -T\left[\langle R_{\rm I}(T) \rangle_0^c - 1\right]. \tag{2.9}$$

Here, the superscript "c" means that only connected diagrams are retained.

Noting that $R_{\rm I}(1/\beta)$ in Eq.(2.5) satisfies ($\beta = 1/T$)

$$\begin{aligned}\partial_\beta R_{\rm I}(1/\beta) &= H_0 R_{\rm I}(\beta) - e^{\beta H_0}(H_0 + H_{\rm I}) e^{-\beta(H_0+H_{\rm I})} \\ &= -\tilde{H}_{\rm I}(\beta) R_{\rm I}(1/\beta),\end{aligned} \tag{2.10}$$

(where $\tilde{H}_{\rm I}(\beta) = e^{\beta H_0} H_{\rm I} e^{-\beta H_0}$), we find

$$R_{\rm I}(1/\beta) = \mathrm{T}_\tau \exp\left[-\int_0^\beta \mathrm{d}\tau\, \tilde{H}_{\rm I}(\tau)\right]. \tag{2.11}$$

Here T_τ is the time ordered product for the imaginary time τ. Substitution of Eq.(2.11) into Eq.(2.9) gives,

$$\begin{aligned}\Omega_{\rm I} &= -\frac{1}{\beta}\left[\left\langle \mathrm{T}_\tau \exp\left[-\int_0^\beta \mathrm{d}\tau\, \tilde{H}_{\rm I}(\tau)\right]\right\rangle_0^c - 1\right] \\ &= -\frac{1}{\beta}\sum_{n=1}^{\infty}\frac{1}{n!}\left\langle \mathrm{T}_\tau\left[-\int_0^\beta \mathrm{d}\tau\, \tilde{H}_{\rm I}(\tau)\right]^n\right\rangle_0^c,\end{aligned} \tag{2.12}$$

which enables us to evaluate the fluctuation correction term $\Omega_{\rm I}$ in a perturbative manner.

The first order correction ($\equiv \Omega^{(1)}_{\rm NSR}$) in terms of $\tilde{H}_{\rm I}$ is given by

$$\begin{aligned}\Omega^{(1)}_{\rm NSR} &= -\frac{1}{\beta}\left\langle \mathrm{T}_\tau\left[-\int_0^\beta \mathrm{d}\tau\, \tilde{H}_{\rm I}(\tau)\right]\right\rangle_0^c \\ &= -\frac{U}{\beta}\sum_{\boldsymbol{p},\boldsymbol{p}',\boldsymbol{q}}\int_0^\beta \mathrm{d}\tau \left\langle \mathrm{T}_\tau\left[\hat{c}^\dagger_{\boldsymbol{p}+\boldsymbol{q}/2,\uparrow}(\tau_+)\hat{c}^\dagger_{-\boldsymbol{p}+\boldsymbol{q}/2,\downarrow}(\tau_+)\hat{c}_{-\boldsymbol{p}'+\boldsymbol{q}/2,\downarrow}(\tau)\hat{c}_{\boldsymbol{p}'+\boldsymbol{q}/2,\uparrow}(\tau)\right]\right\rangle_0^c.\end{aligned} \tag{2.13}$$

In the second line in Eq.(2.13), an infinitesimal shift $\tau \to \tau_+ = \tau + \delta$ $(0 < \delta \ll 1)$ has been introduced to preserve causality. $\Omega^{(1)}_{\rm NSR}$ corresponds to the first diagram in Fig.2.2. Using the Bloch-De Dominicis theorem [88], we can evaluate $\langle \cdots \rangle^c_0$ in Eq.(2.13) as

$$\begin{aligned}
&\left\langle \mathrm{T}_\tau \left[\hat{c}^\dagger_{\boldsymbol{p}+\boldsymbol{q}/2,\uparrow}(\tau_+)\, \hat{c}^\dagger_{-\boldsymbol{p}+\boldsymbol{q}/2,\downarrow}(\tau_+)\, \hat{c}_{-\boldsymbol{p}'+\boldsymbol{q}/2,\downarrow}(\tau)\, \hat{c}_{\boldsymbol{p}'+\boldsymbol{q}/2,\uparrow}(\tau) \right] \right\rangle^c_0 \\
=&\left\langle \mathrm{T}_\tau \left[\hat{c}^\dagger_{\boldsymbol{p}+\boldsymbol{q}/2,\uparrow}(\tau_+)\, \hat{c}^\dagger_{-\boldsymbol{p}+\boldsymbol{q}/2,\downarrow}(\tau_+) \right] \right\rangle_0 \left\langle \mathrm{T}_\tau \left[\hat{c}_{-\boldsymbol{p}'+\boldsymbol{q}/2,\downarrow}(\tau)\, \hat{c}_{\boldsymbol{p}'+\boldsymbol{q}/2,\uparrow}(\tau) \right] \right\rangle_0 \\
+&\left\langle \mathrm{T}_\tau \left[\hat{c}^\dagger_{\boldsymbol{p}+\boldsymbol{q}/2,\uparrow}(\tau_+)\, \hat{c}_{\boldsymbol{p}'+\boldsymbol{q}/2,\uparrow}(\tau) \right] \right\rangle_0 \left\langle \mathrm{T}_\tau \left[\hat{c}^\dagger_{-\boldsymbol{p}+\boldsymbol{q}/2,\downarrow}(\tau_+)\, \hat{c}_{-\boldsymbol{p}'+\boldsymbol{q}/2,\downarrow}(\tau) \right] \right\rangle_0 \\
-&\left\langle \mathrm{T}_\tau \left[\hat{c}^\dagger_{\boldsymbol{p}+\boldsymbol{q}/2,\uparrow}(\tau_+)\, \hat{c}_{-\boldsymbol{p}'+\boldsymbol{q}/2,\downarrow}(\tau) \right] \right\rangle_0 \left\langle \mathrm{T}_\tau \left[\hat{c}^\dagger_{-\boldsymbol{p}+\boldsymbol{q}/2,\downarrow}(\tau_+)\, \hat{c}_{\boldsymbol{p}'+\boldsymbol{q}/2,\uparrow}(\tau) \right] \right\rangle_0 \\
=&\delta_{\boldsymbol{p},\boldsymbol{p}'}\, G^0_\uparrow(\boldsymbol{p}+\boldsymbol{q}/2, \tau-\tau_+)\, G^0_\downarrow(-\boldsymbol{p}+\boldsymbol{q}/2, \tau-\tau_+)\,,
\end{aligned} \tag{2.14}$$

where

$$G^0_\sigma(\boldsymbol{p}, \tau-\tau') = -\left\langle \mathrm{T}_\tau \left[\hat{c}_{\boldsymbol{p},\sigma}(\tau_+)\, \hat{c}^\dagger_{\boldsymbol{p},\sigma}\left(\tau'\right) \right] \right\rangle_0 . \tag{2.15}$$

is the bare single-particle thermal Green's function. We briefly note that $\left\langle \hat{c}^\dagger_\uparrow \hat{c}^\dagger_\downarrow \right\rangle_0$, $\left\langle \hat{c}_\downarrow \hat{c}_\uparrow \right\rangle_0$, $\left\langle \hat{c}^\dagger_\uparrow \hat{c}_\downarrow \right\rangle_0$, and $\left\langle \hat{c}^\dagger_\downarrow \hat{c}_\uparrow \right\rangle_0$ identically vanish due to the thermal average $\langle \cdots \rangle_0$ in terms of over H_0.

The resulting Eq.(2.13) has the form,

$$\begin{aligned}
\Omega^{(1)}_{\rm NSR} &= -\frac{U}{\beta} \sum_{\boldsymbol{p},\boldsymbol{q}} \int_0^\beta \mathrm{d}\tau\, G^0_\uparrow(\boldsymbol{p}+\boldsymbol{q}/2, \tau-\tau_+)\, G^0_\downarrow(-\boldsymbol{p}+\boldsymbol{q}/2, \tau-\tau_+) \\
&= -\frac{U}{\beta} \sum_{\boldsymbol{q}, i\nu_n} e^{i\nu_n \delta} \Pi(\boldsymbol{q}, i\nu_n)\,,
\end{aligned} \tag{2.16}$$

where

$$\Pi(\boldsymbol{q}, i\nu_n) = \frac{1}{\beta} \sum_{\boldsymbol{p}, i\omega_m} G^0_\uparrow(\boldsymbol{p}+\boldsymbol{q}/2, i\omega_m + i\nu_n)\, G^0_\downarrow(-\boldsymbol{p}+\boldsymbol{q}/2, -i\omega_m) \tag{2.17}$$

is the lowest-order pair-correlation function, physically describing fluctuations in the Cooper channel. In Eq.(2.17) ω_n=$\pi(2n+1)T$ and ν_n=$2\pi nT$ $(n = 0, \pm 1, \pm 2, \dots)$ are the Fermi and Bose Matsubara frequency, respectively. The single-particle thermal Green's function

$$G^0_\sigma(\boldsymbol{p}, i\omega_m) = \frac{1}{i\omega_m - \xi_{\boldsymbol{p}}}. \tag{2.18}$$

is related to $G^0_\sigma(\boldsymbol{p}, \tau)$ in Eq.(2.15) as

$$G^0_\sigma(\boldsymbol{p}, \tau) = \frac{1}{\beta} \sum_{i\omega_n} e^{-i\omega_n \tau} G^0_\sigma(\boldsymbol{p}, i\omega_n)\,. \tag{2.19}$$

Substituting Eq.(2.18) into Eq.(2.17), one can carry out the ω_m-summation, giving

$$\Pi(\boldsymbol{q}, i\nu_n) = -\sum_{\boldsymbol{p}} \frac{1 - n_{\rm F}\left(\xi_{\boldsymbol{p}+\boldsymbol{q}/2}\right) - n_{\rm F}\left(\xi_{-\boldsymbol{p}+\boldsymbol{q}/2}\right)}{i\nu_n - \xi_{\boldsymbol{p}+\boldsymbol{q}/2} - \xi_{-\boldsymbol{p}+\boldsymbol{q}/2}}, \tag{2.20}$$

where

$$n_{\rm F}\left(\xi_{\boldsymbol{p}}\right) = \frac{1}{e^{\xi_{\boldsymbol{p}}/T} + 1} \tag{2.21}$$

is the Fermi distribution function.

The second-order correction ($n = 2$ in Eq.(2.12)) can also be evaluated in the same manner. This correction ($\equiv \Omega^{(2)}_{\rm NSR}$) corresponds to the second diagram in Fig.2.2, having the form,

$$\Omega^{(2)}_{\rm NSR} = -\frac{U^2}{2\beta}\sum_{\boldsymbol{q},i\nu_n} e^{i\nu_n\delta}\left[\Pi\left(\boldsymbol{q},i\nu_n\right)\right]^2. \tag{2.22}$$

For higher corrections ($n \geq 3$ in Eq.(2.12)) the NSR scheme only retains the terms describing pairing fluctuations that are diagrammatically drawn as double-ring diagrams, where two Green's functions propagate in the same direction (see, for example, the third diagram in Fig.2.2). Summing these up, we obtain

$$\begin{aligned}\Omega_{\rm NSR} &= \Omega^{(1)}_{\rm NSR} + \Omega^{(2)}_{\rm NSR} + \Omega^{(3)}_{\rm NSR} + \cdots \\ &= -T\sum_{\boldsymbol{q},i\nu_n} e^{i\nu_n\delta}\sum_{m=1}^{\infty}\frac{U^m}{m}\left[\Pi\left(\boldsymbol{q},i\nu_n\right)\right]^m \\ &= -T\sum_{\boldsymbol{q},i\nu_n} e^{i\nu_n\delta}\ln\Gamma(\boldsymbol{q},i\nu_n),\end{aligned} \tag{2.23}$$

where

$$\Gamma(\boldsymbol{q},i\nu_n) = \frac{-U}{1-U\Pi(\boldsymbol{q},i\nu_n)} \tag{2.24}$$

is the particle-particle scattering matrix.

Due to the contact type interaction U in Eq.(2.3), the pair-correlation function $\Pi(\boldsymbol{q},i\nu_n)$ in Eq.(2.17) exhibits an ultraviolet divergence, requiring the introduction of an artificial momentum cutoff $p_{\rm c}$. To remedy this, we introduce the s-wave scattering length a_s, being related to the bare interaction $-U$ as

$$\frac{4\pi a_s}{m} = \frac{-U}{1-U\sum_{\boldsymbol{p}}^{p_{\rm c}}\frac{1}{2\varepsilon_{\boldsymbol{p}}}}, \tag{2.25}$$

where $p_{\rm c}$ is a cutoff momentum (which is actually taken to be infinitely large).

We briefly note that a_s is experimentally accessible in cold atom physics [9]. Using the scattering length a_s, we can rewrite the particle-praticle scattering matrix $\Gamma(\boldsymbol{q},i\nu_n)$ in Eq.(2.24) into the cutoff-free form,

$$\Gamma(\boldsymbol{q},i\nu_n) = \frac{1}{\dfrac{m}{4\pi a_s} + \left[\Pi(\boldsymbol{q},i\nu_n) - \displaystyle\sum_{\boldsymbol{p}}\frac{1}{2\varepsilon_{\boldsymbol{p}}}\right]}. \tag{2.26}$$

Note that the ultraviolet divergence in $\Pi(\boldsymbol{q},i\nu_n)$ is canceled out by $\sum_{\boldsymbol{p}} 1/(2\varepsilon_{\boldsymbol{p}})$ in Eq.(2.26).

In cold atom physics, the strength of a pairing interaction is frequently measured in terms of the inverse scattering length a_s^{-1}, normalised by the Fermi wave length $k_{\rm F}$. In this scale the weak coupling BCS and strong coupling BEC regions are, respectively, characterised as $(k_{\rm F}a_s)^{-1} \lesssim -1$ and $(k_{\rm F}a_s)^{-1} \gtrsim 1$. The (BCS-BEC) crossover region is described by $-1 \lesssim (k_{\rm F}a_s)^{-1} \lesssim 1$.

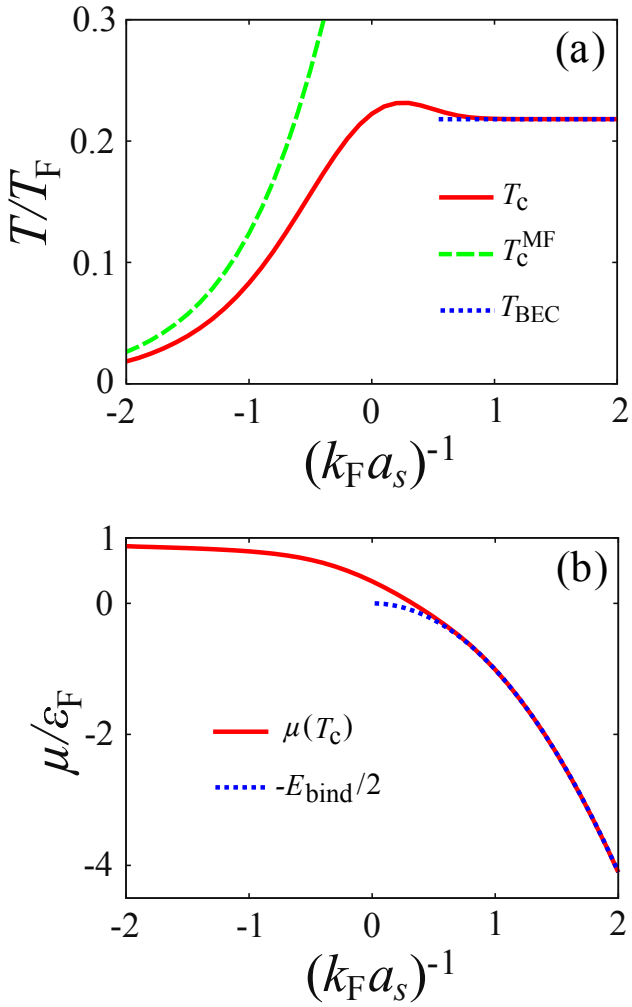

Figure 2.3: Calculated superfluid phase transition temperature T_c (a), as well as the Fermi chemical potential μ at T_c (b) in the BCS-BEC crossover region. The strength of the pairing interaction in measured in terms of the inverse scattering length a_s^{-1}, normalised by the Fermi wavelength k_F. T_F and ε_F are the Fermi temperature and Fermi energy, respectively. In panel (a), T_c^{MF} is the result in the mean-field BCS theory. "T_{BEC} " shows the BEC transition temperature of an $N/2$ ideal Bose gas with molecular mass $M = 2m$ (see Eq.(2.31)).

In the NSR scheme, the superfluid phase transition temperature T_c is determined from the Thouless criterion [15, 16, 19, 28, 90], stating that the particle-particle scattering matrix $\Gamma(\boldsymbol{q}, i\nu_n)$ has a pole in the low energy and long wavelength limit ($\boldsymbol{q} = \boldsymbol{0}, i\nu_n = 0$). The resulting T_c-equation has the same form as the mean field BCS theory, that is

$$1 = -\frac{4\pi a_s}{m}\sum_{\boldsymbol{p}}\left[\frac{1}{2\xi_{\boldsymbol{p}}}\tanh\frac{\xi_{\boldsymbol{p}}}{2T} - \frac{1}{2\varepsilon_{\boldsymbol{p}}}\right]. \tag{2.27}$$

However, while the Fermi chemical potential in Eq.(2.27) can be safely taken to be equal to the Fermi energy ε_F in the conventional BCS theory [89], it is known to deviate from ε_F in the BCS-BEC crossover regime. In the NSR theory, this strong-coupling correction is taken into account by solving the equation for

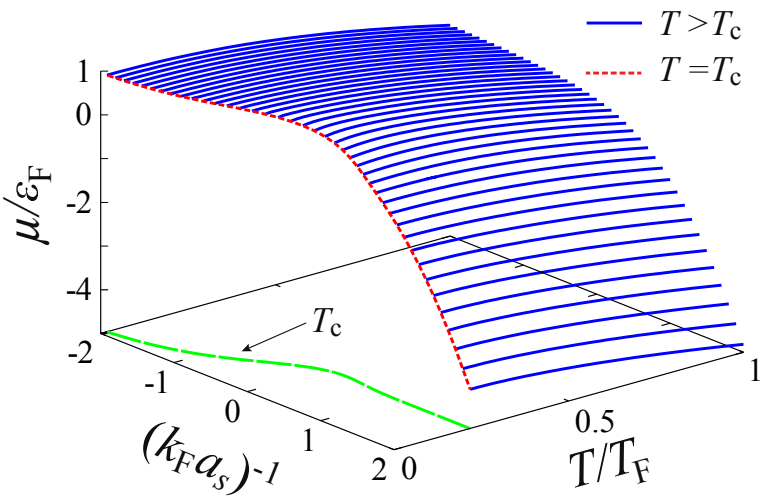

Figure 2.4: Calculated Fermi chemical potential μ in the normal state above T_c.

the number N of Fermi atoms, which is obtained from the NSR thermodynamic potential $\Omega = \Omega_0 + \Omega_{\rm NSR}$ (Eqs (2.7) and (2.23)) by using the identity

$$N = -\left(\frac{\partial \Omega}{\partial \mu}\right)_T = N_0 + N_{\rm NSR}. \tag{2.28}$$

Here

$$N_0 = -\left(\frac{\partial \Omega_0}{\partial \mu}\right)_T = 2\sum_{\boldsymbol{p}} n_{\rm F}\left(\xi_{\boldsymbol{p}}\right), \tag{2.29}$$

and

$$\begin{aligned} N_{\rm NSR} &= -\left(\frac{\partial \Omega_{\rm NSR}}{\partial \mu}\right)_T \\ &= -T\sum_{\boldsymbol{q}, i\nu_n} \Gamma(\boldsymbol{q}, i\nu_n)\frac{\partial \Pi(\boldsymbol{q}, i\nu_n)}{\partial \mu}. \end{aligned} \tag{2.30}$$

For a given interaction strength $(k_{\rm F}a_s)^{-1}$, we solve the T_c-equation (2.27), together with the number equation (2.28), to self-consistently determine T_c and $\mu(T_c)$. Above T_c, we only deal with the number equation (2.28), to determine $\mu(T > T_c)$ for a given parameter set $((k_{\rm F}a_s)^{-1}, T)$.

Figure 2.3 shows the self-consistent solution for the coupled T_c-equation (2.27) with the number equation (2.28) in the BCS-BEC crossover regime of an ultracold Fermi gas. In panel (a), starting from the weak-coupling BCS regime ($(k_{\rm F}a_s)^{-1} \lesssim -1$), the superfluid phase transition temperature gradually deviates from the weak-coupling BCS results ($T_c^{\rm MF}$), to approach the BEC transition temperature of an $N_{\rm B} = N/2$ ideal molecular Bose gas with molecular mass $M = 2m$,

$$T_{\rm BEC} = \frac{\pi}{m}\left(\frac{N}{2\zeta\left(\frac{3}{2}\right)}\right)^{2/3} = 0.218 T_{\rm F}, \tag{2.31}$$

in the strong coupling regime ($(k_{\rm F}a_s)^{-1} \gtrsim 1$). Correspondingly, the Fermi chemical potential, $\mu(T = T_c)$, becomes negative, to approach half the binding energy

$E_{\rm bind} = 1/ma_s^2$ in the BEC regime, as shown in Fig.2.3 (b).

In addition to the solution at $T_{\rm c}$, we also show the calculated Fermi chemical potential μ above $T_{\rm c}$ in Fig.2.4. We will use these results in numerically evaluating the specific heat at constant volume C_V in Chap.3.

2.1.3 Internal Energy And Specific Heat Above $T_{\rm c}$

An advantage of the NSR theory is that this strong-coupling theory is based on the thermodynamic potential Ω. Because of this, once the Fermi chemical potential $\mu(T \geq T_{\rm c})$, as well as $T_{\rm c}$, are determined in this theory, we can evaluate various thermodynamic quantities that are related to Ω. The internal energy E is, for example, obtained via the Legendre transformation [60],

$$\begin{aligned} E &= \Omega + TS + \mu N \\ &= \Omega - T\left(\frac{\partial\Omega}{\partial T}\right)_{\mu} - \mu\left(\frac{\partial\Omega}{\partial\mu}\right)_{T} \\ &= E_0 + E_{\rm NSR}. \end{aligned} \tag{2.32}$$

Here

$$E_0 = 2\sum_{\boldsymbol{p}} \varepsilon_{\boldsymbol{p}} n_{\rm F}\left(\xi_{\boldsymbol{p}}\right), \tag{2.33}$$

is the non-interacting part, and

$$E_{\rm NSR} = -T\sum_{\boldsymbol{q},i\nu_n} \Gamma(\boldsymbol{q}, i\nu_n)\left[T\frac{\partial}{\partial T}\Pi(\boldsymbol{q}, i\nu_n) + \mu\frac{\partial}{\partial\mu}\Pi(\boldsymbol{q}, i\nu_n)\right] \tag{2.34}$$

involves effects of pairing fluctuations, described by $\Gamma(\boldsymbol{q}, i\nu_n)$ and $\Pi(\boldsymbol{q}, i\nu_n)$.

In Chap.3, we examine the specific heat at constant volume C_V, to construct the phase diagram of an ultracold Fermi gas. This thermodynamic quantity is related to the internal energy E in Eq.(2.32) as [60]

$$C_V = \left(\frac{\partial E}{\partial T}\right)_N. \tag{2.35}$$

Analytically, noting that the derivative in Eq.(2.35) must be taken with the total number N of particles being fixed, we actually need to calculate Eq.(2.35) as

$$C_V = \left(\frac{\partial E}{\partial T}\right)_{\mu} + \left(\frac{\partial\mu}{\partial T}\right)_N \left(\frac{\partial E}{\partial\mu}\right)_T, \tag{2.36}$$

where

$$\left(\frac{\partial\mu}{\partial T}\right)_N = -\frac{\left(\frac{\partial N}{\partial T}\right)_{\mu}}{\left(\frac{\partial N}{\partial\mu}\right)_T}. \tag{2.37}$$

Thus, calculating the specific heat C_V requires the evaluation of four derivatives appearing in Eqs (2.36) and (2.37), each containing strong coupling correction

terms coming from $\Omega_{\rm NSR}$ in Eq.(2.23). In this thesis, to avoid this difficulty, we numerically evaluate C_V in the normal state as

$$C_V = \frac{E\left(T+\delta T, \mu\left(T+\delta T\right)\right) - E\left(T-\delta T, \mu\left(T-\delta T\right)\right)}{2\delta T}, \tag{2.38}$$

where $\mu\left(T+\delta T\right)$ and $\mu\left(T-\delta T\right)$ are independently solved from the number equation Eq.(2.28), with $\delta T = 0.01 T_{\rm F}$. At $T_{\rm c}$, we use the right-hand derivative

$$C_V = \frac{-E\left(T_{\rm c}+2\delta T, \mu\left(T_{\rm c}+2\delta T\right)\right) + 4E\left(T_{\rm c}+\delta T, \mu\left(T_{\rm c}+\delta T\right)\right) - 3E\left(T_{\rm c}, \mu\left(T_{\rm c}\right)\right)}{2\delta T}. \tag{2.39}$$

2.2 NSR Theory In The Superfluid State

2.2.1 Nambu Representation

Although the NSR theory explained in the previous section was originally proposed to describe the BCS-BEC crossover behaviour of $T_{\rm c}$, this strong-coupling formalism can be extended to the superfluid phase below $T_{\rm c}$. To explain this extension, it is convenient to write the Hamiltonian given by the sum of Eqs (2.1) and ((2.4)) in the Nambu representation as [20, 21, 88]

$$\begin{aligned} H &= \sum_{\boldsymbol{p}} \Psi_{\boldsymbol{p}}^{\dagger}\left[\xi_{\mathbf{p}}\tau_3 - \Delta\tau_1\right]\Psi_{\boldsymbol{p}} - U\sum_{\boldsymbol{q}} \rho_+\left(\mathbf{q}\right)\rho_-\left(-\mathbf{q}\right) \\ &\equiv H_{\rm MF} + H_{\rm I}', \end{aligned} \tag{2.40}$$

where

$$\Psi_{\boldsymbol{p}} = \begin{bmatrix} c_{\boldsymbol{p},\uparrow} \\ c_{-\boldsymbol{p},\downarrow}^{\dagger} \end{bmatrix}. \tag{2.41}$$

is the two-component Nambu field, and τ_i is the corresponding Pauli matrices acting on particle-hole space. In the "Mean-field BCS term",

$$H_{\rm MF} = \sum_{\boldsymbol{p}} \Psi_{\boldsymbol{p}}^{\dagger}\left[\xi_{\mathbf{p}}\tau_3 - \Delta\tau_1\right]\Psi_{\boldsymbol{p}} \tag{2.42}$$

Δ is the superfluid order parameter, given by [91]

$$\Delta = U\sum_{\boldsymbol{p}'} \langle c_{\boldsymbol{p}',\uparrow}^{\dagger} c_{-\boldsymbol{p}',\downarrow}^{\dagger}\rangle_{\rm MF}. \tag{2.43}$$

Here $\langle\cdots\rangle_{\rm MF}$ is the thermal average taken in terms of $H_{\rm MF}$. In Eq.(2.42) Δ is taken to be real and is chosen to be parallel to the τ_1-component, without loss of generality. The interaction term beyond the mean-field BCS theory,

$$H_{\rm I}' = -U\sum_{\boldsymbol{q}} \rho_+\left(\mathbf{q}\right)\rho_-\left(-\mathbf{q}\right), \tag{2.44}$$

contains the generalised density operator

$$\begin{aligned} \rho_{\pm}\left(\mathbf{q}\right) &= \left[\rho_1\left(\mathbf{q}\right) \pm i\rho_2\left(\mathbf{q}\right)\right]/2, \\ \rho_j\left(\mathbf{q}\right) &= \sum_{\boldsymbol{p}} \Psi_{\boldsymbol{p}+\boldsymbol{q}/2}^{\dagger}\tau_j\Psi_{\boldsymbol{p}-\boldsymbol{q}/2}. \end{aligned} \tag{2.45}$$

Since we are taking the superfluid order parameter Δ to be parallel to the τ_1-component, $\rho_1\left(\mathbf{q}\right)$ and $\rho_2\left(\mathbf{q}\right)$ physically describe amplitude and phase fluctuations of the superfluid order parameter [20, 21].

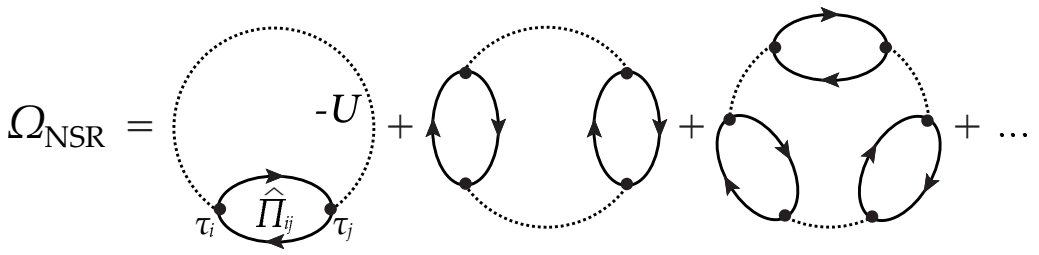

Figure 2.5: NSR corrections $\Omega_{\rm NSR}$ to the thermodynamic potential Ω in the superfluid state below $T_{\rm c}$. $\hat{\Pi}_{ij}$ is the (ij) component of the particle-particle correlation function, in Eq.(2.51).

2.2.2 Strong Coupling Corrections To The Thermodynamic Potential In The Superfluid Phase

Extending the discussion in Sec.2.1 to the superfluid state, we evaluate fluctuation corrections coming from $H_{\rm I}'$ in Eq.(2.44) to the thermodynamic potential Ω. The resulting superfluid thermodynamic potential Ω within the framework of the NSR theory is given by the sum $\Omega = \Omega_{\rm MF} + \Omega_{\rm NSR}$ of the mean-field part $\Omega_{\rm MF}$ and the fluctuation part $\Omega_{\rm NSR}$. Here, the mean-field part has the same form as the thermodynamic potential in the ordinary BCS theory, given by

$$\begin{aligned}\Omega_{\rm MF} &= -T\ln\left[{\rm tr}e^{H_{\rm MF}/T}\right] \\ &= \sum_{\boldsymbol{p}}\left[\xi_{\boldsymbol{p}} - E_{\boldsymbol{p}} + \frac{\Delta^2}{2\varepsilon_{\boldsymbol{p}}} + 2T\ln\left[1 - n_{\rm F}\left(E_{\boldsymbol{p}}\right)\right]\right] - \frac{m\Delta^2}{4\pi a_s},\end{aligned} \tag{2.46}$$

where $E_{\boldsymbol{p}} = \sqrt{\xi_{\boldsymbol{p}}^2 + \Delta^2}$ represents the Bogoliubov single-particle excitations. The fluctuation correction $\Omega_{\rm NSR}$ is diagrammatically described as Fig.2.5, which gives,

$$\Omega_{\rm NSR} = -\frac{T}{2}\sum_{\boldsymbol{q},i\nu_n}{\rm tr}\ln\hat{\Gamma}\left(\boldsymbol{q},i\nu_n\right), \tag{2.47}$$

where

$$\begin{aligned}\hat{\Gamma}\left(\boldsymbol{q},i\nu_n\right) &= -U\left[\mathbf{1} + U\hat{\Pi}\left(\boldsymbol{q},i\nu_n\right)\right]^{-1} \\ &= \begin{pmatrix}\Gamma_{-+}\left(\boldsymbol{q},i\nu_n\right) & \Gamma_{--}\left(\boldsymbol{q},i\nu_n\right) \\ \Gamma_{++}\left(\boldsymbol{q},i\nu_n\right) & \Gamma_{+-}\left(\boldsymbol{q},i\nu_n\right)\end{pmatrix}.\end{aligned} \tag{2.48}$$

is the 2×2 particle-particle scattering matrix in the Nambu formalism, with the 2×2 matrix pair correlation function having the form,

$$\begin{aligned}\hat{\Pi}\left(\boldsymbol{q},i\nu_n\right) &= \begin{pmatrix}\Pi_{-+}\left(\boldsymbol{q},i\nu_n\right) & \Pi_{--}\left(\boldsymbol{q},i\nu_n\right) \\ \Pi_{++}\left(\boldsymbol{q},i\nu_n\right) & \Pi_{+-}\left(\boldsymbol{q},i\nu_n\right)\end{pmatrix}, \\ \Pi_{ij}(\boldsymbol{q},i\nu_n) &= T\sum_{\boldsymbol{p},i\omega_n}{\rm tr}\left[\tau_i\hat{G}_0(\boldsymbol{p}+\boldsymbol{q},i\omega_n+i\nu_n)\tau_j\hat{G}_0(\boldsymbol{p},i\omega_n)\right].\end{aligned} \tag{2.49}$$

In Eq.(2.49) $\hat{G}_0(\boldsymbol{p},i\omega_n)$ is the 2×2 matrix single particle Green's function in the BCS theory, given by [88]

$$\hat{G}_0(\boldsymbol{p},i\omega_n) = \frac{1}{i\omega_n - \xi_{\boldsymbol{p}}\tau_3 + \Delta\tau_1}. \tag{2.50}$$

Carrying out the Matsubara frequency summation over in Eq.(2.49) we have

$$\begin{aligned}
\Pi_{-+}(\boldsymbol{q}, i\nu_n) &= -\frac{1}{4}\sum_{\boldsymbol{p},s=\pm 1}\frac{\tanh\dfrac{E_+}{2T}+s\tanh\dfrac{E_-}{2T}}{(E_++sE_-)^2+\nu_n^2} \\
&\times \left[(E_++sE_-)\left(1+s\frac{\xi_+\xi_-}{E_+E_-}\right)+i\nu_n\left(\frac{\xi_+}{E_+}+s\frac{\xi_+}{E_+}\right)\right], \\
\Pi_{+-}(\boldsymbol{q}, i\nu_n) &= \Pi^{-+}(\boldsymbol{q}, -i\nu_n), \\
\Pi_{--}(\boldsymbol{q}, i\nu_n) &= \frac{1}{4}\sum_{\boldsymbol{p},s=\pm 1}\frac{\Delta^2}{E_+E_-}\frac{s(E_++sE_-)}{(E_++sE_-)^2+\nu_n^2}\left[\tanh\frac{E_+}{2T}+s\tanh\frac{E_-}{2T}\right], \\
\Pi_{++}(\boldsymbol{q}, i\nu_n) &= \Pi^{--}(\boldsymbol{q}, i\nu_n),
\end{aligned} \tag{2.51}$$

where $\xi_\pm = \xi_{\boldsymbol{p}\pm\boldsymbol{p}/2}$, and $E_\pm = E_{\boldsymbol{p}\pm\boldsymbol{p}/2}$.

We note that when $\Delta \to 0$, Eq.(2.49) becomes

$$\hat{\Pi}(\boldsymbol{q}, i\nu_n) = \begin{pmatrix} -\Pi(\boldsymbol{q}, i\nu_n) & 0 \\ 0 & -\Pi(\boldsymbol{q}, -i\nu_n) \end{pmatrix}. \tag{2.52}$$

In this limit, $\Omega_{\rm NSR}$ in Eq.(2.47) is reduced to the correction term in Eq.(2.23) above $T_{\rm c}$.

We also briefly note that the NSR correction term $\Omega_{\rm NSR}$ in the superfluid state looks to be described by different diagrams from those in the normal state (see Figs 2.2 and 2.5). This is, however, simply due to the fact that we are using the Nambu representation in the superfluid case. Indeed, when one rewrites the diagrams in Fig.2.5 by using the components of the Nambu Green's function $\hat{G}_0(\boldsymbol{p}, i\omega_n)$ in Eq.(2.50), the resulting diagrams are found to have the same double ring structure shown in Fig.2.2.

In the above formalism, the superfluid order parameter Δ is determined from the Thouless criterion [20, 21, 90],

$$\det\hat{\Gamma}(\boldsymbol{q}=\boldsymbol{0}, i\nu_n=0)^{-1} = 0, \tag{2.53}$$

Physically, Eq.(2.53) is equivalent to the required condition for the existence of the Gapless Goldstone mode associated with the spontaneously broken $U(1)$ gauge symmetry. In the present NSR formalism, the Thouless criterion in Eq.(2.53) gives the ordinary BCS gap equation

$$1 = -\frac{4\pi a_s}{m}\sum_{\boldsymbol{p}}\left[\frac{1}{2E_{\boldsymbol{p}}}\tanh\frac{E_{\boldsymbol{p}}}{2T}-\frac{1}{2\varepsilon_{\boldsymbol{p}}}\right]. \tag{2.54}$$

We note that Eq.(2.54) is consistent with the definition of the superfluid order parameter in Eq.(2.43), because the mean-field average ($\langle\cdots\rangle_{\rm MF}$) also gives the gap-equation. We also note that Eq.(2.54) is reduced to the $T_{\rm c}$-equation (2.27) when $\Delta = 0$.

As in the normal state, we actually solve the gap equation (2.54), together with the number equation, to self-consistently determine the superfluid order parameter

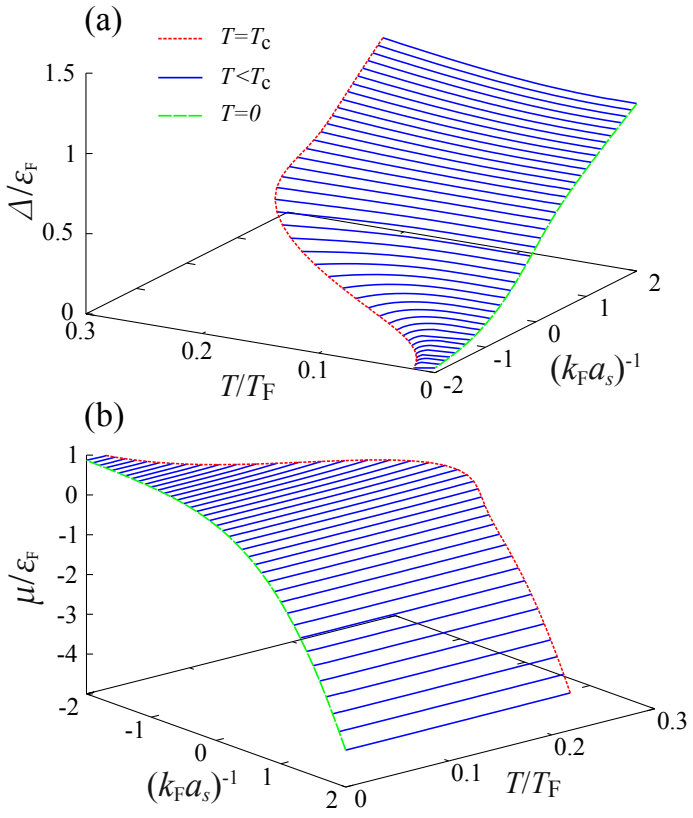

Figure 2.6: Self-consistent solution for the coupled gap equation (2.54) with the number equation (2.28). (a) Superfluid order parameter Δ. (b) Fermi chemical potential μ.

Δ and $\mu(T \leq T_c)$. The latter equation is obtained from the identity in Eq.(2.28), when, in the superfluid case,

$$N_0 = -\left(\frac{\partial \Omega_0}{\partial \mu}\right)_T = \sum_{\boldsymbol{p}} \left[1 - \frac{\xi_{\boldsymbol{p}}}{E_{\boldsymbol{p}}} \tanh \frac{E_{\boldsymbol{p}}}{2T}\right], \tag{2.55}$$

is now the mean-field BCS part, and

$$\begin{aligned} N_{\rm NSR} &= -\left(\frac{\partial \Omega_{\rm NSR}}{\partial \mu}\right)_T = -\left(\frac{\partial \Omega_{\rm NSR}}{\partial \mu}\right)_{\Delta,T} - \left(\frac{\partial \Omega_{\rm NSR}}{\partial \Delta}\right)_{T,\mu}\left(\frac{\partial \Delta}{\partial \mu}\right)_T \\ &= \frac{T}{2}\sum_{\boldsymbol{q},i\nu_n} \mathrm{tr}\left[\hat{\Gamma}(\boldsymbol{q}, i\nu_n)\frac{\partial \hat{\Pi}(\boldsymbol{q}, i\nu_n)}{\partial \mu}\right] \\ &+ \frac{T}{2}\sum_{\boldsymbol{q},i\nu_n} \mathrm{tr}\left[\hat{\Gamma}(\boldsymbol{q}, i\nu_n)\frac{\partial \hat{\Pi}(\boldsymbol{q}, i\nu_n)}{\partial \Delta}\right]\left(\frac{\partial \Delta}{\partial \mu}\right)_T \end{aligned} \tag{2.56}$$

Here, the factor $(\partial\Delta/\partial\mu)_T$ is given by

$$\left(\frac{\partial \Delta}{\partial \mu}\right)_T = \frac{\displaystyle\sum_{\boldsymbol{p}} \frac{\xi_{\boldsymbol{p}}}{E_{\boldsymbol{p}}^2}\left[\frac{1}{2T}\mathrm{sech}^2\left(\frac{E_{\boldsymbol{p}}}{2T}\right) - \frac{1}{E_{\boldsymbol{p}}}\tanh\left(\frac{E_{\boldsymbol{p}}}{2T}\right)\right]}{\displaystyle\sum_{\boldsymbol{p}} \frac{\Delta}{E_{\boldsymbol{p}}^2}\left[\frac{1}{2T}\mathrm{sech}^2\left(\frac{E_{\boldsymbol{p}}}{2T}\right) - \frac{1}{E_{\boldsymbol{p}}}\tanh\left(\frac{E_{\boldsymbol{p}}}{2T}\right)\right]}. \tag{2.57}$$

For the derivation of Eq.(2.57) see appendix B.

Figure 2.6 shows the calculated superfluid order parameter Δ, as well as the Fermi chemical potential μ in the BCS-BEC crossover region below T_c. We will use this numerical data in calculating the specific heat C_V and internal energy in the superfluid phase in Chaps. 3 and 4. Regarding this, we note that Δ in Fig.2.6 (a) remains finite even at T_c, which is, however, an artefact of the present strong-coupling theory. Such an unphysical behaviour just below T_c is also known in other diagrammatic theories, such as a non-self-consistent T-matrix approximation (TMA) [22] and self-consistent T-matrix approximation (SCTMA) [29], but so far this problem has not been solved yet. In this thesis we also leave this as a future problem, to employ the present superfluid NSR theory up to T_c, keeping in mind that this problem may affect our results just below T_c.

2.2.3 Internal Energy And Specific Heat Below T_c

The Legendre transformation in Eq.(2.32) is also valid for the present superfluid case. The resulting E_0 and $E_{\rm NSR}$ are given by, respectively

$$E_0 = \sum_{\boldsymbol{p}} \left[E_{\boldsymbol{p}} n_{\rm F}(E_{\boldsymbol{p}}) + \xi_{\mathbf{p}} - E_{\boldsymbol{p}} - \frac{\Delta^2}{2\varepsilon_{\boldsymbol{p}}} \right] + \frac{m\Delta^2}{4\pi a_s} + \mu N_{\rm MF}, \tag{2.58}$$

and

$$\begin{aligned} E_{\rm NSR} &= \frac{T}{2} \sum_{\boldsymbol{q}, i\nu_n} \left[T{\rm tr} \left[\hat{\Gamma}(\boldsymbol{q}, i\nu_n) \frac{\partial \hat{\Pi}(\boldsymbol{q}, i\nu_n)}{\partial T} \right] + \mu {\rm tr} \left[\hat{\Gamma}(\boldsymbol{q}, i\nu_n) \frac{\partial \hat{\Pi}(\boldsymbol{q}, i\nu_n)}{\partial \mu} \right] \right] \\ &+ \frac{T^2}{2} \sum_{\boldsymbol{q}, i\nu_n} {\rm tr} \left[\hat{\Gamma}(\boldsymbol{q}, i\nu_n) \frac{\partial \hat{\Pi}(\boldsymbol{q}, i\nu_n)}{\partial \Delta} \right] \left(\frac{\partial \Delta}{\partial T} \right)_{\mu}, \end{aligned} \tag{2.59}$$

with

$$\left(\frac{\partial \Delta}{\partial T} \right)_{\mu} = \frac{\displaystyle\sum_{\boldsymbol{p}} \frac{1}{2T^2} {\rm sech}^2 \left(\frac{E_{\boldsymbol{p}}}{2T} \right)}{\displaystyle\sum_{\boldsymbol{p}} \frac{\Delta}{E_{\boldsymbol{p}}^2} \left[\frac{1}{2T} {\rm sech}^2 \left(\frac{E_{\boldsymbol{p}}}{2T} \right) - \frac{1}{E_{\boldsymbol{p}}} \tanh \left(\frac{E_{\boldsymbol{p}}}{2T} \right) \right]}. \tag{2.60}$$

We explain the derivation of Eq.(2.60) in appendix B. We briefly note that E_0 in Eq.(2.58) is just the internal energy in the mean-field BCS theory.

The specific heat at constant volume C_V is numerically calculated from the internal energy as

$$C_V = \frac{E(T+\delta T, \mu(T+\delta T), \Delta(T+\delta T)) - E(T-\delta T, \mu(T-\delta T), \Delta(T-\delta T))}{2\delta T}, \tag{2.61}$$

where we set $\delta T = 0.005 T_{\rm F}$.

2.3 Superfluid NSR Theory With A Non-Vanishing Effective Range $r_{\rm eff}$ (Neutron Star Case)

As mentioned previously, although the low density crust regime of a neutron star interior is similar to the unitary regime of a superfluid Fermi gas far below T_c,

we still need to theoretically make up for the different magnitude of the effective range $r_{\rm eff}$ between the two systems. In this section, we explain how to incorporate the non-vanishing effective range into the NSR theory below $T_{\rm c}$.

2.3.1 Effective Range Theory

To deal with the non-vanishing effective range $r_{\rm eff} = 2.7$ fm [67] in the neutron star case, we start from the general interaction Hamiltonian in Eq.(2.2), instead of the contact-type interaction in Eq.(2.3). (Note that $r_{\rm eff} = 0$ in the case of Eq.(2.3)).

We expand the interaction potential $U(\boldsymbol{p}-\boldsymbol{p}')$ into partial-wave components [68], as

$$U(\boldsymbol{p}-\boldsymbol{p}') = U_s(\boldsymbol{p},\boldsymbol{p}') + U_p(\boldsymbol{p},\boldsymbol{p}') + U_d(\boldsymbol{p},\boldsymbol{p}') + \cdots, \tag{2.62}$$

where s, p and d represent the s-wave, p-wave and d-wave components, respectively.

Then, since only the s-wave channel is non-vanishing in the low-momentum limit, we have $U(\boldsymbol{0}) = U_s(\boldsymbol{0},\boldsymbol{0})$. Here, we assume that the s-wave component $U_s(\boldsymbol{p},\boldsymbol{p}')$ gives the dominant contribution in the low-density crust regime of a neutron star. To include the effective range $r_{\rm eff}$ we consider the following separable interaction [15, 34]

$$U(\boldsymbol{p}-\boldsymbol{p}') \simeq U_s(\boldsymbol{p},\boldsymbol{p}') = U(\boldsymbol{0})\gamma_{\boldsymbol{p}}\gamma_{\boldsymbol{p}'}. \tag{2.63}$$

The detailed expression for the basis function $\gamma_{\boldsymbol{p}}$ is specified soon later.

For the separable s-wave interaction $U_s(\boldsymbol{p},\boldsymbol{p}')$, we consider the two-body scattering T-matrix $\Gamma_{\rm 2b}(\boldsymbol{p},\boldsymbol{p}',\omega_+)$ which obeys the equation [34],

$$\Gamma_{\rm 2b}(\boldsymbol{p},\boldsymbol{p}';\omega_+) = -U_s(\boldsymbol{p},\boldsymbol{p}') - \sum_{\boldsymbol{k}} U_s(\boldsymbol{p},\boldsymbol{k})\frac{1}{\omega_+ - 2\varepsilon_{\boldsymbol{k}}}\Gamma_{\rm 2b}(\boldsymbol{k},\boldsymbol{p}';\omega_+), \tag{2.64}$$

where $\omega_+ = \omega + i\delta$, with δ being an infinitesimally small positive number.

Taking $\Gamma(\boldsymbol{p},\boldsymbol{p}';\omega_+) = \gamma_{\boldsymbol{p}}\Lambda(\omega_+)\gamma_{\boldsymbol{p}'}$, one finds that $\Lambda(\omega_+)$ obeys,

$$\frac{1}{\Lambda(\omega_+)} = -\frac{1}{U(\boldsymbol{0})} - \sum_{\boldsymbol{k}}\frac{\gamma_{\boldsymbol{k}}^2}{\omega_+ - 2\varepsilon_{\boldsymbol{k}}}. \tag{2.65}$$

The scattering T-matrix $\Gamma_{\rm 2b}(\boldsymbol{p},\boldsymbol{p}';\omega_+)$ in Eq.(2.64) is related to the so-called s-wave phase shift $\delta_s(\boldsymbol{p})$ as [68],

$$\frac{1}{p\cot\delta_s(\boldsymbol{p}) - ip} = -\frac{m}{4\pi}\Gamma(\boldsymbol{p},\boldsymbol{p};2\varepsilon_{\boldsymbol{p}} + i\delta), \tag{2.66}$$

where the phase shift $\delta_s(\boldsymbol{p})$ can be expanded as [68, 69]

$$p\cot\delta_s(\boldsymbol{p}) = -\frac{1}{a_s} + \frac{1}{2}r_{\rm eff}p^2 - Pr_{\rm eff}^3p^4 + \cdots. \tag{2.67}$$

For this expression, a_s is the s-wave scattering length, $r_{\rm eff}$ is the effective range, and P is the s-wave shape parameter. Setting $\boldsymbol{p}\to\boldsymbol{0}$ in Eqs (2.66) and (2.67), and

noting that $\Gamma(\mathbf{0},\mathbf{0};0_+) = \Lambda(0_+)$, one finds,

$$\frac{4\pi a_s}{m} = -\frac{U(\mathbf{0})}{1 - U(\mathbf{0})\sum_{\boldsymbol{p}} \dfrac{\gamma_{\boldsymbol{p}}^2}{2\varepsilon_{\boldsymbol{p}}}}, \tag{2.68}$$

which relates the s-wave scattering length a_s to $U(\mathbf{0})$.

Substituting Eq. (2.68) and Eq.(2.65) into Eq. (2.66), we obtain

$$\frac{1}{p\cot\delta_s(\boldsymbol{p}) - ip} = \frac{\gamma_{\boldsymbol{p}}^2}{-\dfrac{1}{a_s} - \dfrac{4\pi}{m}\displaystyle\sum_{\boldsymbol{p}'} \gamma_{\boldsymbol{p}'}^2 \left[\frac{1}{2\varepsilon_{\boldsymbol{p}'} - (2\varepsilon_{\boldsymbol{p}} + i\delta)} - \frac{1}{2\varepsilon_{\boldsymbol{p}'}}\right]}. \tag{2.69}$$

In the effective range theory, the first two terms on the right side of Eq.(2.67) are only retained [34, 68]. This situation can be achieved when we choose the basis function $\gamma_{\boldsymbol{p}}$ in Eq. (2.69) as

$$\gamma_{\boldsymbol{p}} = \frac{1}{\sqrt{1 + \left(\dfrac{p}{p_{\rm c}}\right)^2}}, \tag{2.70}$$

where $p_{\rm c}$ is a cutoff momentum. Substituting Eq.(2.70) into Eq.(2.69), we find

$$p_{\rm c} = \frac{1}{r_{\rm eff}}\left[1 + \sqrt{1 - \frac{2r_{\rm eff}}{a_s}}\right]. \tag{2.71}$$

The outline of this derivation is explained in appendix C.

In this effective range theory we also find from Eq.(2.68),

$$U(\mathbf{0}) = \frac{2\pi}{m}\left(\frac{1}{r_{\rm eff}}\left[1 + \sqrt{1 - \frac{2r_{\rm eff}}{a_s}}\right] - \frac{1}{2a_s}\right)^{-1}. \tag{2.72}$$

Equation (2.72) shows how to obtain the value of $U(\mathbf{0})$ for a given parameter set $(a_s, r_{\rm eff})$. To emphasise this, we write $U(\mathbf{0}) \equiv U(a_s, r_{\rm eff})$ in what follows.

In the case of an ultracold Fermi gas, the effective range $r_{\rm eff}$ is negligibly small, so that $p_{\rm c} \to \infty$, giving $\gamma_{\boldsymbol{p}} = 1$ in Eq. (2.63). This recovers the contact-type s-wave interaction employed in Secs 2.1 and 2.2. In the neutron star case, on the other hand, the scattering length and effective range equal $a_s = -18.5$ fm and 2.7 fm [66], respectively, which gives

$$p_{\rm c} = 0.79\ {\rm fm}^{-1}. \tag{2.73}$$

We use this cutoff momentum in considering the neutron star equation of state in Chap. 4.

We now incorporate the above-mentioned effective range theory into the superfluid BCS Hamiltonian in Eq.(2.40). For this procedure, a crucial difference between the cases of the contact-type interaction ($r_{\rm eff} = 0$) and Eq.(2.63) ($r_{\rm eff} \neq 0$) is

that the Hartree energy in the former case is absent because of the infinitesimally small coupling constant $U \to +0$ (see Eq.(2.25) with $p_c \to \infty$).

In contrast, the bare coupling constant $U(\mathbf{0}) = U(a_s, r_{\rm eff})$ in Eq.(2.72) does not vanish when $r_{\rm eff} \neq 0$. In this case, we need to retain the Hartree term, in the mean-field Hartree-Foch approach [31]. In this approximation $H_{\rm I}$ in Eq.(2.2) becomes

$$\begin{aligned} H_{\rm I}^{\rm HF} &= -\frac{1}{2}U(\mathbf{0})N_{\rm MF}\sum_{\boldsymbol{p},\sigma}\xi_{\boldsymbol{p}}c^{\dagger}_{\boldsymbol{p},\sigma}c_{\boldsymbol{p},\sigma} + \frac{1}{4}U(\mathbf{0})N_{\rm MF}^2 \\ &= -\frac{1}{2}U(a_s, r_{\rm eff})N_{\rm MF}\sum_{\boldsymbol{p},\sigma}\xi_{\boldsymbol{p}}c^{\dagger}_{\boldsymbol{p},\sigma}c_{\boldsymbol{p},\sigma} + \frac{1}{4}U(a_s, r_{\rm eff})N_{\rm MF}^2, \end{aligned} \tag{2.74}$$

when

$$N_{\rm MF} = \sum_{\boldsymbol{p},\sigma}\langle c^{\dagger}_{\boldsymbol{p},\sigma}c_{\boldsymbol{p},\sigma}\rangle_{\rm MF} \tag{2.75}$$

is the total number of Fermi particles in the mean-field approximation.

As a result, $H_{\rm MF}$ and $H'_{\rm I}$ in Eq.(2.40) are modified to be, respectively

$$H_{\rm MF} = \sum_{\boldsymbol{p}}\hat{\Psi}^{\dagger}_{\boldsymbol{p}}\left[\tilde{\xi}_{\mathbf{p}}\tau_3 - \Delta_{\boldsymbol{p}}\tau_1\right]\hat{\Psi}_{\boldsymbol{p}} + \sum_{\boldsymbol{p}}\left[\tilde{\xi}_{\mathbf{p}} + \frac{\Delta_{\boldsymbol{p}}^2}{U(a_s, r_{\rm eff})}\right] + \frac{1}{4}U(a_s, r_{\rm eff})N_{\rm MF}^2, \tag{2.76}$$

$$H'_{\rm I} = -U(a_s, r_{\rm eff})\sum_{\boldsymbol{q}}\tilde{\rho}_{+}(\mathbf{q})\,\tilde{\rho}_{-}(-\mathbf{q}). \tag{2.77}$$

In Eq.(2.76), $\tilde{\xi}_{\boldsymbol{p}} = \xi_{\boldsymbol{p}} - U(a_s, r_{\rm eff})N_{\rm MF}/2$ involves the so-called Hartree shift $-U(a_s, r_{\rm eff})N_{\rm MF}/2$, and

$$N_{\rm MF} = \sum_{\boldsymbol{p},\sigma}\langle c^{\dagger}_{\boldsymbol{p},\sigma}c_{\boldsymbol{p},\sigma}\rangle_{\rm MF} = \sum_{\boldsymbol{p}}\left[1 - \frac{\tilde{\xi}_{\boldsymbol{p}}}{\tilde{E}_{\boldsymbol{p}}}\tanh\frac{\tilde{E}_{\boldsymbol{p}}}{2T}\right], \tag{2.78}$$

with $\tilde{E}_{\boldsymbol{p}} = \sqrt{\tilde{\xi}_{\boldsymbol{p}}^2 + \Delta_{\boldsymbol{p}}^2}$. The superfluid order parameter $\Delta_{\boldsymbol{p}}$ now depends on the momentum $\boldsymbol{p}$ as

$$\Delta_{\boldsymbol{p}} = \gamma_{\boldsymbol{p}}\Delta, \tag{2.79}$$

when

$$\begin{aligned} \Delta &= U(a_s, r_{\rm eff})\sum_{\boldsymbol{p}}\gamma_{\boldsymbol{p}}\langle c^{\dagger}_{\boldsymbol{p},\uparrow}c^{\dagger}_{-\boldsymbol{p},\downarrow}\rangle_{\rm MF} \\ &= U(a_s, r_{\rm eff})\sum_{\boldsymbol{p}}\gamma_{\boldsymbol{p}}\frac{\Delta_{\boldsymbol{p}}}{2\tilde{E}_{\boldsymbol{p}}}\tanh\frac{\tilde{E}_{\boldsymbol{p}}}{2T}. \end{aligned} \tag{2.80}$$

Substituting Eq.(2.79) into Eq.(2.80), we obtain the gap equation

$$1 = U(a_s, r_{\rm eff})\sum_{\boldsymbol{p}}\frac{\gamma_{\boldsymbol{p}}^2}{2\tilde{E}_{\boldsymbol{p}}}\tanh\frac{\tilde{E}_{\boldsymbol{p}}}{2T}. \tag{2.81}$$

The interaction term in Eq.(2.77) is similar to Eq.(2.44), but the generalised density operator $\tilde{\rho}_{\pm}(\mathbf{q})$ now involves the basis function as

$$\tilde{\rho}_{\pm}(\mathbf{q}) = \sum_{\boldsymbol{p}}\gamma_{\boldsymbol{p}}\hat{\Psi}^{\dagger}_{\boldsymbol{p}+\boldsymbol{q}/2}\tau_{\pm}\hat{\Psi}_{\boldsymbol{p}-\boldsymbol{q}/2}. \tag{2.82}$$

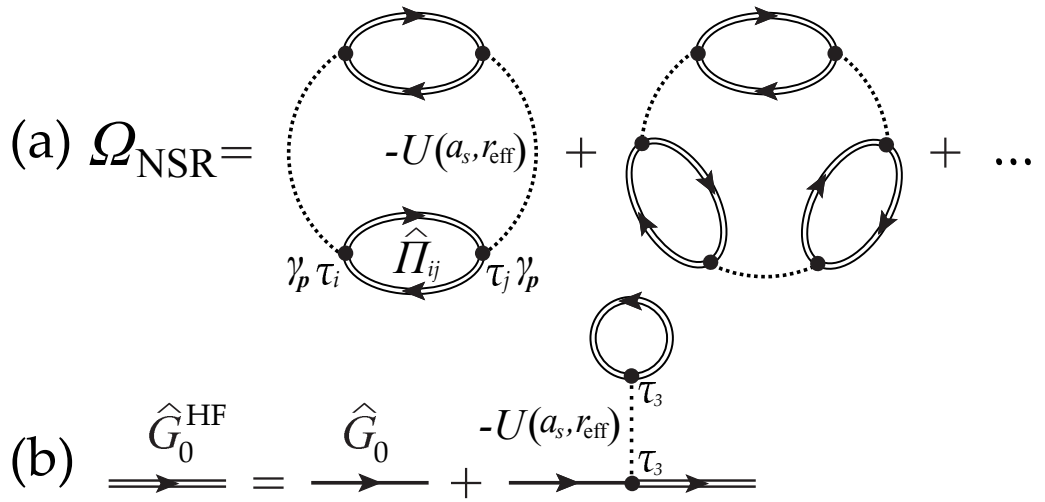

Figure 2.7: (a) NSR fluctuation correction $\Omega_{\rm NSR}$ to the thermodynamic potential Ω in the presence of a non-vanishing effective range $r_{\rm eff}$. $\hat{\Pi}_{ij}$ is the (ij) component of the particle-particle correlation function in Eq.(2.86). $-U(a_s, r_{\rm eff}) < 0$ is the bare attractive interaction in Eq.(2.68). The double-solid line represents the single-particle Green's function involving the Hartree shift, which obeys the Dyson equation is shown in panel (b). Note that the correction term corresponding to the first term in Fig.2.5 has been taken into account in $\Omega_{\rm MF}$, in Eq.(2.84), in the present case, so that $\Omega_{\rm NSR}$ in panel (a) starts from the second order in terms of the bare interaction $-U(a_s, r_{\rm eff})$.

2.3.2 Superfluid NSR Theory In The Presence Of Non-Vanishing Effective Range

Starting from $H = H_{\rm MF} + H_{\rm I}'$ (when $H_{\rm MF}$ and $H_{\rm I}'$ are, respectively, given in Eqs. (2.76) and (2.77)), we evaluate strong-coupling corrections $\Omega_{\rm NSR}$ to the thermodynamic potential Ω within the framework of NSR theory. This procedure is essentially the same as in the absence of the effective range ($r_{\rm eff} = 0$) explained in Sec.2.2, except for the presence of (1) the basis function $\gamma_{\boldsymbol{p}}$ in Eq.(2.70), and (2) the Hartree shift $-U(a_s, r_{\rm eff})N_{\rm MF}/2$ in the single-particle dispersion $\tilde{E}_{\boldsymbol{p}}$. The former affects the vertex part of the pair correlation function Π_{ij} in evaluating $\Omega_{\rm NSR}$, as diagonally shown in Fig.2.7 (a). (Compare this figure with Fig.2.5 ($r_{\rm eff} = 0$)) The latter is simply incorporated into the NSR theory by replacing the single-particle Green's function $\hat{G}_0$ in Eq.(2.50) with

$$\hat{G}_0^{\rm HF}(\boldsymbol{p}, i\omega_n) \;=\; \frac{1}{i\omega_n - \tilde{\xi}_{\boldsymbol{p}}\tau_3 + \gamma_{\boldsymbol{p}}\Delta\tau_1}. \tag{2.83}$$

This modification is diagrammatically described by the Dyson equation in Fig 2.7(b).

The resulting NSR thermodynamic potential $\Omega = \Omega_{\rm MF} + \Omega_{\rm NSR}$ is given by the sum

of the mean-field term

$$\begin{aligned}\Omega_{\rm MF} &= -T\ln\left[{\rm tr}e^{-H_{\rm MF}/T}\right] \\ &= -2T\sum_{\boldsymbol{p}}\left[\ln\left[1+e^{-\tilde{E}_{\boldsymbol{p}}/T}\right]+\tilde{\xi}_{\mathbf{p}}-\tilde{E}_{\boldsymbol{p}}\right] \\ &+ \frac{\Delta^2}{U(a_s,r_{\rm eff})}+\frac{1}{4}U(a_s,r_{\rm eff})N_{\rm MF}^2,\end{aligned} \tag{2.84}$$

and the fluctuation correction

$$\Omega_{\rm NSR}=\frac{T}{2}\sum_{\boldsymbol{q},i\nu_n}{\rm tr}\Big[\ln\left[1+U(a_s,r_{\rm eff})\hat{\Pi}(\boldsymbol{q},i\nu_n)\right]-U(a_s,r_{\rm eff})\hat{\Pi}(\boldsymbol{q},i\nu_n)\Big], \tag{2.85}$$

where the pair-correlation involving the basis function $\gamma_{\boldsymbol{p}}$ is given by

$$\Pi_{ij}(\boldsymbol{q},i\nu_n)=T\sum_{\boldsymbol{p},i\omega_n}\gamma_{\boldsymbol{p}}^2{\rm tr}\left[\tau_i\hat{G}_0^{\rm HF}(\boldsymbol{p}+\boldsymbol{q},i\omega_n+i\nu_n)\tau_j\hat{G}_0^{\rm HF}(\boldsymbol{p},i\omega_n)\right]. \tag{2.86}$$

We briefly note that $\Omega_{\rm MF}$ is the thermodynamic potential in the mean-field level, so that the mean-field particle number $N_{\rm MF}$ in Eq.(2.77), as well as the mean-field order parameter Δ in Eq.(2.81), respectively, satisfies the saddle point conditions,

$$\begin{aligned}\left(\frac{\partial\Omega_{\rm MF}}{\partial N_{\rm MF}}\right)_{T,\mu,\Delta}&=0,\\ \left(\frac{\partial\Omega_{\rm MF}}{\partial\Delta}\right)_{T,\mu,N_{\rm MF}}&=0.\end{aligned} \tag{2.87}$$

Using the NSR thermodynamic potential $\Omega=\Omega_{\rm MF}+\Omega_{\rm NSR}$, we derive the number equation,

$$\begin{aligned}N &= -\left(\frac{\partial\Omega}{\partial\mu}\right)_T \\ &= N_{\rm MF}+N_{\rm NSR},\end{aligned} \tag{2.88}$$

where $N_{\rm MF}$ is given in Eq.(2.78), and

$$\begin{aligned}N_{\rm NSR} &= -\left(\frac{\partial\Omega_{\rm NSR}}{\partial\mu}\right)_T \\ &= -\left(\frac{\partial\mu^*}{\partial\mu}\right)_T\left(\frac{\partial\Omega_{\rm NSR}}{\partial\mu^*}\right)_T,\end{aligned} \tag{2.89}$$

Here we have used the fact that $\Omega_{\rm NSR}$ in Eq.(2.85), only depends on μ through the effective chemical potential $\mu^*=\mu+U(a_s,r_{\rm eff})N_{\rm MF}/2$.

In Eq.(2.89), $(\partial\Omega_{\rm NSR}/\partial\mu^*)_T$ can be evaluated in the same way as Eq.(2.56). On the other hand,

$$\begin{aligned}\left(\frac{\partial\mu^*}{\partial\mu}\right)_T &= 1+\frac{U(a_s,r_{\rm eff})}{2}\left(\frac{\partial N_{\rm MF}}{\partial\mu}\right)_T \\ &= 1+\frac{U(a_s,r_{\rm eff})}{2}\left(\frac{\partial N_{\rm MF}}{\partial\mu^*}\right)\left(\frac{\partial\mu^*}{\partial\mu}\right)_T,\end{aligned} \tag{2.90}$$

which gives

$$\left(\frac{\partial\mu^*}{\partial\mu}\right)_T = \frac{1}{1-\frac{1}{2}U(a_s,r_{\rm eff})\left(\frac{\partial N_{\rm MF}}{\partial\mu^*}\right)_T}. \tag{2.91}$$

Equation (2.91) is just the Stoner factor appearing in the density response function [92].

2.3.3 Internal Energy Far Below $T_{\rm c}$

In Chap.4, we discuss the internal energy E (equation of state) and effects of the non-vanishing effective range within the framework explained in this section. In the present case, E_0 and $E_{\rm NSR}$ in Eq.(2.32) have the forms, respectively,

$$E_{\rm MF} = \sum_{\boldsymbol{p}}\left[\tilde{E}_{\boldsymbol{p}} n_{\rm F}(\tilde{E}_{\boldsymbol{p}}) + \tilde{\xi}_{\mathbf{p}} - \tilde{E}_{\boldsymbol{p}}\right] + \frac{\Delta^2}{U(a_s,r_{\rm eff})} + \frac{1}{4}U(a_s,r_{\rm eff})N_{\rm MF}^2 + \mu N_{\rm MF}, \tag{2.92}$$

and

$$E_{\rm NSR} = \Omega_{\rm NSR} - T\left(\frac{\partial\Omega_{\rm NSR}}{\partial T}\right)_\mu + \mu N_{\rm NSR}. \tag{2.93}$$

In Chap.4, using Eq.(2.92) and Eq.(2.93), we examine the internal energy in the low-density crust regime of a neutron star, by setting $a_s = -18.5$ fm and $r_{\rm eff} = 2.7$ fm. In this thesis take $T/T_{\rm F} = 0.02$ to consider the region near the ground state. Although we can't set $T/T_{\rm F} = 0$ because of computational problems; however we have numerically confirmed that our results do not change within the temperature range $T/T_{\rm F} = [0.005, 0.06]$, so that thermal effects are considered to be almost absent at this temperature. In considering the neutron star case, we measure the EOS in units of MeV, by using the neutron mass $m = 939$ MeV$/c^2$ (where c the speed of light).

Chapter 3

Specific Heat In The BCS-BEC Crossover Region Of An Ultracold Fermi Gas

In this chapter we theoretically investigate strong-coupling properties of an ultracold Fermi gas in the BCS-BEC crossover region. Within the framework of the NSR theory explained in Secs.2.1 and 2.2, we examine the specific heat at constant volume C_V. In the normal state, using the advantage of this quantity that it remains finite in the whole BCS-BEC crossover region, we identify the region where pairing fluctuations dominate over system properties, as well as the region where the system is well described by a gas of tightly bound molecules, in the phase diagram of an ultracold Fermi gas with respect to the interaction strength and temperature. In the superfluid phase below T_c we show that C_V is simply monotonically increasing with increasing temperature.

In Sec.3.1 we first show the calculated C_V at T_c. In Sec.3.2, we examine the temperature dependence of C_V above T_c, to construct the phase diagram of this system. We proceed to the superfluid state in Sec.3.3, which is followed by the comparison of our result with the recent experiment on an ^{6}Li unitary Fermi gas in Sec.3.5.

3.1 Specific Heat At T_c

Figure 3.1 shows the calculated specific heat at constant volume C_V in the BCS-BEC crossover regime of an ultracold Fermi gas at T_c. (Note that we approach T_c from the normal state.) In the weak coupling regime ($(k_F a_s)^{-1} \lesssim -1$), the calculated $C_V\,(T = T_c)$ is found to be well-described by the specific heat C_V^F of a free Fermi gas, given by [89]

$$C_V^F(T \ll T_F) = \frac{\pi^2}{2}\left(\frac{T}{T_F}\right)N. \tag{3.1}$$

On the other hand, our result in the strong-coupling BEC regime ($(k_F a_s)^{-1} \gtrsim 1$) approaches the specific heat C_V^B of an ideal Bose gas of $N/2$ bosons with molecular mass $M = 2m$, at the Bose-Einstein transition temperature $T_{BEC} = 0.218T_F$ (see Eq.(2.31)), given by [15, 16, 28, 58]

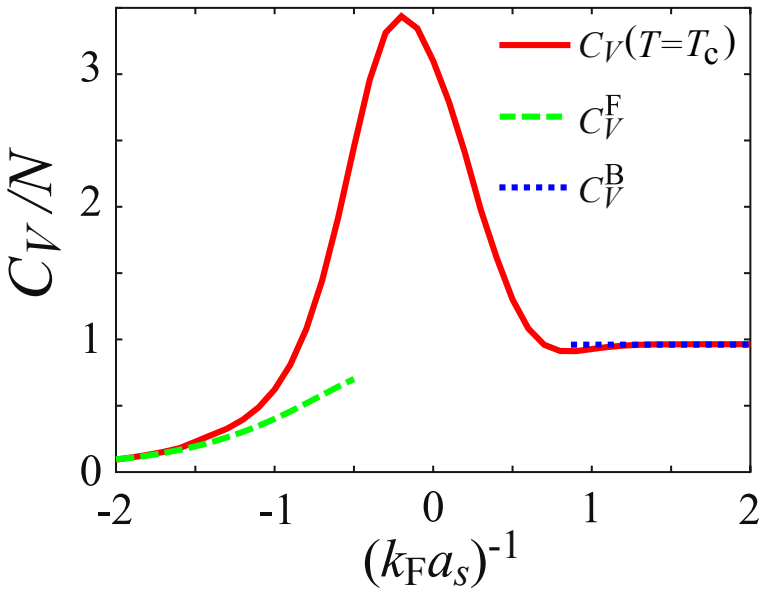

Figure 3.1: Calculated specific heat at constant volume C_V at T_c in the BCS-BEC crossover regime of an ultracold Fermi gas. C_V^F and $C_V^B \simeq 0.96N$ are the specific heat of an ideal Fermi gas at $T = T_c$, and ideal Bose gas at the BEC transition temperature, respectively.

$$C_V^B(T = T_{BEC}) = \frac{15}{4} N_B \times \frac{\zeta(5/2)}{\zeta(3/2)} = 0.963N, \tag{3.2}$$

where $\zeta(3/2) = 2.612$ and $\zeta(5/2) = 1.341$ are Riemann's zeta functions.

This agreement ($C_V \simeq C_V^B(T = T_{BEC})$) is consistent with the BCS-BEC crossover behaviours of T_c and $\mu(T_c)$ in Fig.2.3, where one sees $T_c \simeq T_{BEC}$ and $\mu \simeq E_{bind}/2$ (where $E_{bind} = 1/ma_s^2$ is the molecular binding energy) in the BEC regime, indicating that the system is very close to an ideal Bose gas.

However, while T_c and $\mu(T_c)$ almost monotonically changes from the weak-coupling result to the strong-coupling result (except for a slight hump structure in the case of T_c around $(k_F a_s)^{-1} = 0$ (see Fig.2.3 (a))), we find in Fig.3.1 that $C_V(T = T_c)$ experiences a large enhancement as one passes through the BCS-BEC crossover region. Regarding this, we point out that this behaviour is consistent with the argument in Sec.1.3, that strong pairing fluctuations in the crossover regime near T_c is expected to enhance C_V due to the suppression of the entropy S, through the relation in Eq.(1.6).

The non-monotonic behaviour of $C_V(T = T_c)$ seen in Fig.3.1 can also be understood from the viewpoint of the stability of preformed Cooper pairs near T_c. To explain this, it is convenient to write the fluctuation correction N_{NSR} to the number equation in Eq.(2.30) in the spectral representation as [88],

$$N_{NSR} = 2 \int_{-\infty}^{\infty} d\omega\, n_B(\omega)\, \rho_B(\omega)\,. \tag{3.3}$$

In Eq.(3.3),

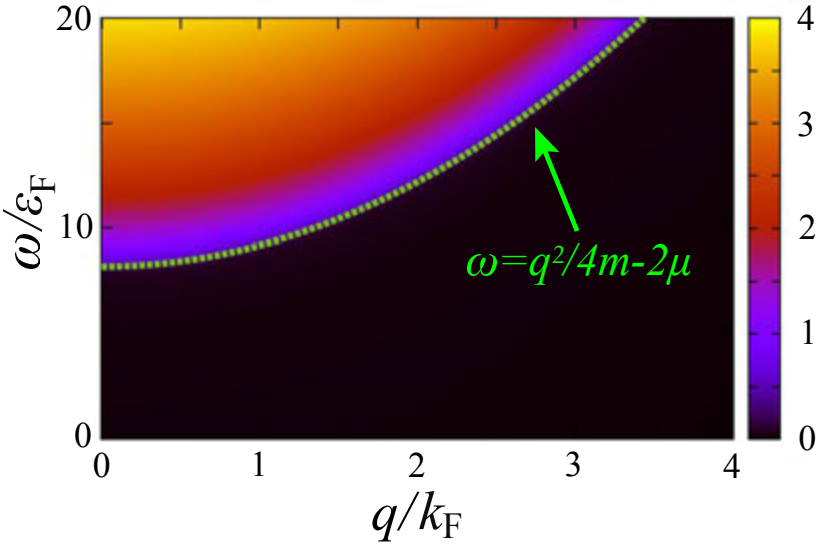

Figure 3.2: Calculated intensity of $\mathrm{Im}\left[\Pi\left(\boldsymbol{q},\omega_{\boldsymbol{q}}+i\delta\right)\right]$ in Eq.(3.9). We set $(k_{\mathrm{F}}a_s)^{-1}=2$ and $T/T_{\mathrm{F}}=0.218$, where $\mu<0$ is realised. The dotted line shows $\omega=q^2/4m-2\mu$. The intensity is normalised by $N\varepsilon_{\mathrm{F}}^{-1}$.

$$n_B(\omega)=\frac{1}{e^{\omega/T}-1} \tag{3.4}$$

is the Bose distribution function, and

$$\rho_B(\omega)=\sum_{\boldsymbol{q}}A_B(\boldsymbol{q},\omega), \tag{3.5}$$

may be viewed as the "molecular Bose density of states", where

$$A_B(\boldsymbol{q},\omega)=-\frac{1}{2\pi}\mathrm{Im}\left[\Gamma(\boldsymbol{q},\omega_+)\frac{\partial}{\partial\mu}\Pi(\boldsymbol{q},\omega_+)\right]. \tag{3.6}$$

Here, $\Gamma(\boldsymbol{q},\omega_+)=\Gamma(\boldsymbol{q},i\nu_n\to\omega+i\delta)$, and, $\Pi(\boldsymbol{q},\omega_+)=\Pi(\boldsymbol{q},i\nu_n\to\omega+i\delta)$ are the analytic continued particle-particle scattering matrix and pair-correlation function, respectively. In the present NSR theory, the former has the form (see Eq.(2.26))

$$\Gamma(\boldsymbol{q},\omega_+)=\frac{1}{\dfrac{m}{4\pi a_s}+\Pi(\boldsymbol{q},\omega_+)-\displaystyle\sum_{\boldsymbol{p}}\frac{1}{2\varepsilon_{\boldsymbol{p}}}}, \tag{3.7}$$

and thus

$$\begin{aligned}A_B(\boldsymbol{q},\omega) &= -\frac{1}{2\pi}\left[\mathrm{Re}\Gamma(\boldsymbol{q},\omega_+)\frac{\partial}{\partial\mu}\mathrm{Im}\Pi(\boldsymbol{q},\omega_+)+\mathrm{Im}\Gamma(\boldsymbol{q},\omega_+)\frac{\partial}{\partial\mu}\mathrm{Re}\Pi(\boldsymbol{q},\omega_+)\right]\\ &= -\frac{1}{2\pi}\left[\mathrm{Re}\Gamma(\boldsymbol{q},\omega_+)\frac{\partial}{\partial\mu}\mathrm{Im}\Pi(\boldsymbol{q},\omega_+)\right.\\ &- \left.\mathrm{Im}\Pi(\boldsymbol{q},\omega_+)\left|\Gamma(\boldsymbol{q},\omega_+)\right|^2\frac{\partial}{\partial\mu}\mathrm{Re}\Pi(\boldsymbol{q},\omega_+)\right],\end{aligned} \tag{3.8}$$

with

$$\mathrm{Im}\Pi(\boldsymbol{q},\omega_+)=\pi\sum_{\boldsymbol{p}}\tanh\left(\frac{\xi_{\boldsymbol{p}+\boldsymbol{q}/2}}{2T}\right)\delta\left(\omega-\left[\frac{\boldsymbol{p}^2}{m}+\frac{\boldsymbol{q}^2}{4m}-2\mu\right]\right). \tag{3.9}$$

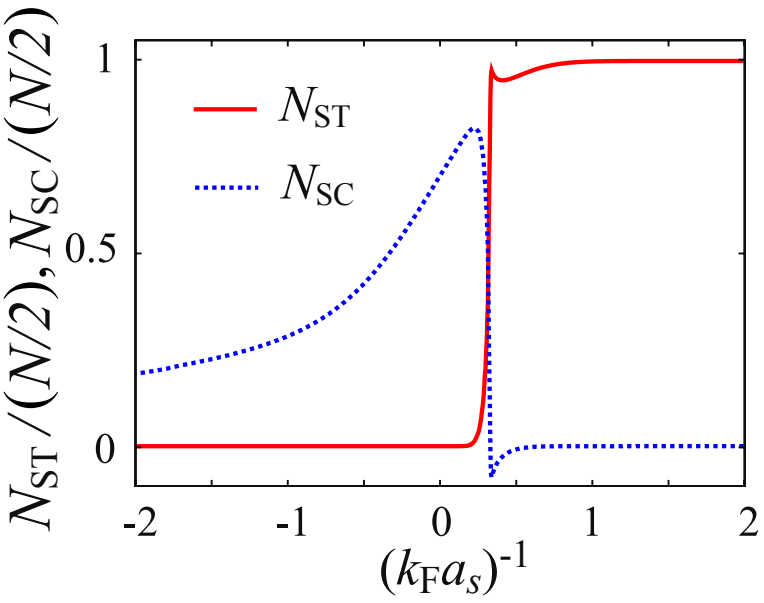

Figure 3.3: The number $N_{\rm ST}$ of stable molecules and the contribution $N_{\rm SC}$ of scattering states, physically describing the number of fluctuating preformed Cooper pairs. We take $T = T_{\rm c}$.

Eq.(3.5), Eq.(3.8) and Eq.(3.9) indicate that the "molecular density of states" $\rho(\omega)$ in quantitatively different in the weak-coupling BCS region where $\mu \geq 0$, and the strong-coupling BEC region where $\mu < 0$. Equation (3.9) indicates that $\rho(\omega)$ is always non-negative in the BCS region where $\mu \geq 0$. We note that $\mu(T = T_{\rm c})$ is positive when $(k_{\rm F}a_s)^{-1} \lesssim 0.3$ (see Fig.2.3) (b).

On the other hand, when $\mu < 0$, $\rho_B(\omega)$ has a finite gap $\Delta E_G^B = 2|\mu|$, because Eq.(3.9) vanishes when $\omega \leq 2|\mu|$, unless $\Gamma(\boldsymbol{q}, \omega_+)$ has poles in the region $0 \leq \omega < 2|\mu|$. To confirm this, we show in Fig.3.2 $\mathrm{Im}\Pi(\boldsymbol{q}, \omega_+)$ in the BEC region when $\mu < 0$. Clearly $\mathrm{Im}\Pi(\boldsymbol{q}, \omega_+)$ vanishes in the low energy region $\omega \leq q^2/4m + 2|\mu|$.

However, $\Gamma(\boldsymbol{q}, \omega_+)$ actually has real poles in this gapped energy region, so that $\rho_B(\omega)$ has δ-function peaks at these poles. The appearance of these real poles physically means the appearance of stable molecules in the strong-coupling regime, when $\mu < 0$. Expanding the denominator of $\Gamma(\boldsymbol{q}, \omega_+)$ in Eq.(3.7) around a real pole $\omega = \omega_{\boldsymbol{q}}$, we have

$$\begin{aligned}\Gamma(\boldsymbol{q}, \omega_+) &\cong \frac{1}{\dfrac{m}{4\pi a_s} + \left[\Pi\left(\boldsymbol{q}, \omega_{\boldsymbol{q}}\right) + \left[\omega_+ - \omega_{\boldsymbol{q}}\right]\dfrac{\partial}{\partial\omega}\Pi\left(\boldsymbol{q}, \omega_+ = \omega_{\boldsymbol{q}}\right) - \displaystyle\sum_{\boldsymbol{p}}\frac{1}{2\varepsilon_{\boldsymbol{p}}}\right]} \\ &= \frac{1}{\left[\omega_+ - \omega_{\boldsymbol{q}}\right]\dfrac{\partial}{\partial\omega_{\boldsymbol{q}}}\Pi\left(\boldsymbol{q}, \omega_{\boldsymbol{q}}\right)}. \end{aligned} \tag{3.10}$$

The number $N_{\rm ST}$ of stable molecules is then evaluated as

$$
\begin{aligned}
N_{\mathrm{ST}} &= -\sum_{\boldsymbol{q}:\mathrm{poles}} \int_{-\infty}^{\infty} \frac{\mathrm{d}\omega}{2\pi} n_{\mathrm{B}}(\omega)\, \mathrm{Im}\left[\frac{\frac{\partial}{\partial\mu}\Pi(\boldsymbol{q},\omega_+)}{\left[\omega_+ - \omega_{\boldsymbol{q}}\right]\frac{\partial}{\partial\omega_{\boldsymbol{q}}}\Pi\left(\boldsymbol{q},\omega_{\boldsymbol{q}}\right)} \right] \\
&= -\sum_{\boldsymbol{q}:\mathrm{poles}} \int_{-\infty}^{\infty} \frac{\mathrm{d}\omega}{2\pi} n_{\mathrm{B}}(\omega)\, \frac{\frac{\partial}{\partial\mu}\Pi(\boldsymbol{q},\omega_+)}{\frac{\partial}{\partial\omega_{\boldsymbol{q}}}\Pi\left(\boldsymbol{q},\omega_{\boldsymbol{q}}\right)} \mathrm{Im}\left[\frac{1}{\omega_+ - \omega_{\boldsymbol{q}}} \right] \\
&= \sum_{\boldsymbol{q}:\mathrm{poles}} \int_{-\infty}^{\infty} \frac{\mathrm{d}\omega}{2} n_{\mathrm{B}}(\omega)\, \frac{\frac{\partial}{\partial\mu}\Pi(\boldsymbol{q},\omega_+)}{\frac{\partial}{\partial\omega_{\boldsymbol{q}}}\Pi\left(\boldsymbol{q},\omega_{\boldsymbol{q}}\right)} \delta\left(\omega - \omega_{\boldsymbol{q}}\right) \\
&= \frac{1}{2} \sum_{\boldsymbol{q}:\mathrm{poles}} n_{\mathrm{B}}\left(\omega_{\boldsymbol{q}}\right) \frac{\frac{\partial}{\partial\mu}\Pi\left(\boldsymbol{q},\omega_{\boldsymbol{q}}\right)}{\frac{\partial}{\partial\omega_{\boldsymbol{q}}}\Pi\left(\boldsymbol{q},\omega_{\boldsymbol{q}}\right)},
\end{aligned}
\tag{3.11}
$$

where the summation is taken over the real poles of $\Gamma(\boldsymbol{q},\omega_+)$, under the condition $\mathrm{Im}\Pi(\boldsymbol{q},\omega_+) = 0$.

Then, the correction term N_{NSR} in Eq.(3.7) is given by the sum of the number N_{ST} of "stable" molecules in Eq.(3.11) and the so-called *scattering states* N_{SC} [15, 19], that is

$$N_{\mathrm{NSR}} = 2N_{\mathrm{ST}} + 2N_{\mathrm{SC}}. \tag{3.12}$$

Physically, N_{SC} may be interpreted as the number of fluctuating preformed Cooper pairs associated with strong pairing fluctuations.

Figure 3.3 shows that N_{ST}, as well as $N_{\mathrm{SC}} = N_{\mathrm{NSR}}/2 - N_{\mathrm{ST}}$ (where N_{NSR} is calculated from Eq.(2.30)) in the BCS-BEC crossover region at T_{c}. Starting from the weak coupling regime, the scattering states N_{SC} gradually increases with increasing interaction strength, indicating the enhancement of pairing fluctuations near T_{c}. This corresponds to the amplification of $C_V(T = T_{\mathrm{c}})$ around the unitarity limit seen in Fig.3.1. However, N_{SC} is suddenly suppressed in the strong coupling BEC regime when the Fermi chemical potential becomes negative (around $(k_{\mathrm{F}}a_s)^{-1} = 0.3$). Instead, the stable molecules (N_{ST}) dominantly contribute to the number equation there. These molecules have a definite binding energy, which eventually becomes the large two-body bound state energy $E_{\mathrm{bind}} = 1/ma_s^2$ deep inside the BEC regime, so that effects of pairing fluctuations on C_V is suppressed there. Finally C_V approaches C_V^{B} in Eq.(3.2), as shown in Fig.3.1.

3.2 Specific Heat Above T_{c}

Fig.3.4 (a) shows the calculated specific heat C_V above T_{c}. In this figure, one sees that the detailed temperature dependence remarkably depends on the interaction strength, implying that this thermodynamic quantity is sensitive to system properties in the BCS-BEC crossover. We briefly note that the internal energy, which is related to C_V as Eq.(2.35) always monotonically decreases with decreasing temperature, as shown in Fig.3.4 (b). This indicates that C_V is a more useful quantity than E in considering properties of an ultracold Fermi gas in the BCS-BEC crossover regime.

For the following two subsections, we separately examine the origin of the temper-

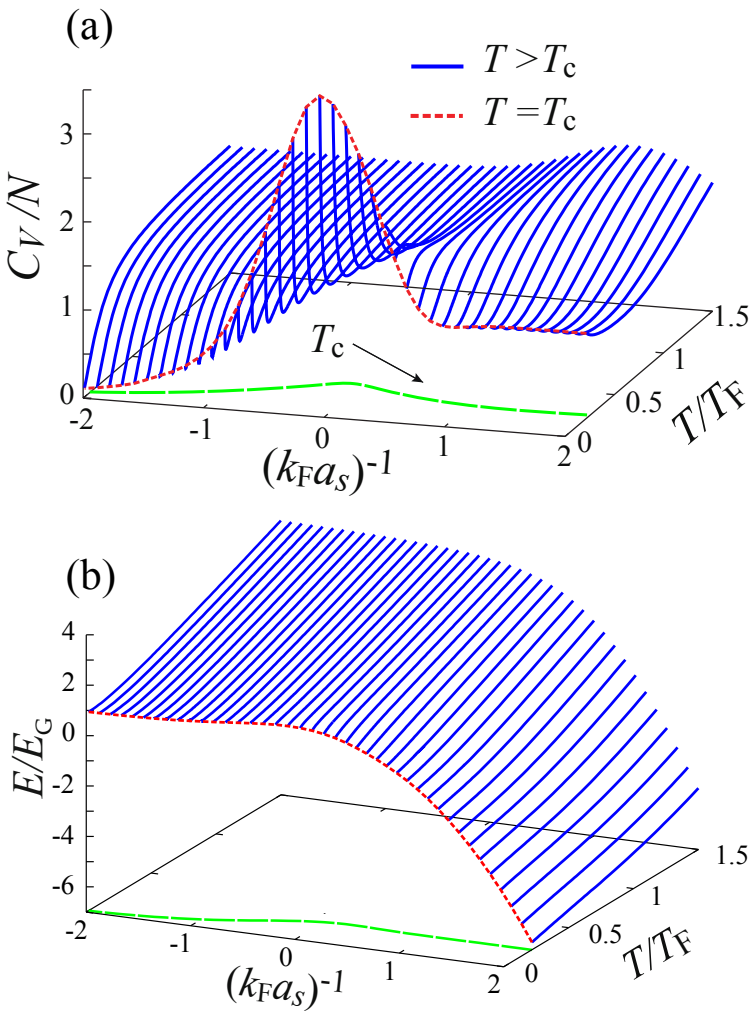

Figure 3.4: Calculated Specific heat at constant volume C_V (a), and the internal energy E (b) in the BCS-BEC crossover regime of an ultracold Fermi gas above T_c. $E_G = \frac{3}{5}\varepsilon_F$ is the internal energy of a free Fermi gas at $T = 0$.

ature dependence of C_V in the strong ($(k_F a_s)^{-1} \gtrsim 0$) and weak coupling ($(k_F a_s)^{-1} \lesssim 0$) side.

3.2.1 The Strong Coupling Side $(k_F a_s)^{-1} \gtrsim 0$

Figure.3.5 shows the specific heat C_V in the strong-coupling side of the crossover region. When $(k_F a_s)^{-1} = 0.2$, C_V remarkably increases with decreasing temperature near T_c, giving the amplification of $C_V(T = T_c)$ in the unitarity regime in Fig.3.1. As mentioned previously, this behaviour is due to the suppression of entropy S by the formation of fluctuating preformed Cooper pairs near T_c. However, this behaviour is found to soon disappear as one increases the interaction strength. When $(k_F a_s)^{-1} = 0.6$, Fig.3.5 shows that C_V monotonically increases with increasing the temperature near T_c, which is the opposite tendency compared to the $(k_F a_s)^{-1} = 0.2$ case.

As shown in Fig.3.3 long-lived stable molecules appear in the BEC side when $(k_F a_s)^{-1} \gtrsim 0.3$. However, since the binding energy E_{bind} in this regime is still

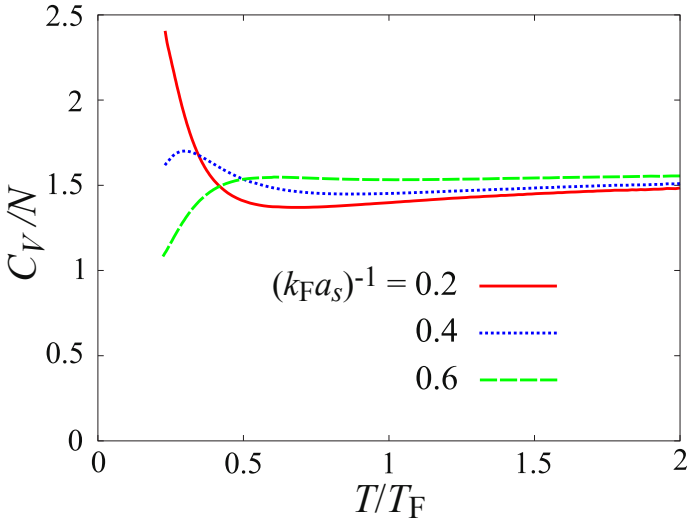

Figure 3.5: Calculated specific heat C_V in the strong coupling BEC side of the crossover region ($0.2 \leq (k_F a_s)^{-1} \leq 0.6$).

small, the thermal dissociation of these molecules can easily occur near T_c, which is expected to dominantly contribute to the temperature dependence of C_V in this regime (at least near T_c). Indeed, simply considering this effect by dealing with a two-level system with energy $\omega = 0$ and $\omega = E_{\rm bind}$, we obtain

$$C_V = \left(\frac{E_{\rm bind}}{2T}\right)^2 {\rm sech}^2\left(\frac{E_{\rm bind}}{2T}\right). \tag{3.13}$$

This model specific heat *monotonically* increases with increasing the temperature, when $T \lesssim E_{\rm bind}/2$, as the behaviour of $C_V(T \gtrsim T_c)$ when $(k_F a_s)^{-1} = 0.6$ in Fig.3.5. Thus, the increase of C_V with increasing temperature near T_c in this regime is attributed to the thermal dissociation of (weakly bound) stable molecules.

As we go deeper inside the BEC regime, Fig.3.6 shows that the enhancement of C_V near T_c revives, although it is not so remarkable as that in the unitary regime (see Fig.3.5 for $(k_F a_s)^{-1} = 0.2$). As the interaction strength increases, Fig.3.6 (b) and (c) shows that C_V near T_c is well described by that of an ideal gas of $N/2$ Bose molecules with a molecular mass $M = 2m$, although this agreement becomes worse at high temperatures. From this result, when we introduce the characteristic temperature $\tilde{T}$ in this regime, as the temperature at which C_V takes a minimum value (vertical dashed line in Fig.3.6), the system in the region $T_c \leq T \lesssim \tilde{T}$ may be viewed as an ideal molecular Bose gas, rather that an interacting Fermi gas. Indeed, one finds that most of the Fermi atoms form stable molecules, giving $N_{\rm ST} = N/2$, in this regime (see Fig.3.6 (d)~(f)). Above $\tilde{T}$, these molecules start to thermally dissociate into Fermi atoms, leading to $N_{\rm ST} < N/2$, as shown in Fig.3.6 (d)~(f).

Before ending this subsection, we analytically show that the specific heat C_V is reduced to $C_V^{\rm B}$ in the BEC limit. In this limit, $\mu/\varepsilon_F \ll -1$, so that one can ignore the Fermi distribution function $n_F\left(\xi_{\boldsymbol{p}}\right)$ in the pair correlation function $\Pi\left(\boldsymbol{q}, i\nu_n\right)$ in Eq.(2.17), which gives

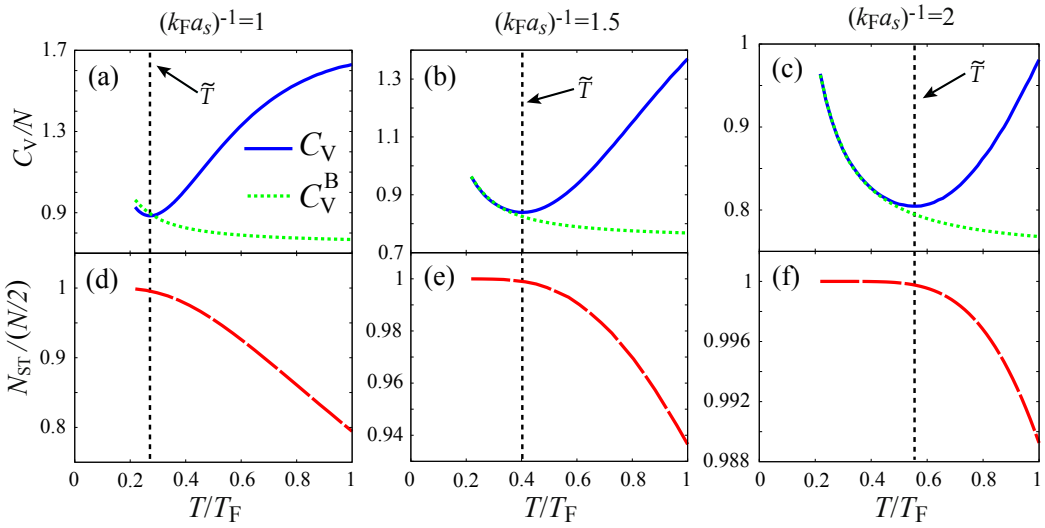

Figure 3.6: (a)~(c) Calculated specific heat $C_V(T \geq T_c)$ in the strong-coupling BEC regime. C_V^B is the specific heat in an ideal gas of $N/2$ bosons with a molecular mass $m_B = 2m$. (d)~(f) Temperature dependence of the number N_{ST} of stable pairs in Eq.(2.8). The characteristic temperature $\tilde{T}$ is given as the temperature at which C_V takes a minimal value (vertical dotted line) in the BEC regime.

$$\begin{aligned}\Pi(\boldsymbol{q}, i\nu_n) &= -\sum_{\boldsymbol{p}} \frac{1}{i\nu_n - \xi_{\boldsymbol{p}+\boldsymbol{q}/2} - \xi_{\boldsymbol{p}-\boldsymbol{q}/2}} \\ &= \sum_{\boldsymbol{p}} \frac{1}{2\varepsilon_{\boldsymbol{p}}} - m\int_0^\infty \frac{\mathrm{d}p}{2\pi^2} \frac{\frac{q^2}{4} - 2m\mu - m\,i\nu_n}{p^2 + \frac{q^2}{4} - 2m\mu - m\,i\nu_n} \\ &= \sum_{\boldsymbol{p}} \frac{1}{2\varepsilon_{\boldsymbol{p}}} - \frac{m}{4\pi}\sqrt{m\left[\frac{q^2}{4m} - 2\mu - i\nu_n\right]}. \end{aligned} \tag{3.14}$$

Substituting this into the particle-particle scattering matrix Eq.(2.26), we obtain

$$\begin{aligned}\Gamma(\boldsymbol{q}, i\nu_n) &= \frac{4\pi}{m} \frac{1}{\left(\frac{1}{a_s} - \sqrt{m\left[\frac{q^2}{4m} - 2\mu - i\nu_n\right]}\right)} \\ &= \frac{4\pi}{m^2 a_s} \frac{\left(1 + \sqrt{\frac{1}{E_{\mathrm{bind}}}\left[-i\nu_n + \frac{q^2}{4m} - \mu_B + E_{\mathrm{bind}}\right]}\right)}{i\nu_n - \frac{q^2}{4m} + \mu_B}, \end{aligned} \tag{3.15}$$

where

$$\mu_B = 2\mu + E_{\mathrm{bind}}, \tag{3.16}$$

with $E_{\mathrm{bind}} = 1/ma_s^2$ being the binding energy of a two-body bound molecule. Because $E_{\mathrm{bind}}/\varepsilon_F = 2/(k_Fa_s)^2 \to \infty$ in the extreme BEC limit, the square root in Eq.(3.15) is further approximated to

$$\sqrt{\frac{1}{E_{\rm bind}}\left[-i\nu_n+\frac{q^2}{4m}-\mu_B+E_{\rm bind}\right]}=\sqrt{1-\frac{1}{E_{\rm bind}}\left[i\nu_n-\frac{q^2}{4m}+\mu_B\right]}\to 1. \quad (3.17)$$

Then Eq.(3.15) is reduced to

$$\Gamma(\boldsymbol{q},i\nu_n)=\frac{8\pi}{m^2a_s}\frac{1}{i\nu_n-\frac{q^2}{4m}+\mu_B}, \quad (3.18)$$

which is just the Bose Green's function mass $2m$ and chemical potential μ_B, multiplied by the factor $8\pi/m^2a_s$.

Substituting Eq.(3.18) into Eq.(2.34), we can evaluate the NSR strong coupling correction $E_{\rm NSR}$ to the internal energy in the deep BEC limit as,

$$\begin{aligned}E_{\rm NSR}&=-T^2\sum_{\boldsymbol{q},i\nu_n}e^{i\nu_n\delta}\frac{1}{\frac{m}{4\pi a_s}+\Pi(\boldsymbol{q},i\nu_n)-\sum_{\boldsymbol{p}}\frac{1}{2\varepsilon_{\boldsymbol{p}}}}\frac{\partial}{\partial T}\Pi(\boldsymbol{q},i\nu_n)\\&=-T^2\frac{\partial}{\partial T}\sum_{\boldsymbol{q},i\nu_n}e^{i\nu_n\delta}\log\left(i\nu_n-\frac{q^2}{4m}+\mu_{\rm B}\right)\\&=-T\sum_{\boldsymbol{q},i\nu_n}e^{i\nu_n\delta}\frac{i\nu_n}{i\nu_n-\frac{q^2}{4m}+\mu_{\rm B}}\\&=\sum_{\boldsymbol{q}}\left(\frac{q^2}{4m}-\mu_{\rm B}\right)n_B\left(\frac{q^2}{4m}-\mu_{\rm B}\right).\end{aligned} \quad (3.19)$$

The internal energy E in Eq.(2.32) in the BEC limit is obtained as

$$\begin{aligned}E&=\sum_{\boldsymbol{q}}\left(\frac{q^2}{4m}-\mu_{\rm B}\right)n_B\left(\frac{q^2}{4m}-\mu_{\rm B}\right)+2\mu\sum_{\boldsymbol{q}}n_B\left(\frac{q^2}{4m}-\mu_{\rm B}\right)\\&=\sum_{\boldsymbol{q}}\frac{q^2}{4m}n_B\left(\frac{q^2}{4m}-\mu_{\rm B}\right)-E_{\rm bind}\sum_{\boldsymbol{q}}n_B\left(\frac{q^2}{4m}-\mu_B\right)\\&\equiv E_B-E_{\rm bind}N_B,\end{aligned} \quad (3.20)$$

where we have dropped the free Fermi gas term E_0 in Eq.(2.32) because $\mu/\varepsilon_{\rm F}\ll -1$. In the last line $E_{\rm B}$ is the kinetic energy of $N_{\rm B}$ molecular bosons with a molecular mass $2m$. When all the Fermi atoms form tightly bound molecules in the extreme BEC regime, one may take $N_{\rm B}=N/2$, leading to

$$E=\sum_{\boldsymbol{q}}\frac{q^2}{4m}n_{\rm B}\left(\frac{q^2}{4m}-\mu_{\rm B}\right)-E_{\rm bind}\frac{N}{2}. \quad (3.21)$$

Since $C_V=(\partial E/\partial T)_{V,N}$ is simply obtained from the first term in Eq. (3.21), it is just the same as the specific heat in an ideal gas with $N/2$ two-body bound molecules.

With increasing temperature above $\tilde{T}$, the gradual decrease of the number $N_{\rm B}$ of stable pairs from $N/2$, shown in Figs.3.6 (d)~(f), indicates the thermal dissociation of molecular bosons. The last term $E_{\rm bind}N_{\rm B}$ in Eq. (3.20) shows that this phenomenon naturally increases C_V, giving the deviation from $C_V^{\rm B}$ seen in Figs3.6 (a)~(c).

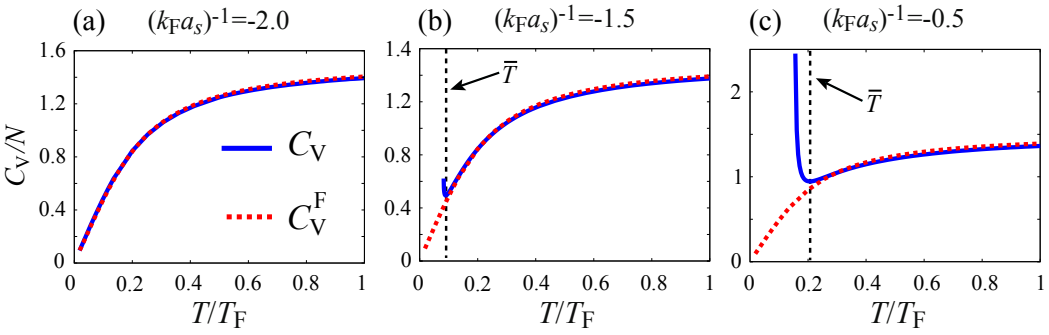

Figure 3.7: Temperature dependence of specific heat C_V in the weak coupling BCS side ($(k_Fa_s)^{-1} \lesssim 0$) of the crossover. C_V^F is the specific heat of a free Fermi gas, given in Eq.(3.22). The characteristic temperature $\bar{T}$ is determined as the temperature at which C_V becomes has a minimum value.

3.2.2 The Weak Coupling Side $(k_Fa_s)^{-1} \lesssim 0$

We now turn our attention to the weak coupling BCS side ($(k_Fa_s)^{-1} \lesssim 0$). We see in Fig.3.7 (c) that the remarkable amplification of C_V seen at T_c soon disappears with increasing temperature, to approach the specific heat C_V^F of a free Fermi gas, given by

$$C_V^F = 2\sum_{\boldsymbol{p}} \varepsilon_{\boldsymbol{p}} \frac{\partial n_F(\xi_{\boldsymbol{p}})}{\partial T}. \tag{3.22}$$

This means that fluctuating preformed Cooper pairs gradually disappears as the temperature increases from T_c. We briefly note that C_V^F in Eq.(3.22) approaches the classical Dulong-Petit law [89] ($C_V = 3N/2$) from below, in the high temperature limit.

Introducing another characteristic temperature $\bar{T}$ as the temperature at which C_V takes a minimum value in this region, the lower ($T \lesssim \bar{T}$) and the higher ($T \gtrsim \bar{T}$) temperature side may be viewed as a Fermi gas with strong pairing fluctuations, and a normal Fermi gas, respectively. As one approaches the weak coupling regime, the characteristic temperature $\bar{T}$ decreases as shown in Fig.3.7 (a)~(c), which means the shrinkage of the fluctuation regime with decreasing interaction strength, as expected.

3.3 Specific Heat Below T_c

Figure.3.8 shows the specific heat C_V in the superfluid state of a ultracold Fermi gas in the BCS-BEC crossover region. In contrast to the case of the normal state above T_c, the overall temperature dependence below T_c is not so dependent on the strength of a pairing interaction. In the weak-coupling BCS regime both Bogoliubov single-particle excitations accompanied by pair-breaking and a gapless collective Goldstone mode are considered to contribute to C_V ($T \leq T_c$). In the strong coupling BEC regime, the former becomes irrelevant because the binding energy $E_{\rm bind} = 1/ma_s^2$ is much larger than $T_c(\simeq 0.218T_F)$, so that most pairs remain even at T_c. Thus, the latter collective excitations dominate over C_V in this regime, as in the case of the ordinary Bose superfluid.

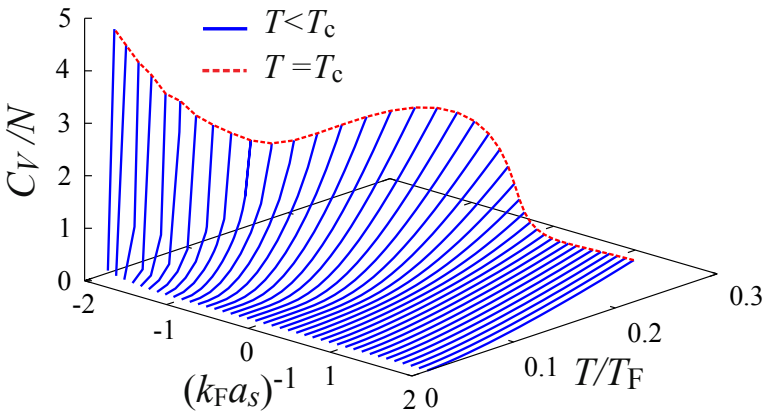

Figure 3.8: Calculated specific heat C_V BCS-BEC crossover regime of a superfluid Fermi gas below T_c.

3.4 Phase Diagram Of An Ultracold Fermi Gas

When we compare the two characteristic temperature $\tilde{T}$ and $\bar{T}$ introduced in the previous section with the pseudogap temperature T^* [22, 23] (below which the pseudogap appears in the density of states near the Fermi level), as well as the spingap temperature T_s [24] (below which the spin susceptibility is anomalously suppressed by the preformed pair formation), we find that $\bar{T}$ is close to T^* and T_s as shown in Fig.3.9. In this regard, we recall that the right side of T^* and T_s is sometimes referred to as the pseudogap regime in cold Fermi gas physics, where strong pairing fluctuations dominate over system properties. Thus, from the viewpoint of the specific heat C_V, $\bar{T}$ is found to physically give the boundary between the pseudogap regime and the normal Fermi gas regime (although there is no phase transition at $\bar{T}$).

As mentioned previously, the region bellow the characteristic temperature $\tilde{T}$, obtained in the strong coupling BEC regime, may be physically viewed as an ideal molecular Bose gas. Thus, together with the above discussion, the temperatures $\tilde{T}$ works as the boundary between the pseudogap regime and the molecular Bose gas regime.

We note that no characteristic temperature corresponding to $\tilde{T}$ has so far been obtained from analysis on the density of states $\rho(\omega)$ (which only gives the pseudogap temperature T^*), or the spin susceptibility χ_s (which only gives the spin gap temperature T_s). This is because, in the BEC regime, $\rho(\omega)$ almost vanishes around $\omega = 0$ due to the opening of large pseudogap [22, 23], and χ_s is also suppressed due to the spin-singlet pair formation, so that it is difficult to extract useful information from these quantities there. In contrast, the specific heat does not vanish even in the strong coupling regime, leading to $\tilde{T}$. This is an advantage of using this thermodynamic quantity for the study of BCS-BEC crossover physics.

We note that, as the boundary between the normal Bose gas regime and the pseudogap regime, it has been proposed that $T = 2|\mu|$ in the BEC regime (where $\mu < 0$) [22, 23]. This proposal is based on the fact that $2|\mu|$ eventually coincides with the binding energy $E_{\rm bind} = 1/(ma_s^2)$ of a molecular boson in the BEC

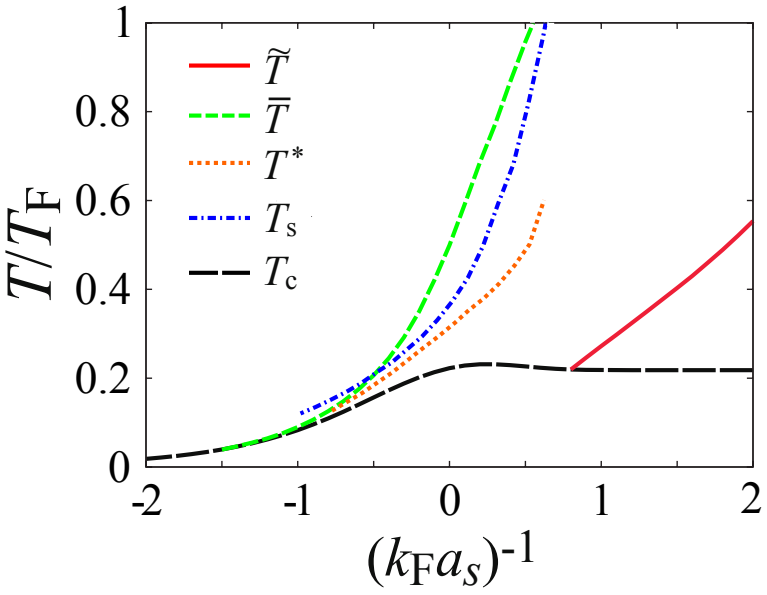

Figure 3.9: Comparison of $\tilde{T}$ and $\bar{T}$ with various characteristic temperatures discussed in the BCS-BEC crossover regime of an ultracold Fermi gas. T^* is the pseudogap temperature, below which a dip appears in the single-particle density of states near the Fermi level [22, 23]. T_s is the spingap temperature, below which the spin susceptibility is suppressed by the formation of preformed Cooper pairs [24]. The right side of these characteristic temperatures is called the pseudogap regime in the literature. $\tilde{T}$ and $\bar{T}$ are introduced in this thesis. In this figure, except for T_c, no phase transitions occur at these characteristic temperatures.

limit. Stable molecules are thus expected to appear below $2|\mu| \sim E_{\rm bind}$, overwhelming thermal dissociation. However, when we compare $2|\mu|$ with $\tilde{T}$, we find that $2|\mu| \gg \tilde{T}$. This indicates that, although stable molecules are expected to appear around $2|\mu| \sim E_{\rm bind}$, this does not immediately indicate the realisation of a molecular Bose gas. Instead, to realise a gas of long-lived stable molecules, the temperature needs to be further decreased down to $\tilde{T}$. In this sense, the region between $2|\mu|$ and $\tilde{T}$ may be regarded as the crossover region between a gas of metastable molecules and that of long-lived stable molecules.

Summarising our results and discussions, we obtain the phase diagram of an ultracold Fermi gas shown in Fig.3.10. Using the two characteristic temperatures $\bar{T}$ and $\tilde{T}$, we can divide the normal state above T_c into (1) normal Fermi gas regime (NF), (2) pseudogap regime (PG), and (3) molecular Bose gas regime (MB). Although there is no phase transition at $\bar{T}$ or $\tilde{T}$, this phase diagram would be useful in understanding strong-coupling properties of this system in the BCS-BEC crossover region.

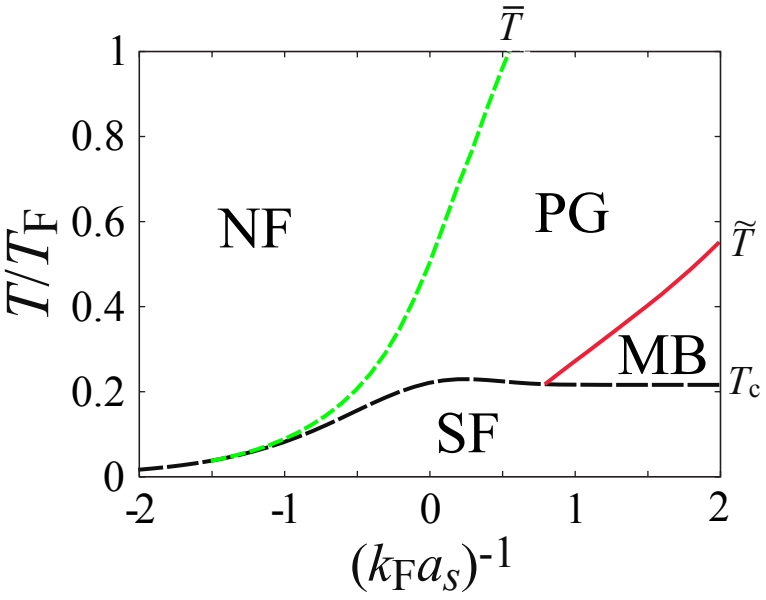

Figure 3.10: Phase diagram of an ultracold Fermi gas in terms of the interaction strength and the temperature, based on the analysis on the specific heat. SF: superfluid phase. NF: Normal Fermi gas regime. PG: pseudogap regime. MB: molecular Bose gas regime. In this phase diagram T_c is the only phase transition temperature. $\bar{T}$ and $\tilde{T}$, are characteristic temperatures without being accompanied by any spontaneous symmetry breaking.

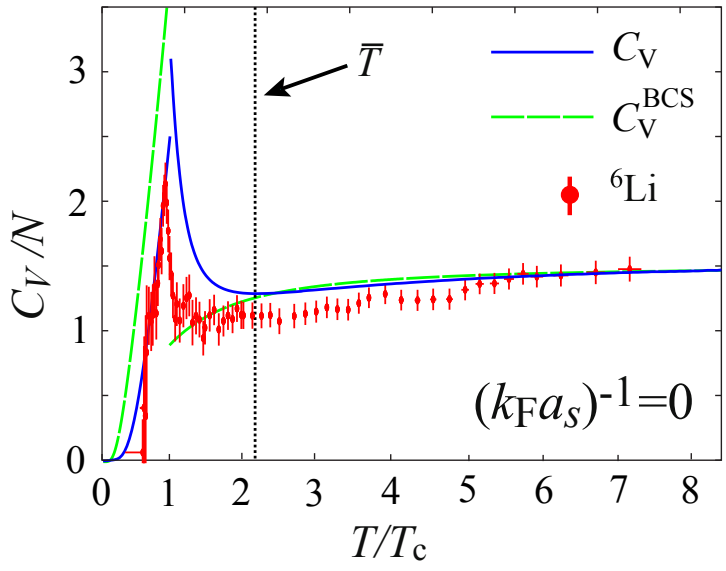

Figure 3.11: Comparison of our theoretical results with the resent experiment on a ^{6}Li unitary Fermi gas [32]. In this figure, the temperature is normalised by T_c. C_V^{BCS} is the specific heat in the mean field BCS-theory. The vertical dashed line shows $\bar{T}$, where the calculated C_V has a minimum value.

3.5 Comparison With Experiment

Finally, in this section we compare our result with the recent experiment on a ^{6}Li unitary Fermi gas [32] in Fig.3.11. The overall behaviour of our result agrees with the experimental data, especially in the superfluid phase below T_c. However, the calculated C_V in the pseudogap regime ($T_c \leq T \lesssim \bar{T}$) is somehow larger than the observed C_V. In this regard, we note that the experimental group states that a finite spacial resolution inherent in this experiment in a trapped geometry could lead to a possible suppression of the specific heat near T_c [32]. Thus, further analysis including these effects are needed to quantitatively explain this experimental result, which remains as our future problem.

Chapter 4

Application To Neutron Star Equation Of State

In this chapter we propose an idea to study the low density crust regime of a neutron star, by using a superfluid Fermi atomic gas near the unitary regime. In this idea, we first construct a reliable strong-coupling theory which can well explain the ground state properties of an ultracold Fermi gas, and apply it to the neutron star equation of state, by making up for the difference between the two systems in a theoretical manner. In Sec.1.4, we show that the superfluid NSR theory explained in Sec.2.2 well explains the recent experiment of a ^{6}Li superfluid Fermi gas in the BCS-unitary regime. Being based on this result, we apply the extended NSR theory (including the non-vanishing effective range $r_{\rm eff} = 2.7$ fm) presented in Sec.2.3, to calculate the neutron star equation of state (EOS) in Sec.4.2. In Sec.4.3 we examine how thermodynamic properties of an interacting Fermi gas vary when we tune $r_{\rm eff}$. In Sec.4.4 we discuss corrections to the neutron star EOS due to higher order density corrections.

4.1 EOS Of A Superfluid Fermi Gas In The BCS-Unitary Regime

Figure 4.1 shows self-consistent solutions for the Fermi chemical potential μ and the superfluid order parameter Δ obtained by the superfluid NSR theory explained in Sec.2.2. We find that our results agree well with recent experiments on ^{6}Li superfluid Fermi gases [33, 94], as well as theoretical Monte-Carlo simulation [93].

We note that the mean-field based BCS-Leggett strong-coupling theory cannot quantitively explain the observed μ and Δ, as shown in Fig.4.1. That is, even at low temperatures where thermal fluctuations are considered to be almost absent, we still need to take into account strong-coupling corrections beyond the mean-field level. For this purpose, Fig.4.1 indicates that the NSR scheme works well near $T/T_{\rm F} = 0$. Indeed, when we evaluate the internal energy E by using the NSR results for μ and Δ in Fig.4.1, it is found to well explain the recent experiment, as shown in Fig.4.2. (Note that the BCS-Leggett theory again overestimates E.)

As mentioned in Sec.2.3.3, in our numerical calculations targeting the ground state we set the temperature to $T/T_{\rm F} = 0.02$. We briefly note that, except in the

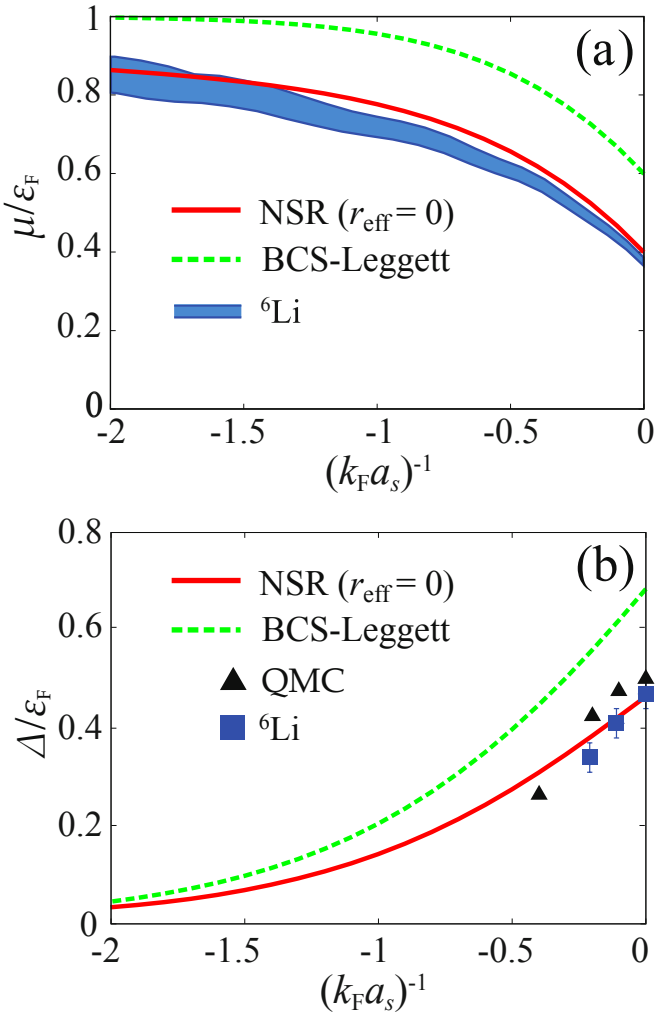

Figure 4.1: Self-consistent solutions for the coupled gap equation (2.54) with the number equation (2.55) and (2.56) in the BCS-Unitary regime of a superfluid Fermi gas. (a) Chemical potential μ. (b) Superfluid order parameter Δ. In both cases, the effective range $r_{\rm eff} = 0$ fm. In panel (a) the shaded line is the experimental result on a ^{6}Li Fermi gas [33]. In panel (b) "QMC" shows the result by quantum Monte-Carlo simulation [93]. "^{6}Li" shows the experimental results by Bragg spectroscopy [94].

weak coupling regime ($(k_{\rm F}a_s)^{-1} \lesssim -1$), $T_{\rm c}$ is much higher than $T/T_{\rm F} = 0.02$ (see Fig.2.3 (a)). Thus, our results around the unitarity limit may be regarded as those in the ground state at $T/T_{\rm F} = 0$.

4.2 Neutron Star Equation Of State In The Low Density Regime

In Sec. 4.1, we have confirmed that the superfluid NSR theory can correctly deal with strong-coupling effects on the internal energy in the unitary regime of a superfluid atomic Fermi gas near $T = 0$, we now extend this scheme to include the non-vanishing effective range $r_{\rm eff} = 2.7$ fm, for the study of EOS of a neutron star in the low density crust regime. (This extension has been explained in Sec.2.3).

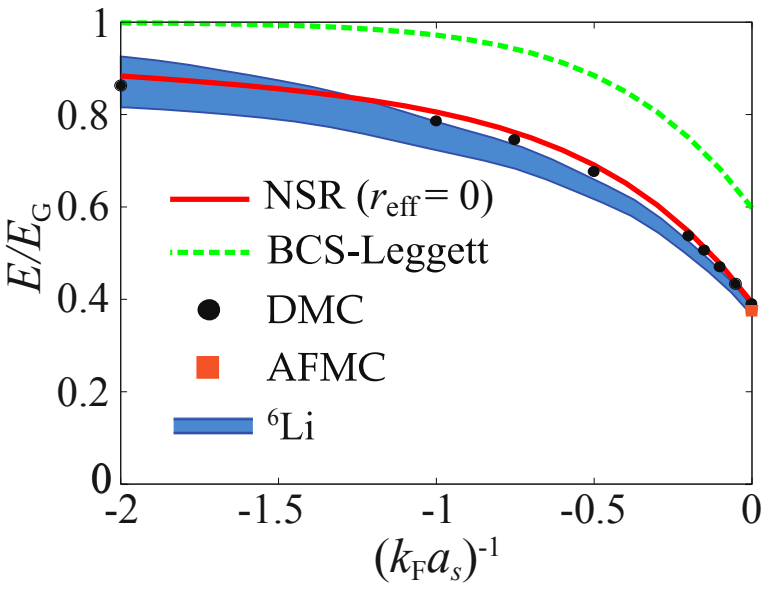

Figure 4.2: Calculated internal energy E in the BCS-unitary regime of a superfluid Fermi gas at $T/T_F = 0.02$ (solid line). The dashed line shows the result in the BCS-Leggett theory. "DMC" and "AFMC" show the results from diffusion Monte-Carlo and auxiliary field Monte Carlo simulations, respectively [93]. "^{6}Li" shows the experimental result on a ^{6}Li superfluid Fermi gas [33].

Figure.4.3 shows the calculated Fermi chemical potential μ, as well as the superfluid order parameter $\Delta = \gamma_{\boldsymbol{p}}/\Delta_{\boldsymbol{p}}$ within the framework of the superfluid NSR theory for the s-wave neutron interaction (where $a_s = -18.5$ fm and $r_{\rm eff} = 2.7$ fm). In this figure, sine the Fermi momentum k_F is proportional to $n^{1/3}$ (where n is the neutron density), the x-axis is related to the depth of a neutron star, from the surface. In panel (a), comparing "NSR($r_{\rm eff} = 2.7$ fm)" and "NSR($r_{\rm eff} = 0$ fm)", we find that effects of the non-vanishing effective range becomes remarkable in the high density region when $k_F \gtrsim 0.8$ fm^{-1}. Regarding this, we recall that the effective range $r_{\rm eff} = 2.7$ fm gives the momentum cutoff $p_c = 0.79$ fm^{-1} (see Eq.(2.73)). As a result, effects of this cutoff become crucial when the Fermi energy $\varepsilon_{\rm eff} = k_F^2/2m$ becomes comparable to the cutoff energy $\omega = p_c^2/2m$.

However, Fig.4.3 (b) shows that the difference between "NSR($r_{\rm eff} = 2.7$ fm)" and "NSR($r_{\rm eff} = 0$ fm)" has already been remarkable when $k_F \sim p_c = 0.79$ fm^{-1}, indicating that the superfluid order parameter is more sensitive to the cutoff momentum p_c than the chemical potential μ.

We note that the present superfluid order parameter,

$$\Delta_{\boldsymbol{p}} = \gamma_{\boldsymbol{p}}\Delta = \frac{\Delta}{\sqrt{1+\left(\frac{p}{p_c}\right)^2}}, \tag{4.1}$$

depends on the momentum $\boldsymbol{p}$. Thus, Δ shown in Fig.4.3 (b) does not immediately give the so-called superfluid energy gap $E_{\rm gap}$. (Note that $E_{\rm gap} = \Delta$ when $r_{\rm eff} = 0$, or $p_c \to \infty$, as far as $\mu > 0$.) Indeed, when we evaluate the threshold energy $E_{\rm gap}$ of

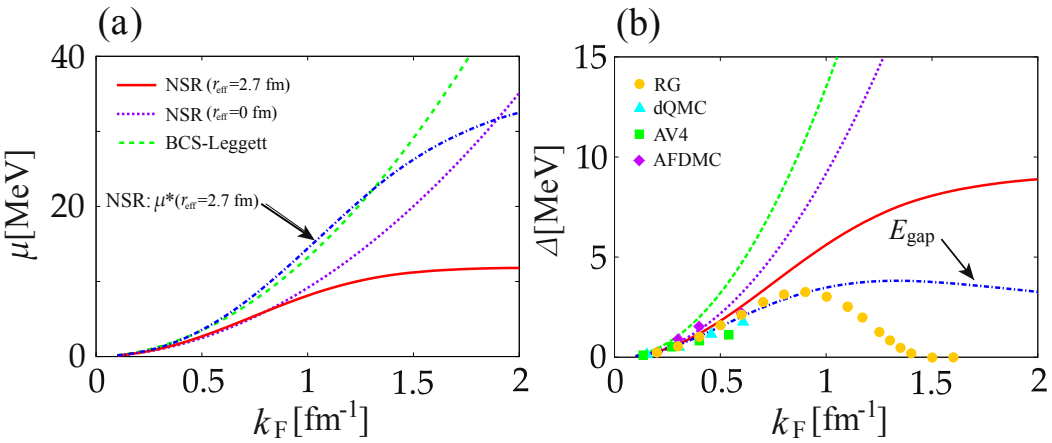

Figure 4.3: Self-consistent solution for the coupled gap equation (2.81) with the NSR number equation (2.88) (solid line). (a) Fermi chemical potential μ. (b) Superfluid order parameter $\Delta = \gamma_{\boldsymbol{p}}/\Delta_{\boldsymbol{p}}$. We set $a_s = -18.5$ fm, $r_{\rm eff} = 2.7$ fm, and $m_n = 936$ MeV/c^2 for the study of neutron matter. Energy is measured in units of MeV. For comparison, we also show the NSR results with $r_{\rm eff} = 0$ (dotted line), as well as the mean field BCS-Leggett result (dashed line). In panel (a) the dashed-dotted line shows the effective chemical potential $\mu^* = \mu + U(a_s, r_{\rm eff})N_{\rm MF}/2$ calculated from the NSR theory with $r_{\rm eff} = 2.7$ fm. In panel (b) the dashed-dotted line shows the threshold energy of the Bogoliubov single-particle dispersion $\tilde{E}_{\boldsymbol{p}} = \sqrt{\tilde{\xi}_{\boldsymbol{p}}^2 + \Delta_{\boldsymbol{p}}^2}$. The solid squares, solid circles, solid triangles, and solid diamonds, show the results for the threshold energy by quantum Monte-Carlo simulation [47], renormalisation group [95], deterministic quantum Monte-Carlo simulation [96], and auxiliary field Monte-Carlo simulation [97], respectively.

the Bogoliubov single-particle dispersion $\tilde{E}_{\boldsymbol{p}} = \sqrt{\tilde{\xi}_{\boldsymbol{p}}^2 + \Delta_{\boldsymbol{p}}^2}$, it is given as the value of $\Delta_{\boldsymbol{p}}$ at the momentum $\tilde{p}_{\rm F}$ satisfying

$$0 = \tilde{\xi}_{\tilde{p}_{\rm F}} = \frac{\tilde{p}_{\rm F}^2}{2m} - \mu^*, \tag{4.2}$$

when

$$\mu^* = \mu + U(a_s, r_{\rm eff})N_{\rm MF}/2 \tag{4.3}$$

is the Fermi chemical potential including the Hartree shift (we show μ^* in Fig.4.3 (a)). As shown in Fig.4.3 (b) the energy gap $E_{\rm gap}$ is actually found to be smaller than Δ. We also find that the present $E_{\rm gap}$ agrees with previous work in the low-density regime where $k_{\rm F} \lesssim p_{\rm c} = 0.79$ fm^{-1}.

When $k_{\rm F} \gtrsim p_{\rm c} = 0.79$ fm^{-1}, our $E_{\rm gap}$ becomes larger than the previous result [95]. This is because the present simple effective range theory in the s-wave scattering channel overestimates the phase shift (or the interaction strength) of the s-wave neutron-neutron interaction when $k_{\rm F} \gtrsim p_{\rm c} = 0.79$ fm^{-1} (see Fig.4.4 (b)), leading to the overestimation of Δ. In addition, non-s-wave interactions, such as the p-wave one , becomes strong in the high density region, as shown in Fig.4.4 (b). While ref [95] involves this realistic situation of the neutron star interior to some extent, our approach ignores these. Thus, the present approach is restricted to the low density region $k_{\rm F} \lesssim p_{\rm c} = 0.79$ fm where the simple effective range theory works.

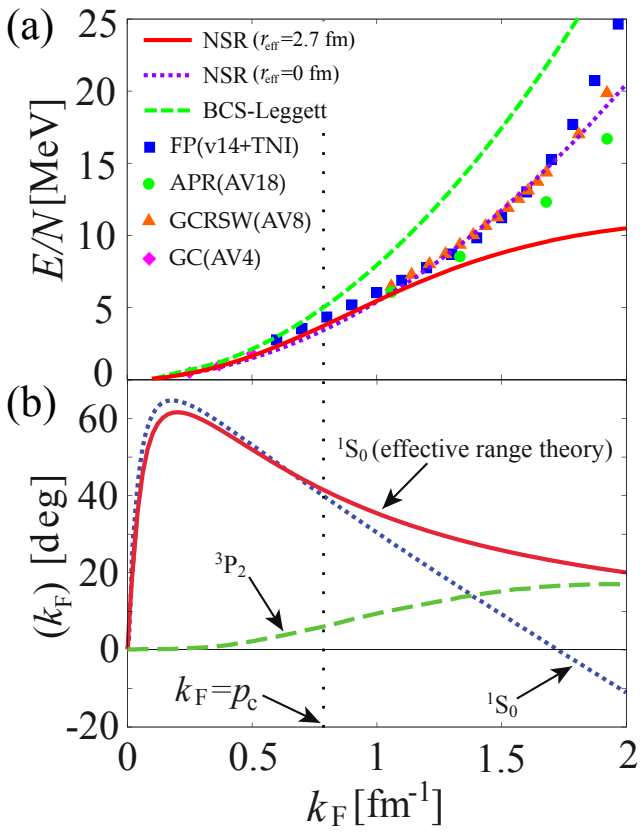

Figure 4.4: (a) Calculated neutron star equation of state (solid line), within the framework of the superfluid NSR theory with $a_s = -18.5$ fm and $r_{\rm eff} = 2.7$ fm. The dotted and dashed line show the results in the NSR theory with $r_{\rm eff} = 0$ fm, and BCS-Leggett theory with $r_{\rm eff} = 0$ fm, respectively. The solid squares [83], circles [84], diamonds [47], and triangles [85], show the results starting from various model interactions proposed in nuclear physics, with the name of the model being written in parentheses. (b) Neutron-neutron scattering phase shift $\delta(k_{\rm F})$. The solid line shows the phase shift in the present s-wave effective range theory. The dotted line shows the phase shift in the $^1{\rm S}_0$ channel [64, 98]. The vertical dotted line shows the position at the cutoff momentum $p_{\rm c} = 0.79$ fm^{-1}. In panel (b), we also show the phase shift in the $^3{\rm P}_2$ channel.

Regarding the above discussion, we note that the Hartree shift (the last term in Eq.(4.3)) largely increases the Fermi momentum $\tilde{p}_{\rm F} = \sqrt{2m\mu^*}$ (see the difference between μ and μ^* in Fig.4.3 (a)). This correction is crucial for the above-mentioned agreement of $E_{\rm gap}$ with the previous work. When μ is used instead of μ^* in Eq.(4.2) (when we ignore the correction from the Hartree shift) a smaller $\tilde{p}_{\rm F}$ gives a larger value of the threshold energy $E_{\rm gap}$ in Fig.4.3 (b).

Using the basic data set shown in Fig.4.3, we compute the neutron star equation of state (EOS) as a function of $k_{\rm F}$, as shown in Fig.4.4 (a). In the low-density region (where $k_{\rm F} \lesssim p_{\rm c}$), our combined NSR theory with the effective range theory agrees well with previous EOS results obtained in nuclear physics [47, 83–85]. As these previous results are based on pseudopotentials calibrated so as to reproduce nucleon scattering experiments it is difficult to ascertain to what extent *many-body effects* are included. Our results shown in Fig.4.4 (a), together with the results

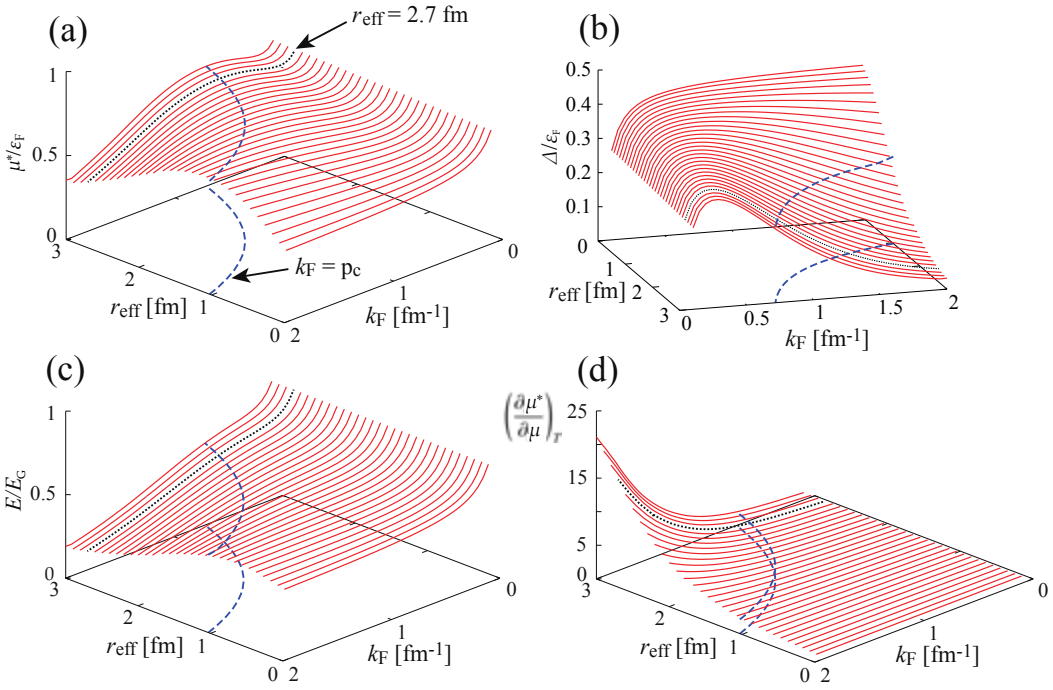

Figure 4.5: (a) Calculated effective chemical potential $\mu^* = \mu + U(a_s, r_{\rm eff})N_{\rm MF}/2$. (b) Superfluid order parameter Δ (c) Internal energy E. (d) Stoner factor $(\partial\mu^*/\partial\mu)_T$ in Eq. (2.91). We take $a_s = -18.5$ fm. The dashed line shows the result at $k_{\rm F} = p_{\rm c} = 0.79$ fm^{-1}. The dotted line shows the case of a neutron star ($r_{\rm eff} = 2.7$ fm).

presented in Sec 4.2, thus help to give experimental support in this regard. That is, although the inclusion of non-vanishing effective range ($r_{\rm eff} = 2.7$ fm) is still a theoretical challenge, the inclusion of strong-coupling corrections by the NSR scheme is fully supported by the recent experiment on a ^{6}Li superfluid Fermi gas, as shown in Fig.4.2.

We see in Fig.4.4 (a) that our EOS gradually deviates from previous results when $k_{\rm F} \gtrsim p_{\rm c}$. As mentioned previously, this is simply because the present simple effective range theory does no longer agrees with the phase shift in the ^{1}S$_0$ channel in this regime, as shown in Fig.4.4 (b). In addition, in the higher density region other partial wave channels (such as ^{3}P$_2$ shown in Fig.4.4 (b)), which are included in the previous results, should become important. Extending the present NSR approach to include these points is our exciting future problem. We briefly note that, because the conventional NSR theory with $r_{\rm eff} = 0$ also includes the above mentioned issues, the agreement with the previous work up to $k_{\rm F} = 2$ fm^{-1} seen in Fig.4.4 (a) is accidental.

4.3 Effects Of A Finite Effective Range On Thermodynamic Properties

We show in Fig.4.5 several physical quantities at various values of the effective range ($0 \le r_{\rm eff} \le 3$ fm). Although the present approach is valid for the low density region, $k_{\rm F} \lesssim p_{\rm c} = 0.79$ fm^{-1}, we also show the results in the region $k_{\rm F} \gtrsim p_{\rm c}$,

for reference. In panel (a), one sees that the effective chemical potential μ^* in Eq.(4.3) is not so sensitive to the effective range in the low density region ($k_{\rm F} \lesssim p_{\rm c}$). Since the Hartree shift $U(a_s, r_{\rm eff})N_{\rm MF}/2$ increases with increasing the value of $r_{\rm eff}$ (see Eq.(2.72)), this means that the effective range effects on the (bare) chemical potential μ are compensated by the Hartree shift to some extent. On the other hand, since Fermi particles near the Fermi surface are important for the Cooper-pair formation, the pairing is suppressed when the Fermi momentum $k_{\rm F}$ exceeds the cutoff momentum $k_{\rm c}$. Because of this, the superfluid order parameter Δ is sensitive to $r_{\rm eff}$ as seen in Fig.4.5 (b).

At a glance, the $r_{\rm eff}$-dependence of Δ shown in Fig.4.5 (b) makes us expect that the internal energy E is also sensitive to $r_{\rm eff}$, because of the $r_{\rm eff}$-dependence of the superfluid condensation energy (which is deeply related to Δ). However, the calculated internal energy E shown in panel (c) is actually not so sensitive to $r_{\rm eff}$ in the low density regime. This indicates that, although the loss of superfluid condensation energy by the suppression of Δ increases E, (at least compared to the NSR case for $r_{\rm eff} = 0$ fm). The Hartree energy term $-U(a_s, r_{\rm eff})N_{\rm MF}^2/2$ lowers E, which compensates the former effective range effect. Figure 4.4 (a) implies that such a compensation phenomenon occurs in the low density region, so that EOS is still comparable to that in the case when $r_{\rm eff} = 0$ fm when $k_{\rm F} \lesssim p_{\rm c}$. This indicates the importance of the Hartree-term, in quantitatively investigating EOS in the crust regime of a neutron star interior.

In Fig.4.5 (d), we show the Stoner factor $(\partial\mu^*/\partial\mu)_T$ associated with density fluctuations in Eq.(2.91). When the bare attraction interaction $U(a_s, r_{\rm eff})$ is non-zero density fluctuations are known to be enhanced by this interaction. However, although the Stoner enhancement really occurs ($(\partial\mu^*/\partial\mu)_T > 1$) in the present case, Fig.4.5 (d) shows that this enhancement is not so remarkable in the low density region ($k_{\rm F} \lesssim p_{\rm c}$). In this sense, density fluctuations are not so important in this region.

4.4 Correction From Density Fluctuations To The Equation Of State

The NSR theory is based on the assumption that pairing fluctuations (fluctuations in the Cooper channel) associated with a strong attractive interaction dominates over system properties. Regarding this assumption, Fig.4.5 (b) shows that the superfluid order is suppressed in the presence of a non-vanishing effective range, especially when $k_{\rm F} \gtrsim p_{\rm c}$. In addition, as mentioned previously, Figs.4.5 (a) and (c) imply the importance of the Hartree term when $r_{\rm eff} \neq 0$. Furthermore, the Stoner factor, associated with density fluctuations, appears in the NSR theory when $r_{\rm eff} \neq 0$, becomes large when $k_{\rm F} \gtrsim p_{\rm c}$ (see Fig.4.5) (d). These facts make us expect that other interaction channels, such as density fluctuations, may also become important in the case when the non-vanishing effective range exists, which the current NSR theory completely ignores.

Thus, although we can not include all the possible diagrams coming from $H_{\rm I}'$ in Eq.(2.77), in this section we evaluate all the second order diagrams that are ignored in the NSR theory. For this purpose we rewrite the interaction term $H_{\rm I}'$ in

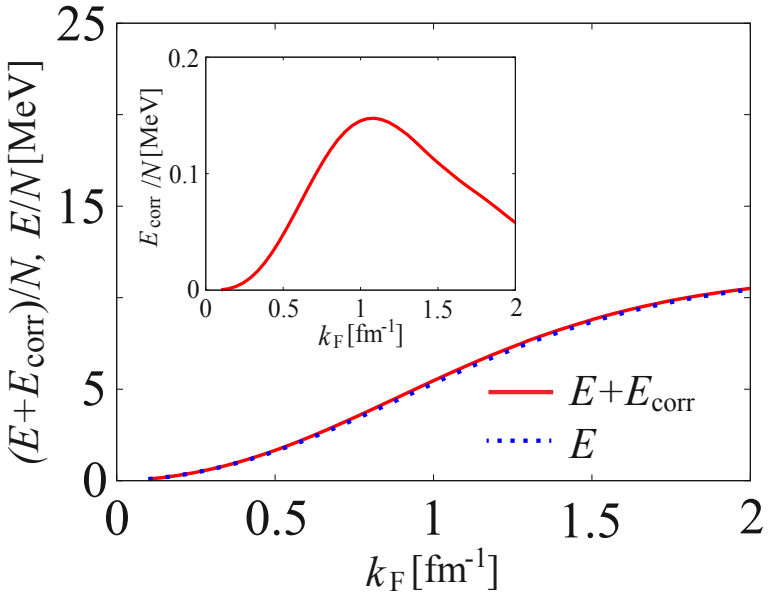

Figure 4.6: Effects of $E_{\rm corr}$ in Eq.(2.93) to the internal energy when $r_{\rm eff} = 2.7$ fm. The inset shows $E_{\rm corr}$.

Eq.(2.77) in the following two forms :

$$H'_{\rm I} = -U(a_s, r_{\rm eff}) \sum_{\boldsymbol{p},\boldsymbol{p}',\boldsymbol{q}} \gamma_{\boldsymbol{p}}\gamma_{\boldsymbol{p}'}\rho_+(\boldsymbol{p},\boldsymbol{q})\rho_-(\boldsymbol{p}',-\boldsymbol{q}), \tag{4.4}$$

$$H'_{\rm I} = -U(a_s, r_{\rm eff}) \sum_{\boldsymbol{p},\boldsymbol{p}',\boldsymbol{q}} \gamma_{(\boldsymbol{p}+\boldsymbol{p}'+\boldsymbol{q})/2}\gamma_{(\boldsymbol{p}+\boldsymbol{p}'-\boldsymbol{q})/2} n_+(\boldsymbol{p},\boldsymbol{q})n_-(\boldsymbol{p}',-\boldsymbol{q}). \tag{4.5}$$

These are convenient forms in considering superfluid fluctuations and density corrections, respectively. In Eq.(4.4) and Eq.(4.5), we have introduced

$$\rho_\pm(\boldsymbol{p},\boldsymbol{q}) = \frac{1}{2}\Psi^\dagger_{\boldsymbol{p}+\boldsymbol{q}/2}[\tau_1 \pm i\tau_2]\Psi_{\boldsymbol{p}-\boldsymbol{q}/2}, \tag{4.6}$$

$$n_\pm(\boldsymbol{p},\boldsymbol{q}) = \frac{1}{2}\Psi^\dagger_{\boldsymbol{p}+\boldsymbol{q}/2}[\tau_3 \pm \mathbf{1}]\Psi_{\boldsymbol{p}-\boldsymbol{q}/2}. \tag{4.7}$$

The second order correction $\Omega_{\rm corr}$ to the thermodynamic potential Ω in terms of $H'_{\rm I}$ is obtained from Eq.(2.12) as,

$$\Omega_{\rm corr} = -\frac{1}{2\beta}\int_0^\beta d\tau \int_0^\beta d\tau' \langle H'_{\rm I}(\tau)H'_{\rm I}(\tau')\rangle_{\rm c}. \tag{4.8}$$

Using Eq. (4.4) for both $H'_{\rm I}$'s in Eq. (4.8) results in contribution from the second-order diagram $\Omega^{(2)}_{\rm NSR}$ in Fig.2.7 (a), which has already been included in $\Omega_{\rm NSR}$ in Eq. (2.85).

Actually, $\Omega_{\rm NSR}$, may also be regarded as a contribution coming from fluctuations in the density channel. Indeed, when we choose Eq.(4.5) for both $H_{\rm I}$'s in Eq. (4.8), the second-order correction $\Omega^{(2)}_{\rm NSR}$ is again obtained. Since this contribution is already included in the NSR theory, we don't have to include this case here.

The correction that contributes to $\Omega_{\rm corr}$ is obtained, when we choose one $H_{\rm I}'$ as Eq. (4.4) and one as Eq. (4.5). This gives

$$\begin{aligned}\Omega_{\rm corr} &= -U(a_s, r_{\rm eff})^2 T \sum_{\boldsymbol{p},\boldsymbol{p}',\boldsymbol{q},\nu_n} \gamma_{(\boldsymbol{p}+\boldsymbol{p}'+\boldsymbol{q})/2}\gamma_{(\boldsymbol{p}+\boldsymbol{p}'-\boldsymbol{q})/2}\gamma_{\boldsymbol{p}}\gamma_{\boldsymbol{p}'} \\ &\times \left[\Pi^{\rho n}_{++}(\boldsymbol{p},\boldsymbol{q},i\nu_n)\Pi^{n\rho}_{--}(\boldsymbol{p}',-\boldsymbol{q},i\nu_n) + \Pi^{\rho n}_{+-}(\boldsymbol{p},\boldsymbol{q},i\nu_n)\Pi^{n\rho}_{+-}(\boldsymbol{p}',-\boldsymbol{q},i\nu_n)\right] \\ &= -2U(a_s, r_{\rm eff})^2 T \sum_{\boldsymbol{p},\boldsymbol{p}',\boldsymbol{q},\nu_n} \gamma_{(\boldsymbol{p}+\boldsymbol{p}'+\boldsymbol{q})/2}\gamma_{(\boldsymbol{p}+\boldsymbol{p}'-\boldsymbol{q})/2}\gamma_{\boldsymbol{p}}\gamma_{\boldsymbol{p}'} \\ &\times \Pi^{\rho n}_{++}(\boldsymbol{p},\boldsymbol{q},i\nu_n)\Pi^{\rho n}_{++}(\boldsymbol{p}',\boldsymbol{q},i\nu_n), \end{aligned} \tag{4.9}$$

where

$$\Pi^{\rho n}_{ij}(\boldsymbol{p},\boldsymbol{q},i\nu_n) = T\sum_{\nu_n} {\rm tr}\left[\tau_i \hat{G}(\boldsymbol{p}+\boldsymbol{q}/2, i\omega_n + i\nu_n) n_j \hat{G}(\boldsymbol{p}-\boldsymbol{q}/2, i\omega_n)\right], \tag{4.10}$$

$$\Pi^{n\rho}_{ij}(\boldsymbol{p},\boldsymbol{q},i\nu_n) = T\sum_{\nu_n} {\rm tr}\left[n_i \hat{G}(\boldsymbol{p}+\boldsymbol{q}/2, i\omega_n + i\nu_n) \tau_j \hat{G}(\boldsymbol{p}-\boldsymbol{q}/2, i\omega_n)\right]. \tag{4.11}$$

and we use the symmetry properties, $\Pi^{n\rho}_{--}(\boldsymbol{p},-\boldsymbol{q},i\nu_n) = \Pi^{\rho n}_{+-}(\boldsymbol{p},-\boldsymbol{q},i\nu_n) = \Pi^{\rho n}_{++}(\boldsymbol{p},\boldsymbol{q},i\nu_n)$, and $\Pi^{n\rho}_{+-}(\boldsymbol{p},\boldsymbol{q},i\nu_n)) = \Pi^{\rho n}_{++}(\boldsymbol{p},\boldsymbol{q},i\nu_n)$. These correlation functions physically describe couplings between superfluid and density fluctuations [20].

Summing up the Matsubara frequencies in $\Pi^{\rho n}_{++}$ in Eq.(4.9), gives

$$\begin{aligned}\Pi^{\rho n}_{++}(\boldsymbol{p},\boldsymbol{q},i\nu_n)) &= -\frac{\Delta_+}{4\tilde{E}_+}\left[\left(1+\frac{\tilde{\xi}_-}{\tilde{E}_-}\right)\left[\frac{1-n_{\rm F}(\tilde{E}_+)-n_{\rm F}(\tilde{E}_-)}{i\nu_n+\tilde{E}_++\tilde{E}_-} - \frac{n_{\rm F}(\tilde{E}_+)-n_{\rm F}(\tilde{E}_-)}{i\nu_n-\tilde{E}_++\tilde{E}_-}\right]\right. \\ &+ \left.\left(1-\frac{\tilde{\xi}_-}{\tilde{E}_-}\right)\left[\frac{1-n_{\rm F}(\tilde{E}_+)-n_{\rm F}(\tilde{E}_-)}{i\nu_n-\tilde{E}_+-\tilde{E}_-} - \frac{n_{\rm F}(\tilde{E}_+)-n_{\rm F}(\tilde{E}_-)}{i\nu_n+\tilde{E}_+-\tilde{E}_-}\right]\right] \end{aligned} \tag{4.12}$$

where $\Delta_\pm = \Delta_{\boldsymbol{p}\pm\boldsymbol{q}/2}$, $\tilde{\xi}_\pm = \tilde{\xi}_{\boldsymbol{p}\pm\boldsymbol{q}/2}$, and $\tilde{E}_\pm = \tilde{E}_{\boldsymbol{p}\pm\boldsymbol{q}/2}$.

Substituting Eq.(4.12) into Eq.(4.9), we obtain, after carrying out the ν_n-summation,

$$\begin{aligned}\Omega_{\rm corr} &= \frac{U(a_s, r_{\rm eff})^2}{4}\sum_{\boldsymbol{p},\boldsymbol{p}',\boldsymbol{q}}\left[1-\frac{\tilde{\xi}_{\boldsymbol{p}-\boldsymbol{q}/2}}{\tilde{E}_{\boldsymbol{p}-\boldsymbol{q}/2}}\right]\left[1-\frac{\tilde{\xi}_{\boldsymbol{p}'-\boldsymbol{q}/2}}{\tilde{E}_{\boldsymbol{p}'-\boldsymbol{q}/2}}\right] \\ &\times \frac{\gamma_{\boldsymbol{p}}\gamma_{\boldsymbol{p}'}\gamma_{(\boldsymbol{p}+\boldsymbol{p}'+\boldsymbol{q})/2}\gamma_{(\boldsymbol{p}+\boldsymbol{p}'-\boldsymbol{q})/2}\Delta_{\boldsymbol{p}+\boldsymbol{q}/2}\Delta_{\boldsymbol{p}'+\boldsymbol{q}/2}}{\tilde{E}_{\boldsymbol{p}+\boldsymbol{q}/2}\tilde{E}_{\boldsymbol{p}'+\boldsymbol{q}/2}\left[\tilde{E}_{\boldsymbol{p}+\boldsymbol{q}/2}+\tilde{E}_{\boldsymbol{p}-\boldsymbol{q}/2}+\tilde{E}_{\boldsymbol{p}'+\boldsymbol{q}/2}+\tilde{E}_{\boldsymbol{p}'-\boldsymbol{q}/2}\right]}. \end{aligned} \tag{4.13}$$

For simplicity, we have taken the zero-temperature limit in Eq.(4.13). The correction $E_{\rm corr}$ to the internal energy E, is then obtained from from Eq.(4.13) as

$$E_{\rm corr} = \Omega_{\rm corr} - T\left(\frac{\partial\Omega_{\rm corr}}{\partial T}\right)_\mu + \mu N_{\rm corr}, \tag{4.14}$$

where

$$N_{\rm corr} = -\left(\frac{\partial\mu^*}{\partial\mu}\right)_T\left(\frac{\partial\Omega_{\rm corr}}{\partial\mu^*.}\right)_T, \tag{4.15}$$

Fig.4.6 shows $E + E_{\rm corr}$ (we briefly note that we have resolved the gap equation Eq.(2.81), together with the number equation $N = N_{\rm MF} + N_{\rm NSR} + N_{\rm corr}$ including the correction term in Eq.(4.15)). The correction $E_{\rm corr}$ is found to be actually very small compared to the NSR internal energy E, at least in the low density region. Thus, the inclusion of superfluid fluctuations described by the diagrammatic series in Fig.2.7 (a) is considered to be effective in the low-density crust regime of a neutron star.

Chapter 5

Summary

To summarise, we have theoretically investigated effects of strong pairing fluctuations in the BCS-BEC crossover regime of an ultracold Fermi gas. Including fluctuations in the Cooper channel within the framework of the strong-coupling NSR (Nozières and Schmitt-Rink) theory [15], we examined how the specific heat at constant volume C_V is affected by pairing fluctuations in the whole BCS-BEC crossover regime in the normal and superfluid state. We have also discussed a possible approach of this highly tunable Fermi atomic system to the study of the equation of state (EOS) of a neutron star in the low density crust regime.

We found that the temperature dependence of the specific heat C_V is complicated and is sensitive to the strength of a pairing interaction in the normal state above T_c. Analysing the detailed behaviour of C_V, we succeeded in obtaining the characteristic temperatures $\tilde{T}$ and $\bar{T}$. Using these, we determine the region where system properties are dominated by pairing fluctuations, as well as the strong-coupling region where the system may be regarded as an almost ideal molecular Bose gas, in the phase diagram of an ultracold Fermi gas with respect to the temperature and interaction strength. From the comparison of these characteristic temperatures with the previous pseudo gap temperature T^* [22] and spin gap temperature T_s [24], we pointed out that the above-mentioned regime with strong pairing fluctuations corresponds to the so called pseudogap regime discussed recently [22, 44, 45].

We also compared the calculated C_V with the recent experiment in a ^{6}Li unitary Fermi gas [32]. Our result was shown to agree with the observed C_V in a semi quantitative level.

We further extended the superfluid NSR theory [20, 21] so that it can deal with the case with non-vanishing effective range $r_{\rm eff} \neq 0$. Combining this with the recent EOS experiment on a ^{6}Li superfluid Fermi gas in the BCS-unitarity regime [33], we have explored the possibility that an ultracold Fermi atomic gas can be used as a quantum simulator for the study of the EOS in the low density crust regime of a neutron star interior. After checking that the superfluid NSR theory can quantitatively explain the observed internal energy in the BCS-unitarity regime of a ^{6}Li superfluid Fermi gas, we employ the extended superfluid NSR theory with the realistic value $r_{\rm eff} = 2.7$ fm of the effective range of the neutron-neutron interaction, to evaluate the neutron star EOS. In the low density regime ($k_{\rm F} \lesssim 1$ fm^{-1}), our results agree well with the previous ones obtained in nuclear physics. We emphasise that, in our approach, inclusion of many-body effects are fully supported

by the recent EOS experiment in cold Fermi gas physics, except for effects of the non-vanishing effective range. This is quite different from the previous work, where such experimental support is up to construction of few body interactions, and inclusion of many-body effects is a fully experimental challenge. Our result indicates that an ultracold Fermi atom gas may be used as a quantum simulator for the study of other systems in a more flexible manner than the current approach (where perfect replication of a target system is attempted), when the difference between the Fermi gas system and target system is made up for by using a reliable strong-coupling BCS-BEC crossover theory.

Since humanity does not currently possess the technology to directly measure the neutron star EOS, our idea for using the thermodynamic properties of a strongly interacting Fermi gas along with strong coupling theory provides a novel route, in addition to astrophysical observations and nuclear physics, in studying this mysterious object.

In this thesis, we have restricted our theoretical approach to the NSR level. Inclusion of higher-order pairing fluctuations beyond this scheme would be an important future problem, in order to obtain more quantitative agreement with the observed specific heat in the normal state of a ^{6}Li unitary Fermi gas near T_c. For this purpose, inclusion of spacial inhomogeneity coming from the trapping geometry would also be important. In addition, we have only dealt with the case of an s-wave pairing interaction. Since a tunable p-wave interaction associated with a p-wave Feshbach resonance has been realised in ultracold Fermi gasses [7, 35, 36, 41], it is also an interesting future problem to explore the possibility that this p-wave interacting Fermi gas is usefull to study the deeper region of a neutron star interior.

Since understanding strong coupling properties of an ultracold Fermi gas in the BCS-BEC crossover region is a crucial issue for, not only the development of cold Fermi gas physics, but also various complicated many-body systems that are waiting for a quantum simulator, our results would contribute to the future of various research fields.

Acknowledgments

First and foremost I would like to give thanks to professor Yoji Ohashi. His kind guidance, advice and teaching helped me realise I still have a long way to go, but have also made me enthusiastic about the journey ahead. I am grateful for the research environment he has provided, which has allowed me to concentrate on my work without restrictions. I thank him also for being strict when the time called for it, and pushing me to go beyond what I think I could possibly achieve in these 5 short years. His guidance always displayed a true passion for physics, and the education of the students in his lab.

I am also extremely grateful to professor Masanori Matoba, professor Shinichi Watanabe, and professor Jun Yamauchi for reading my thesis and for their kind advice through my PhD examination process.

I would like to thank Dr. Daisuke Inotani for the multitude of invaluable advice he gave me concerning my research, and to Dr. Tajima Hiroyuki for being an example every graduate student should strive for. I am also grateful to my other lab mates (previous and present) Ryo Hanai, Morio Matsumoto, Daichi Kagamihara, Miki Ota, Digvijay Khagra, Soumita Mondal, Manabe Koki and Sato Ryohei who helped to make the Ohashi group laboratory a fruitful research environment.

I would like to give special thanks to professor Akira Ohnishi for his kind guidance and advice concerning the second part of my thesis.
Finally, I cannot say thank you enough to my mother and father, Sandra and Pieter Roelof van Wyk, for teaching me the value of diligence and hard work. Without their love and support I would not be where I am today.

Appendix A

Proton Fraction In Non-Interacting Nuclear Matter

In this appendix, we evaluate the neutron population from the beta-equilibrium condition in Eq.(1.9), together with charge neutrality. Considering Eq.(1.9) (where the Fermi chemical potential is given in Eq.(1.10)), we find.

$$\begin{aligned}\sqrt{m_n^2c^4 + p_{\mathrm{F}n}^2c^2} &= \sqrt{m_p^2c^4 + p_{\mathrm{F}p}^2c^2} + \sqrt{m_e^2c^4 + p_{\mathrm{F}e}^2c^2} \\ &\simeq \sqrt{m_n^2c^4 + p_{\mathrm{F}p}^2c^2} + \sqrt{(\beta m_n)^2\,c^4 + p_{\mathrm{F}p}^2c^2}, \end{aligned} \tag{A.1}$$

where we assumed charge neutrality $p_{\mathrm{F}p} = p_{\mathrm{F}e}$, and $m_n \simeq m_p$, $m_e \simeq \beta m_p$, where $\beta = 1/1836.12$ [99].

Using $p_{\mathrm{F}i} = \hbar\left(3\pi^2 n_i\right)^{1/3}$ $(i = n, p)$ and defining the proton fraction $Y_p = n_p/n_n$, we can rewrite Eq.(A.1) as

$$\sqrt{1 + \alpha\bar{n}_n^{2/3}} = \sqrt{1 + \alpha\bar{n}_n {Y_p}^{2/3}} + \sqrt{\beta^2 + \alpha\bar{n}_n {Y_p}^{2/3}}. \tag{A.2}$$

In Eq.(A.2) $\bar{n}_n = n_n/n_0$, with $n_0 = 0.16\mathrm{fm}^{-3}$ being the nuclear saturation density [61], and we have defined

$$\alpha = \frac{\hbar^2\left(3\pi^2 n_0\right)^{3/2}}{m_n^2c^2} = 0.124 \tag{A.3}$$

(using $\hbar c = 197$ MeV fm and $m_n = 939$ MeV/c^2).

The total mass density is given by

$$\begin{aligned}\rho &= m_n n_n + m_p n_p + m_e n_e \\ &= \left(1 + (1+\beta)\,Y_p\right) m_n n_n. \end{aligned} \tag{A.4}$$

Normalising Eq.(A.4) in terms of the the neutron mass density $\rho_0 = m_n n_0$ at the nuclear saturation density, and substituting into Eq.(A.2), we have

$$\begin{aligned}\sqrt{1 + \alpha\left[\frac{\bar{\rho}}{1 + (1+\beta)\,Y_p}\right]^{2/3}} &= \sqrt{1 + \alpha\left[\frac{\bar{\rho}Y_p}{1 + (1+\beta)\,Y_p}\right]^{2/3}} \\ &+ \sqrt{\beta^2 + \alpha\left[\frac{\bar{\rho}Y_p}{1 + (1+\beta)\,Y_p}\right]^{2/3}}, \end{aligned} \tag{A.5}$$

where $\bar{\rho} = \rho/\rho_0$. Equation (A.5) is a self-consistent equation for the proton fraction Y_p for a given $\bar{\rho}$. The solution of Eq.(A.5) is shown in Fig.1.11. In the high density limit ($\bar{\rho} \gg 1$) Eq.(A.5) gives $Y_p = 1/8$.

Appendix B

Derivation Of Eq.(2.57) And Eq.(2.60)

To derive Eq.(2.57) and Eq.(2.60) from the gap-equation Eq.(2.54) , we conveniently define

$$g\left(T,\mu,\Delta\right)=\sum_{\boldsymbol{p}}\left[\frac{1}{2E_{\boldsymbol{p}}}\tanh\frac{E_{\boldsymbol{p}}}{2T}-\frac{1}{2\varepsilon_{\boldsymbol{p}}}\right]. \tag{B.1}$$

We note that $g\left(T,\mu,\Delta\right)=1$ when Δ and μ satisfy the gap equation (2.54). In such a case, one finds

$$0=\left(\frac{\partial g}{\partial\mu}\right)_{T}=\left(\frac{\partial g}{\partial\mu}\right)_{\Delta,T}+\left(\frac{\partial\Delta}{\partial\mu}\right)_{T}\left(\frac{\partial g}{\partial\Delta}\right)_{\mu,T} \tag{B.2}$$

when Eq.(2.54) is satisfied.

Here, Eq.(B.1) gives

$$\begin{aligned}\left(\frac{\partial g}{\partial\mu}\right)_{\Delta,T} &= -\sum_{\boldsymbol{p}}\frac{\xi_{\boldsymbol{p}}}{2E_{\boldsymbol{p}}^{2}}\left[\frac{1}{2T}\mathrm{sech}^{2}\left(\frac{E_{\boldsymbol{p}}}{2T}\right)-\frac{1}{E_{\boldsymbol{p}}}\tanh\left(\frac{E_{\boldsymbol{p}}}{2T}\right)\right],\\ \left(\frac{\partial g}{\partial\Delta}\right)_{\mu,T} &= \sum_{\boldsymbol{p}}\frac{\Delta}{2E_{\boldsymbol{p}}^{2}}\left[\frac{1}{2T}\mathrm{sech}^{2}\left(\frac{E_{\boldsymbol{p}}}{2T}\right)-\frac{1}{E_{\boldsymbol{p}}}\tanh\left(\frac{E_{\boldsymbol{p}}}{2T}\right)\right].\end{aligned} \tag{B.3}$$

Substituting Eq.(B.3) into Eq.(B.2), we obtain

$$\begin{aligned}\left(\frac{\partial\Delta}{\partial\mu}\right)_{T} &= -\frac{\left(\frac{\partial g}{\partial\mu}\right)_{\Delta,T}}{\left(\frac{\partial g}{\partial\Delta}\right)_{\mu,T}}\\ &= \frac{\sum_{\boldsymbol{p}}\frac{\xi_{\boldsymbol{p}}}{E_{\boldsymbol{p}}^{2}}\left[\frac{1}{2T}\mathrm{sech}^{2}\left(\frac{E_{\boldsymbol{p}}}{2T}\right)-\frac{1}{E_{\boldsymbol{p}}}\tanh\left(\frac{E_{\boldsymbol{p}}}{2T}\right)\right]}{\sum_{\boldsymbol{p}}\frac{\Delta}{E_{\boldsymbol{p}}^{2}}\left[\frac{1}{2T}\mathrm{sech}^{2}\left(\frac{E_{\boldsymbol{p}}}{2T}\right)-\frac{1}{E_{\boldsymbol{p}}}\tanh\left(\frac{E_{\boldsymbol{p}}}{2T}\right)\right]}.\end{aligned} \tag{B.4}$$

Similarly, taking the derivative of Eq.(B.1) with respect to T while keeping the chemical potential μ fixed,

$$0=\left(\frac{\partial g}{\partial T}\right)_{\mu}=\left(\frac{\partial g}{\partial T}\right)_{\Delta,\mu}+\left(\frac{\partial\Delta}{\partial T}\right)_{\mu}\left(\frac{\partial g}{\partial\Delta}\right)_{\mu,T}. \tag{B.5}$$

Using Eq.(B.3) and

$$\left(\frac{\partial g}{\partial T}\right)_{\mu,\Delta} = -\sum_{\boldsymbol{p}} \frac{1}{4T^2}\mathrm{sech}^2\left(\frac{E_{\boldsymbol{p}}}{2T}\right) \tag{B.6}$$

one reaches

$$\begin{aligned}\left(\frac{\partial \Delta}{\partial T}\right)_{\mu} &= -\frac{\left(\frac{\partial g}{\partial T}\right)_{\Delta,\mu}}{\left(\frac{\partial g}{\partial \Delta}\right)_{\mu,T}} \\ &= \frac{\sum_{\boldsymbol{p}} \frac{1}{2T^2}\mathrm{sech}^2\left(\frac{E_{\boldsymbol{p}}}{2T}\right)}{\sum_{\boldsymbol{p}} \frac{\Delta}{E_{\boldsymbol{p}}^2}\left[\frac{1}{2T}\mathrm{sech}^2\left(\frac{E_{\boldsymbol{p}}}{2T}\right) - \frac{1}{E_{\boldsymbol{p}}}\tanh\left(\frac{E_{\boldsymbol{p}}}{2T}\right)\right]}.\end{aligned} \tag{B.7}$$

Appendix C

Derivation Of Eq.(2.71)

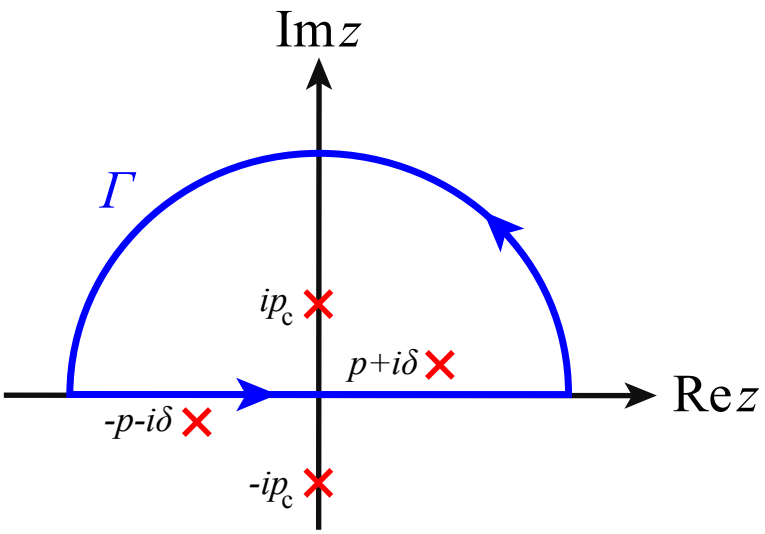

Figure C.1: Integral contour Γ in Eq.(C.2). Four poles of the integrant are also shown (red ×).

To derive the expression for the momentum cutoff p_c in Eq.(2.71) in the effective range theory, we introduce the function,

$$\begin{aligned} I_p &= \frac{4\pi}{m}\sum_{p'}\gamma_{p'}^2\left[\frac{1}{2\varepsilon_{p'}-(2\varepsilon_p+i\delta)}-\frac{1}{2\varepsilon_{p'}}\right] \\ &= \frac{2p_c^2}{\pi}\int_0^\infty \mathrm{d}p'\,\frac{p'^2}{p'^2+p_c^2}\left[\frac{1}{p'^2-p^2-i\delta}-\frac{1}{p'^2}\right], \end{aligned} \tag{C.1}$$

where we have redefined $m\delta \to \delta$ in obtaining the second line.

To evaluate Eq.(C.1), we also introduce the complex integral,

$$\begin{aligned} I_\Gamma &= \frac{1}{2}\int_\Gamma \mathrm{d}z\frac{z^2}{z^2+p_c^2}\frac{1}{z^2-p^2-i\delta} \\ &= \frac{1}{2}\int_\Gamma \mathrm{d}z\frac{z^2}{(z+ip_c)(z-ip_c)(z+[p+i\delta])(z-[p+i\delta])}, \end{aligned} \tag{C.2}$$

where the path Γ is given in Fig.C.1. Evaluating the residues at the poles $z = ip_c$

and $z = p + i\delta$, one has

$$I_\Gamma = \frac{\pi}{2}\left[\frac{p_c}{p^2 + p_c^2} + \frac{ip}{p^2 + p_c^2}\right]. \tag{C.3}$$

Taking the radius of the contour to infinity, we reach

$$\begin{aligned} I_{\boldsymbol{p}} &= \frac{2p_c^2}{\pi}\left[I_\Gamma - \frac{\pi}{2p_c}\right] \\ &= p_c\left(\gamma_{\boldsymbol{p}}^2 - 1\right) + ip\gamma_{\boldsymbol{p}}^2. \end{aligned} \tag{C.4}$$

Using this, we can evaluate the momentum summation in the denominator in Eq.(2.69) when the basis function $\gamma_{\boldsymbol{p}}$ in Eq.(2.70) is used, which gives Eq.(2.71).

Bibliography

[1] W. Ketterle, D.S. Durfee, D.M. Stamper-Kurn, *Making, probing and understanding Bose-Einstein condensates* in Bose-Einstein Condensation in Atomic Gases (Proceedings of the International School of Physics), (IOS Press, Amsterdam, 1999).

[2] X. -G. Wen *Quantum Field Theory of Many-Body Systems*, (Oxford University Press, New York, 2004).

[3] W. Ketterle, and M. W. Zwierlein, *Ultracold Fermi Gases*, edited by M. Inguscio, W. Ketterle, and C. Salomon (IOS Press, Amsterdam, 2008).

[4] I. Bloch, J. Dalibard, and W. Zwerger, *Many-body physics with ultracold gases*, Rev. Mod. Phys. **80**, 885 (2008).

[5] I. Bloch, J. Dalibard, and S. Nascimbène, *Quantum simulations with ultracold quantum gases*, Nature Phys. **8**, 267 (2012).

[6] C. Chin, R. Grimm, P. Julienne, and E. Tiesinga, *Feshbach resonances in ultracold gases*, Rev. Mod. Phys. **82**, 1225 (2010).

[7] C. A. Regal, C. Ticknor, J. L. Bohn, and D. S. Jin, *Creation of ultracold molecules from a Fermi gas of atoms*, Nature **424**, 47 (2003).

[8] C. A. Regal, and D. S. Jin, *Measurement of Positive and Negative Scattering Lengths in a Fermi Gas of Atoms*, Phys. Rev. Lett. **90**, 230404 (2003).

[9] C. A. Regal, M. Greiner, and D. S. Jin, *Observation of Resonance Condensation of Fermionic Atom Pairs*, Phys. Rev. Lett. **92**, 040403 (2004).

[10] M. W. Zwierlein, C. A. Stan, C. H. Schunck, S. M. F. Raupach, A. J. Kerman, and W. Ketterle, *Condensation of Pairs of Fermionic Atoms near a Feshbach Resonance*, Phys. Rev. Lett. **92**, 120403 (2004).

[11] J. Kinast, S. L. Hemmer, M. E. Gehm, A. Turlapov, and J. E. Thomas, *Evidence for Superfluidity in a Resonantly Interacting Fermi Gas*, Phys. Rev. Lett. **92**, 150402 (2004).

[12] M. Bartenstein, A. Altmeyer, S. Riedl, S. Jochim, C. Chin, J. H. Denschlag, and R. Grimm, *Collective Excitations of a Degenerate Gas at the BEC-BCS Crossover*, Phys. Rev. Lett **92**, 203201 (2004).

[13] D. M. Eagles, *Possible Pairing without Superconductivity at Low Carrier Concentrations in Bulk and Thin-Film Superconducting Semiconductors*, Phys. Rev. **186**, 456 (1969).

[14] A. J. Leggett, in *Modern Trends in the Theory of Condensed Matter*, edited by A. Pekalski and J. Przystawa, (Springer-Verlag, Berlin, 1980).

[15] P. Nozières and S. Schmitt-Rink, *Bose condensation in an attractive fermion gas: From weak to strong coupling superconductivity*, J. Low Temp. Phys. **59**, 195 (1985).

[16] C. A. R. Sá de Melo, M. Randeria, and R. Engelbrecht, *Crossover from BCS to Bose superconductivity: Transition temperature and time-dependent Ginzburg-Landau theory*, Phys. Rev. Lett. **71**, 3202 (1993).

[17] A. Perali, P. Pieri, G. C. Strinati, and C. Castellani, *Pseudogap and spectral function from superconducting fluctuations to the bosonic limit*, Phys. Rev. B **66**, 024510 (2002).

[18] A. Perali, F. Palestini, P. Pieri, G. C. Strinati, J. T. Stewart, J. P. Gaebler, T. E. Drake, and D. S. Jin, *Evolution of the Normal State of a Strongly Interacting Fermi Gas from a Pseudogap Phase to a Molecular Bose Gas*, Phys. Rev. Lett. **106**, 060402 (2011).

[19] Y. Ohashi and A. Griffin, *BCS-BEC Crossover in a Gas of Fermi Atoms with a Feshbach Resonance*, Phys. Rev. Lett. **89**, 130402 (2002).

[20] Y. Ohashi and A. Griffin, *Superfluidity and collective modes in a uniform gas of Fermi atoms with a Feshbach resonance*, Phys. Rev. A **67**, 063612 (2003).

[21] N. Fukushima, Y. Ohashi, E. Taylor and A. Griffin, *Pairing fluctuations and the superfluid density through the BCS-BEC crossover*, Phys. Rev. A **75**, 033609 (2007).

[22] S. Tsuchiya, R. Watanabe, and Y. Ohashi, *Single-particle properties and pseudogap effects in the BCS-BEC crossover regime of an ultracold Fermi gas above T_c*, Phys. Rev. A **80**, 033613 (2009).

[23] S. Tsuchiya, R. Watanabe, and Y. Ohashi, *Pseudogap temperature and effects of a harmonic trap in the BCS-BEC crossover regime of an ultracold Fermi gas*, Phys. Rev. A **84**, 043647 (2011).

[24] H. Tajima, T. Kashimura, R. Hanai, R. Watanabe, and Y. Ohashi, *Uniform spin susceptibility and spin-gap phenomenon in the BCS-BEC-crossover regime of an ultracold Fermi gas*, Phys. Rev. A **89**, 033617 (2014).

[25] J. T. Stewart, J. P. Gaebler, and D. S. Jin, *Using photoemission spectroscopy to probe a strongly interacting Fermi gas*, Nature **454**, 744 (2008).

[26] J. P. Gaebler, J. T. Stewart, T. E. Drake, D. S. Jin, A. Perali, P. Pieri, and G. C. Strinati, *Observation of pseudogap behaviour in a strongly interacting Fermi gas*, Nature Phys. **6**, 569 (2010).

[27] S. Nascimbène, N. Navon, K. J. Jiang, F. Chevy, and C. Salomon, *Exploring the thermodynamics of a universal Fermi gas*, Nature, **463**, 1057 (2010).

[28] C. A. R. Sa de Melo, M. Randeria, and J. R. Engelbrecht, *Crossover from BCS to Bose superconductivity: Transition temperature and time-dependent Ginzburg-Landau theory*, Phys. Rev. Lett, **71**, 3202 (1993).

[29] R. Haussmann, W. Rantner, S. Cerrito and W. Zwerger, *Thermodynamics of the BCS-BEC crossover*, Phys. Rev. A **75**, 023610 (2007).

[30] S. Giorgini, L. P. Pitaevskii, and S. Stringari, *Theory of ultracold atomic Fermi gases*, Rev. Mod. Phys. **80**, 1215 (2008).

[31] I. M. Georgescu, S. Ashhab, F .Nori, *Quantum simulation*, Rev. Mod. Phys. **86**, 153 (2014).

[32] M. J. H. Ku, A. T. Sommer, L. W. Cheuk, and M. W. Zwierlein, *Revealing the Superfluid Lambda Transition in the Universal Thermodynamics of a Unitary Fermi Gas*, Science **335**, 563 (2012).

[33] M. Horikoshi, M. Koashi, H. Tajima, Y. Ohashi, and M. Kuwata-Gonokami, *Ground-State Thermodynamic Quantities of Homogeneous Spin*$-1/2$ *Fermions from the BCS Region to the Unitarity Limit*, Phys. Rev. X **7**, 041004 (2017).

[34] T. L. Ho, and R. B. Diener, *Fermion Superfluids of Nonzero Orbital Angular Momentum near Resonance*, Phys. Rev. Lett. **94**, 090402 (2005).

[35] C. Ticknor, C. A. Regal, D. S. Jin, and J. L. Bohn, *Multiplet structure of Feshbach resonances in nonzero partial waves*, Phys. Rev. A **69**, 042712 (2004).

[36] J. Zhang, E. G. M. van Kempen, T. Bourdel, L. Khaykovich, J. Cubizolles, F. Chevy, M. Teichmann, L. Tarruell, S. J. J. M. F. Kokkelmans, and C. Salomon, *P-wave Feshbach resonances of ultracold* ^{6}*Li*, Phys. Rev. A **70**, 030702(R) (2004).

[37] F. Chevy, E. G. M. van Kempen, T. Bourdel, J. Zhang, L. Khaykovich, M. Teichmann, L. Tarruell, S. J. J. M. F. Kokkelmans, and C. Salomon, *Resonant scattering properties close to a p-wave Feshbach resonance*, Phys. Rev. A **71**, 062710 (2005).

[38] J. P. Gaebler, J. T. Stewart, J. L. Bohn, and D. S. Jin, *p-Wave Feshbach Molecules*, Phys. Rev. Lett. **98**, 200403 (2007).

[39] M. Jona-Lasinio, L. Pricoupenko, and Y. Castin, *Three Resonant Ultracold Bosons: Off-Resonance Effects*, Phys. Rev. A **77**, 043611 (2008).

[40] J. Levinsen, N. R. Cooper, and V. Gurarie, *Stability of fermionic gases close to a p-wave Feshbach resonance*, Phys. Rev. A **78**, 063616 (2008).

[41] T. Nakasuji, J. Yoshida, and T. Mukaiyama, *Experimental determination of p-wave scattering parameters in ultracold* ^{6}*Li atoms*, Phys. Rev. A **88**, 012710 (2013).

[42] T. Lahaye, J. Metz, B. Fröhlich, T. Koch, M. Meister, A. Griesmaier, T. Pfau, H. Saito, Y. Kawaguchi, and M. Ueda, *d-Wave Collapse and Explosion of a Dipolar Bose-Einstein Condensate*, Phys. Rev. Lett. **101**, 080401 (2008).

[43] P. A. Lee, N. Nagaosa, X. -G. Wen, *Doping a Mott insulator: Physics of high-temperature superconductivity*, Rev. Mod. Phys, **78**, 87 (2006).

[44] Q. J. Chen, J. Stajic, S. N. Tan, and K. Levin, *BCS-BEC Crossover: From High Temperature Superconductors to Ultracold Superfluids*, Phys. Rep. **412**, 1 (2005).

[45] Q. J. Chen, and K. Levin, *Applying BCS-BEC crossover theory to high-temperature superconductors and ultracold atomic Fermi gases*, Low Temp. Phys. **32**, 406 (2006).

[46] J. Margueron, H. Sagawa, and K. Hagino, *BCS-BEC crossover of neutron pairs in symmetric and asymmetric nuclear matter*, Phys. Rev. C **76**, 064316 (2007).

[47] A. Gezerlis and J. Carlson, *Strongly paired fermions: Cold atoms and neutron matter*, Phys. Rev. C **77**, 032801(R) (2008).

[48] A. Gezerlis and J. Carlsos, *Low-density neutron matter*, Phys. Rev. C **81**, 025803 (2010).

[49] A. Gezerlis, and J. Carlson, *Terrestrial and Astrophysical Superfluidity: Cold Atoms and Neutron Matter*, arXiv:1109.4946 (2011).

[50] S. Mao, X. -G. Huang, and P. Zhuang, *BCS-BEC crossover and thermodynamics in asymmetric nuclear matter with pairings in isospin $I = 0$ and $I = 1$ channels*, Phys. Rev. C **79**, 034304 (2009)

[51] X. -G. Huang, *BCS-BEC crossover in symmetric nuclear matter at finite temperature: Pairing fluctuation and pseudogap*, Phys. Rev. C **81**, 034007 (2010)

[52] M. Stein, X. -G. Huang, A. Sedrakian, and J. W. Clark, *Phase diagram of dilute nuclear matter: Unconventional pairing and the BCS-BEC crossover*, Phys. Rev. C **86**, 062801(R) (2012).

[53] M. Stein, A. Sedrakian, X. -G. Huang, and J. W. Clark, *BCS-BEC crossovers and unconventional phases in dilute nuclear matter*, Phys. Rev. C **90**, 065804 (2014).

[54] S. Ramanan and M. Urban, *BEC-BCS crossover in neutron matter with renormalization-group-based effective interactions*, Phys. Rev. C. **88**, 054315 (2013).

[55] S. Wolf, A. Vagov, A. A. Shanenko, V. M. Axt, A. Perali, and J. Albino Aguiar, *BCS-BEC crossover induced by a shallow band: Pushing standard superconductivity types apart*, Phys. Rev. B **95**, 094521 (2017).

[56] S. Kasahara, T. Watashige, T. Hanaguri, Y. Kohsaka, T. Yamashita, Y. Shimoyama, Y. Mizukami, R. Endo, H. Ikeda, K. Aoyama, T. Terashima, S. Uji, T. Wolf, H. von Lohneysen, T. Shibauchi, and Yuji Matsuda, *Field-induced superconducting phase of FeSe in the BCS-BEC cross-over*, PNAS **111**, 16309 (2014).

[57] G. F. Giuliani, G. Vignale, *Quantum Theory of the Electron Liquid* (Cambridge University Press, New York, 2005).

[58] N. E. Phillips, *Heat Capacity of Aluminum between* 0.1°K *and* 4.0°K, Phys. Rev. **114**, 676 (1959).

[59] H. H. Wen, G. Mu, H. Luo, H. Yang, L. Shan, C. Ren, P. Cheng, J. Yan, L. Fang, *Specific-Heat Measurement of a Residual Superconducting State in the Normal State of Underdoped* $Bi_2Sr_{2-x}La_xCuO_{6+\delta}$ *Cuprate Superconductors*, Phys. Rev. Lett. **103**, 067002 (2009).

[60] P. Reif, *Fundamentals of Statistical and Thermal Physics*, (Waveland Press, Illinois, 2008).

[61] H. Heiselberg, V. Pandharipande, *Recent Progress in Neutron Star Theory*, Annu. Rev. Nucl. Part. Sci. **50**, 481 (2000).

[62] A. Reisengger, and F. S. Zepeda, *Order-of-magnitude physics of neutron stars*, arXiv:1511.08813 (2015).

[63] S. L. Shapiro, S. A. Teukolsky, *Black Holes, White Dwarfs and Neutron Stars: The Physics of Compact Objects* (Wiley-VCH, Weinheim,1983).

[64] D. J. Dean and M. Hjorth-Jensen, *Pairing in nuclear systems: from neutron stars to finite nuclei*, Rev. Mod. Phys. **75**, 607 (2003).

[65] W. D. Newton, *Neutron stars: A taste of pasta?*, Nature Phys. **9**, 369 (2013).

[66] V. G. J. Stoks, R. A. M. Klomp, M. C. M. Rentmeester, and J. J. de Swart, *Partial-wave analysis of all nucleon-nucleon scattering data below 350 MeV*, Phys. Rev. C **48**, 792 (1993).

[67] I. Slaus, Y. Akaishi, H. Tanaka, *Neutron-neutron effective range parameters*, Phys. Rep. **173**, 257 (1989).

[68] J. R. Taylor, in *Scattering Theory* (Dover, NY, 2006).

[69] H. A. Bethe, *Theory of the Effective Range in Nuclear Scattering*, Phys. Rev. **76**, 38 (1949).

[70] P. B. Demorest, T. Pennucci, S. M. Ransom, M. S. E. Roberts, and J. W. T. Hessels, *A two-solar-mass neutron star measured using Shapiro delay*, Nature **467**, 1081 (2010).

[71] J. Antoniadis, P. C. C. Feire, N. Wex, T. M. Tauris, R. S. Lynch, M. H. van Kerkwijk, M. Kramer, C. Bassa, V. S. Dhillon, T. Driebe, J. W. T. Hessels, V. M. Kapsi, V. I. Kondratiev, N. Langer, T. R. Marsh, M. A. McLaughlin, T. T. Pennucci, S. M. Ransom, I. H. Stairs, J. van Leeuwen, J. P. W. Vierbiest, D. G. Whelan, *A Massive Pulsar in a Compact Relativistic Binary* , Science **340**, 448 (2013).

[72] J. M . Lattimer, and M. Parkash, *Neutron Star Structure and the Equation of State*, Astrophys. J. **550**,426 (2001).

[73] T. Takatsuka, *Hyperon-Mixed Neutron Stars*, Prog. Theor. Phys. Suppl. **156**, 84 (2004).

[74] D. Lonardoni, A. Lovato, S. Gandolfi, and F. Pederiva, *Hyperon Puzzle: Hints from Quantum Monte Carlo Calculations*, Phys. Rev. Lett. **114**, 092301 (2015).

[75] R. C. Tolman, *Static Solutions of Einstein's Field Equations for Spheres of Fluid*, Phys. Rev. **55**, 364 (1939).

[76] J. R. Oppenheimer, and G. M. Volkoff, *On Massive Neutron Cores*, Phys. Rev. **55**, 374 (1939).

[77] R. R. Silbara, and S. Reddyb, *Neutron stars for undergraduates*, Am. J. Phys. **72**, 892 (2004).

[78] N. Sartore, A. Tiengo, S. Mereghetti, A. De Luca, R. Turolla, and F. Haberl, *Spectral monitoring of RX J1856.5-3754 with XMM-Newton Analysis of EPIC-pn data*, Astronomy & Astrophysics, **541**, A66 (2012).

[79] K. Riisager, *Nuclear halo states*, Rev. Mod. Phys. **66**, 1105 (1994).

[80] Y. Togano, T. Nakamura, Y. Kondo, J. A. Tostevin, A. T. Saito, J. Gibelin, N. A. Orr, N. L. Achouri, T. Aumannd, H. Babae, F. Delaunay, P. Doornenbal, N. Fukuda, J. W. Hwang, N. Inabe, T. Isobe, D. Kameda, D. Kanno, S. Kim, N. Kobayashi, T. Kobayashi, T. Kubo, S. Leblond, J. Lee, F. M. Marques, R. Minakata, T. Motobayashi, D. Murai, T. Murakami, K. Muto, T. Nakashima, N. Nakatsuka, A. Navin, S. Nishi, S. Ogoshi, H. Otsu, H. Sato, Y. Satou, Y. Shimizu, H. Suzuki, K. Takahashi, H. Takeda, S. Takeuchi, R. Tanaka, A. G. Tuff, M. Vandebrouck, K. Yoneda, *Interaction cross section study of the two-neutron halo nucleus* ^{2}2C, Phys. Lett. B **761**, 412 (2016).

[81] A. Tamii, I. Poltoratska, P. von Neumann-Cosel, Y. Fujita, T. Adachi, C.A. Bertulani, J. Carter, M. Dozono, H. Fujita, K. Fujita, K. Hatanaka, D. Ishikawa, M. Itoh, T. Kawabata, Y. Kalmykov, A. M. Krumbholz, E. Litvinova, H. Matsubara, K. Nakanishi, R. Neveling, H. Okamura, H. J. Ong, B. Ożel-Tashenov, V. Yu. Ponomarev, A. Richter, B. Rubio, H. Sakaguchi, Y. Sakemi, Y. Sasamoto, Y. Shimbara, Y. Shimizu, F. D. Smit, T. Suzuki, Y. Tameshige, J. Wambach, R. Yamada, M. Yosoi, and J. Zenihiro, *Complete Electric Dipole Response and the Neutron Skin in* ^{2}08*Pb*, Phys. Rev. Lett. **107**, 062502 (2011).

[82] F. J. Fattoyev and J. Piekarewicz, *Neutron skins and neutron stars*, Phys. Rev. C **86**, 015802 (2012).

[83] B. Friedman, and V. R. Pandharipande, *Hot and cold, nuclear and neutron matter*, Nucl. Phys, A **361**, 502 (1981).

[84] A. Akmal, V. R. Pandharipande, and D. G. Ravenhall, *Equation of state of nucleon matter and neutron star structure*, Phys. Rev. C **58**, 1804 (1998).

[85] S. Gandolfi, J. Carlson, S. Reddy, A. W. Steiner, and R. B. Wiringa, *The equation of state of neutron matter, symmetry energy and neutron star structure*, Europhys. J. A **50**, 10 (2014).

[86] A. W. Steiner, S. Gandolfi, *Connecting Neutron Star Observations to Three-Body Forces in Neutron Matter and to the Nuclear Symmetry Energy*, Rev. Lett. **108**, 081102 (2012).

[87] H. Hammer, A. Nogga, A. Schwenk, *Colloquium: Three-body forces: From cold atoms to nuclei*, Rev. Mod. Phys. **85**, 197 (2013).

[88] A. A. Abrikosov, L. P. Gorkov, and I. E. Dzyaloshinski, *Methods of Quantum Field Theory in Statistical Physics* (Dover, New York, 1975).

[89] A. L. Fetter, J. D. Walecka, *Quantum Theory of Many-Particle Systems*, (Dover, New York, 2003).

[90] D. J. Thouless, *Perturbation Theory in Statistical Mechanics and the Theory of Superconductivity*, Ann. Phys. **10**, 553 (1960).

[91] J. R. Schrieffer, *Theory of Superconductivity* (W. A. Benjamin, New York, 1964).

[92] K. Yosida, *Theory of Magnetism* (Springer-Verlang, Berlin, 1996).

[93] J. Carlson, S. Gandolfi and A. Gezerlis, *Quantum Monte Carlo approaches to nuclear and atomic physics*, Prog. Theor. Exp. Phys. **2012**, 01A209 (2012).

[94] S. Hoinka, P. Dyke, M. G. Lingham1, J. J. Kinnunen, G. Bruun, and C. Vale, *Goldstone mode and pair-breaking excitations in atomic Fermi superfluids*, Nature Physics **13**, 943 (2017).

[95] A. Schwenk, B. Friman and G. E. Brown, *Renormalization group approach to neutron matter: quasiparticle interactions, superfluid gaps and the equation of state*, Nuc. Phys. A **713**, 191 (2003).

[96] T. Abe and R. Seki, *From low-density neutron matter to the unitary limit*, Phys. Rev. C **79**, 054002 (2009).

[97] S. Gandolfi, A. Y. Illarinov, F. Pederiva, K. E. Schmidt, and S. Fantoni, *Equation of state of low-density neutron matter, and the* $^1S_0$ *pairing gap*, Phys. Rev. C **80**, 045802 (2009).

[98] A. Gezerlis, C. J. Pethick, and A. Schwenk, in *Novel Superfluid, Volume 2*, edited by K. H. Nennemann, and J. B. Ketterson, (Oxford University Press, New York, 2014).

[99] F. Lenz, *The Ratio of Proton and Electron Masses*, Phys. Rev. **82**, 554 (1951).